8-11-2020

# Complex Dynamics in Dedicated / Multifunctional Neural Networks and Chaotic Nonlinear Systems

Krishna Pusuluri

# COMPLEX DYNAMICS IN DEDICATED / MULTIFUNCTIONAL NEURAL NETWORKS AND CHAOTIC NONLINEAR SYSTEMS

by

KRISHNA PUSULURI

Under the Direction of Andrey Shilnikov, Ph.D.

## ABSTRACT

We study complex behaviors arising in neuroscience and other nonlinear systems by combining dynamical systems analysis with modern computational approaches including GPU parallelization and unsupervised machine learning. To gain insights into the behaviors of brain networks and complex central pattern generators (CPGs), it is important to understand the dynamical principles regulating individual neurons as well as the basic structural and functional building blocks of neural networks. In the first section, we dis-

cuss how symbolic methods can help us analyze neural dynamics such as bursting, tonic spiking and chaotic mixed-mode oscillations in various models of individual neurons, the bifurcations that underlie transitions between activity types, as well as emergent network phenomena through synergistic interactions seen in realistic neural circuits, such as network bursting from non-intrinsic bursters. The second section is focused on the origin and coexistence of multistable rhythms in oscillatory neural networks of inhibitory coupled cells. We discuss how network connectivity and intrinsic properties of the cells affect the dynamics, and how even simple circuits can exhibit a variety of mono/multi-stable rhythms including pacemakers, half-center oscillators, multiple traveling-waves, fully synchronous states, as well as various chimeras. Our analyses can help generate verifiable hypotheses for neurophysiological experiments on central pattern generators. In the last section, we demonstrate the inter-disciplinary nature of this research through the applications of these techniques to identify the universal principles governing both simple and complex dynamics, and chaotic structure in diverse nonlinear systems. Using a classical example from nonlinear laser optics, we elaborate on the multiplicity and self-similarity of key organizing structures in 2D parameter space such as homoclinic and heteroclinic bifurcation curves, Bykov T-point spirals, and inclination flips. This is followed by detailed computational reconstructions of the spatial organization and 3D embedding of bifurcation surfaces, parametric saddles, and isolated closed curves (isolas). The generality of our modeling approaches could lead to novel methodologies and nonlinear science applications in biological, medical and engineering systems.

INDEX WORDS: Neural networks, Multistability, Central Pattern Generators, Dynamical systems, Chaos, Unsupervised machine learning

# COMPLEX DYNAMICS IN DEDICATED / MULTIFUNCTIONAL NEURAL NETWORKS AND CHAOTIC NONLINEAR SYSTEMS

by

KRISHNA PUSULURI

A Dissertation Submitted in Partial Fulfillment of the Requirements for the Degree of

Doctor of Philosophy

in the College of Arts and Sciences

Georgia State University

2020

# COMPLEX DYNAMICS IN DEDICATED / MULTIFUNCTIONAL NEURAL NETWORKS AND CHAOTIC NONLINEAR SYSTEMS

by

KRISHNA PUSULURI

Committee Chair: Andrey Shilnikov

Committee: Igor Belykh
Mukesh Dhamala
Yaroslav I. Molkov

Electronic Version Approved:

Office of Graduate Studies
College of Arts and Sciences
Georgia State University
August 2020

## DEDICATION

I would like to dedicate this work to Shri Mataji Nirmala Devi, the founder of Sahajayoga, for making my life more purposeful and joyful, through Her teachings of self-realization and inner peace.

“ You cannot know the meaning of your life
until you are connected to the power that created you!"
Shri Mataji Nirmala Devi

## ACKNOWLEDGEMENTS

This work would not have been possible without the valuable contributions of several people. First, I would like to thank my advisor, Dr. Andrey Shilnikov, for his immense support and guidance over the past several years. It would not have been possible to overcome the difficulties in understanding complex biological and mathematical phenomena arising in Neuroscience and Applied Dynamical Systems, without his constant guidance and direction. Since I joined the Shilnikov NeurDS lab, he was always patient in explaining advanced scientific phenomena, and took the trouble of going over every detail multiple times, until I understood its essence. He is willing to learn everyday, open to new suggestions and ideas, and provides valuable feedback and encouragement every step of the way. Since moving from India to the United States for a PhD was not an easy transition, he was always supportive to adapt to the differences in culture and society, constantly inquiring and ensuring my life outside of the lab was going through just as smoothly as was my research. I would like to thank my dissertation committee, Dr. Igor Belykh, Dr. Mukesh Dhamala and Dr. Yaroslav Molkov, for their suggestions and guidance in shaping this dissertation; and Dr. Paul Katz and Dr. Don Edwards for serving in my Proposal committee and Advisory committee, respectively. I want to thank all the current and past members of the Shilnikov NeurDS lab for valuable discussions and feedback: Justus Schwabedal, Jarod Collens, Jeremy Wojcik, Drake Knapper, Aaron Keley, Tingli Xing and Deniz Alacam for their contributions related to multistability of central pattern generators (CPG); Tingli Xing and Jeremy Wojcik for their work related to symbolic methods for chaotic systems; Deniz Alacam, Jack Scully, Jassem Bourahman, and Huiwen Ju for research on modeling the swim CPGs of sea slugs; and Huiwen Ju for work related to half-center oscillators and chaotic dynamics in neuron models. I also want to thank our collaborators Dr. Paul Katz and Dr. Akira Sakurai for insightful discussions into the behaviors of the swim CPGs of sea slugs; and Dr. Hil Meijer and Dr.Arkady Pikovsky for work related to chaotic dynamics

and homoclinic bifurcations.

I am grateful to all the faculty at the Neuroscience Institute for training me in the biological and computational aspects of Neuroscience; Dr. Joseph Normandin and Dr. Marise Parent, with whom I served as a teaching assistant for undergraduate courses, and gained valuable experience; all the staff at the Neuroscience Institute, especially, Emily Hardy for all the administrative assistance, Ryan Sleeth and Rob Poh for technical assistance, and Elizabeth Weaver for assistance in matters related to the Brains and Behavior fellowship. I want to thank the Brains and Behavior initiative of Georgia State University for supporting me with a graduate fellowship. The research was also supported in part by the following grants of my advisor, Dr. Shilnikov: NSF grant IOS-1455527; RSF grant 14-41-00044 at the Lobachevsky University of Nizhny Novgorod; and MESRF project 14.740.11.0919; GSU's Brain and Behavior pilot grant; and NVIDIA Corporation's donation of Tesla K40 GPUs. I want to thank Georgia State University, the city of Atlanta, the United States of America, and the people of this great country, for warmly welcoming me into this land to pursue higher education, and for providing me livelihood, while pursuing research that I am so passionate about. I will forever be greatly indebted!

I want to thank my loving wife, Sunitha Pusuluri (aka Sunitha Basodi), for being part of every aspect of my life through thick and thin, for constantly reminding me of my best parts, as well as for bearing with my worst! I am grateful for her compassion, support, and understanding through all of our major life decisions, including giving up her job and moving to the United States immediately after we got married in India, starting her own graduate studies, and giving birth to our child. While I would be proud of my own Ph.D., I would be prouder still of Sunitha's, who is also graduating at this time with a Ph.D. in Computer Science from GSU, while also managing the more important responsibility of being the mother of our one year old son! I am also thankful for getting the opportunity to work together with her through a couple of research projects and publications, and hope this will be the beginning of many more future collaborations in research, in addition to our joyful pursuit of life together as family. I want to thank our son, Virata Pusuluri, for

bringing so much joy and happiness into our lives. Despite both of his parents working strenuously over the last few weeks towards our Ph.D. dissertations and not spending enough time with him, as well as him having to mostly stay home due to COVID-19, it is so heartening to see Virata being always joyful, playful, innocent and understanding! With one loving smile, he makes us forget everything else and teaches us to live joyfully in the present moment. I hope that when he grows up, he would think all of these efforts were worthwhile, especially those of his mother!

No words would suffice to express my gratitude towards my parents, Mr. V. Umamaheswara Rao Pusuluri and Mrs. Kameswari Pusuluri, for always being there to love and nurture, for building my character, and inspiring me to learn. I still cherish those early memories from childhood when my mother would ask me to multiply large numbers on the fly, and I would do so in my mind. Whenever she inquired what I wanted to be when I grew up, I would say "a Scientist"! I firmly believe her training was instrumental in developing a scientific mind set. My father, through his way of life, showed the importance of curiosity to learn something new everyday, perseverance in the pursuit of my goals, and to find joy in all aspects of life and work. In particular, I want to thank him for teaching me the significance of spirituality and Sahajayoga meditation, making it an integral part of my life from a young age! I don't believe there is anything else in my life that had as much positive impact on me! I want to thank my sister, Janaki Duvvuru, for always motivating me to do well and for being proud of every one of my small achievements. I want to thank my in-laws, cousins, extended family and friends from my hometown Amalapuram, from Hyderabad, and elsewhere, who have all had a positive impact in shaping my outlook towards life. I want to acknowledge the invaluable contributions of all my teachers and professors growing up, particularly from Sarada Convent High School and Aditya Junior College in Amalapuram, Jawaharlal Nehru Technological University and Indian School of Business (ISB) in Hyderabad. I want to thank my former research adviser at ISB, the late Dr. Bhimasankaram Pochiraju, for guiding me towards the pursuit of doctoral education and for teaching me the rigors of a scientific pursuit. I want to thank my former manager

at Yahoo Inc., Mr. Mukund Acharya, and my former colleagues at ISB, Sayali Phadke and Suresh Dasari, for helping with the graduate applications. I want to thank my wonderful country, India, its people, the rich culture, and spirituality, for making me everything I am today!

Finally, I want to thank Sahajayoga meditation, its founder Shri Mataji Nirmala Devi, and all the Sahajayogis of Atlanta, Hyderabad, Amalapuram, and those I met elsewhere around the world, for their immense love and spiritual guidance to focus on the most important aspects of my life, through self realization and inner peace for mental, emotional and spiritual well being. I want to thank all the Sahajayogis of Atlanta, in particular, for warmly welcoming me into this beautiful family, and never making me feel away from home, even after having traveled half-way around the world for my PhD. Through ups and downs in our personal lives, as well as bearing witness to outside troubles, Sahajayoga is what gives me hope and the ability to stay calm and balanced, through its practices of love, peace, equality and the upliftment of all of humanity.

# TABLE OF CONTENTS

# LIST OF TABLES

# LIST OF FIGURES

# CHAPTER 1

# INTRODUCTION

The development and incorporation of new mathematical and computational tools is essential to unravel the multifarious behaviors arising in Neuroscience and other complex dynamical systems. Sensory, motor and cognitive functions are characterized by rhythmic oscillations, whose dysfunction underlies brain disorders such as schizophrenia, epilepsy, autism, Alzheimer's disease, and Parkinson's disease. Understanding the mechanisms regulating rhythmic activities can be helpful in designing therapeutic interventions for such conditions. Smaller structural and functional building blocks of neural networks called 'motifs' are seen in brain networks as well as complex central pattern generators (CPGs) [1, 8–10] (see Fig. 1.1). A CPG is a small biological neural network that determines and autonomously controls rhythmic oscillations underlying a variety of physiological networks such as those controlling locomotion, respiration, sleep, heartbeat and circulation [1, 11–23]. As networks evolve, grow and become more complex, additional elements are incorporated into the existing motifs, maximizing available number of configurations and robustness of the networks [1, 24–26]. A common constituent seen in many known CPGs is a half-center oscillator (HCO), composed of two bilaterally symmetric neurons that mutually inhibit each other, producing an alternating bursting pattern in anti-phase. Multiple HCOs combine via inhibitory, excitatory and/or electrical synapses to form more complex CPG networks, such as those seen controlling the swimming behaviors of sea slugs Melibe leonina and Dendronotus iris [17, 25, 27–32] (see Fig. 1.2). It is important to understand the dynamical principles regulating individual neurons as well as the basic motifs, to gain insights into the behaviors of larger networks.

The cooperative dynamics of coupled cells is an area of active ongoing research, with both biological and phenomenological approaches employed [2, 17, 25, 27–32]. While

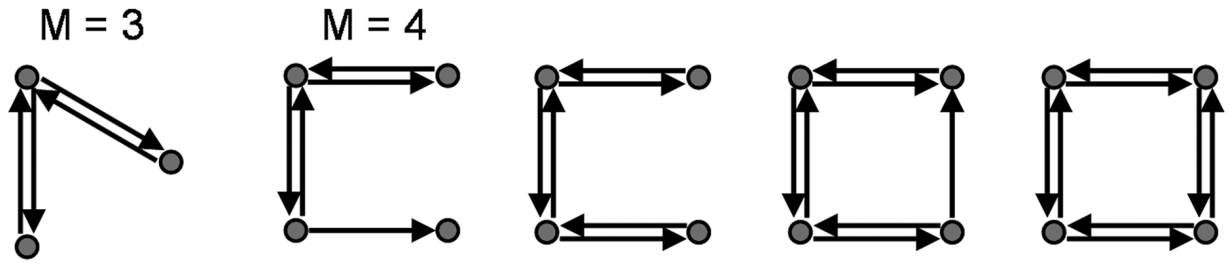


**Figure (1.1)** Structural motifs of sizes 3 and 4 ($M = 3, 4$) that occurred in significantly higher numbers in the brain networks of Macaque and cat cortices. Image adapted with permission and further details can be found in [1].

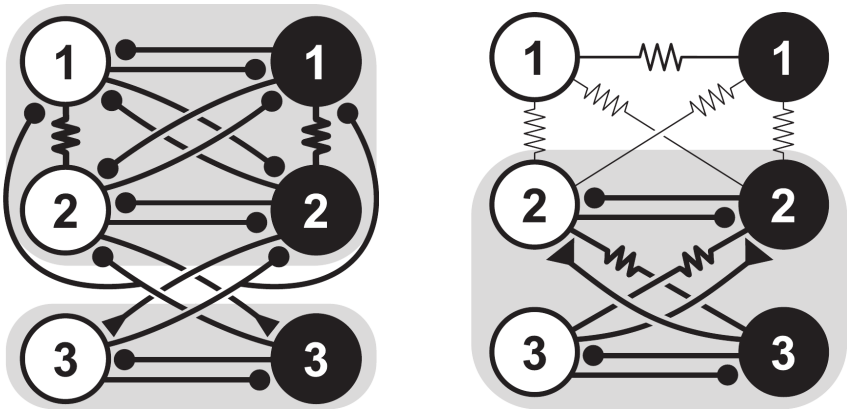


**Figure (1.2)** Swim CPGs of sea slugs Melibe leonina (left) and Dendronotus iris (right), composed of multiple half-center oscillators that are interconnected by inhibitory, excitatory and electrical synapses. Image adapted with permission and further details can be found in [2].

mathematical modeling studies at multiple levels starting from isolated neurons to small networks and populations have provided valuable insights into the working principles of biological neural networks [33–39], the basic principles of robustness and stability of many CPGs observed in nature are yet poorly understood and cannot be inferred apriori. In this thesis, we extend the existing techniques of dynamical systems theory for Neuroscience by combining with modern computational approaches such as unsupervised machine learning [40–46] to further our understanding of complex nonlinear network phenomena. Recent advances in parallel processing and GPU computing [3–5, 47, 48] offer tremendous performance improvements and make it possible to study problems in neuroscience

and nonlinear dynamics that could not be solved earlier. We demonstrate how the techniques developed are applicable to diverse disciplines of nonlinear science. The research is truly inter disciplinary, spanning across the boundaries of neuroscience, applied dynamical systems, modeling, and computer science, and bridges some of the gap between research communities. The broad goal of this research is to gain insights into the universality of rules underlying complex dynamics in diverse systems, with particular emphasis on biological neural networks.

Simple phenomenological and biologically plausible models of isolated neurons can show complex behaviors such as quiescence, tonic spiking, bursting with spike adding, square wave bursting, plateau bursting, parabolic bursting, mixed mode oscillations and chaotic dynamics [5, 25, 49–54]. Neural activity types, their transitions, as well as the occurrence of chaos near the boundaries is described in Chapter 2. Existing techniques such as spike counting, Lyapunov exponents, and parameter continuation can be used to construct biparametric sweeps to identify some of these behaviors, bifurcations, and transitions as parameters of the model are varied. But they are either largely time consuming or require great expertise. In addition, such tools are not readily applicable for studying parametric transitions occurring in even small neural circuits such as half center oscillators and CPGs. There is a dearth of simple and useful tools to study parametric transitions underlying synergistic network dynamics [55–57]. It has been found through parametric exploration that disparate combinations of intrinsic and extrinsic parameters can result in almost identical network activity [58]. Approaches based on parametric optimization based on a cost function can be employed to match model output to experimental results, but they heavily depend on the cost functions, optimization algorithms, and initial parameter values chosen [59]. We address these issues in Chapter 3 through a GPU-based approach of symbolic dynamics that serves as a fast, robust and extensive means to analyze activity types and identify transition boundaries in the parameter spaces of various models of isolated neurons and those of small neural circuits producing dedicated rhythms. We demonstrate how symbolic approaches can be employed to model realis-

tic CPGs and emergent network phenomena in neural circuits, such as network bursting arising from non-intrinsic bursting cells, through the bottom up reconstruction of a CPG governing the swimming behavior of the sea slug Dendronotus iris.

It is an active area of research for both theoretical and experimental work on CPGs to determine whether multiple stable rhythmic patterns are each regulated by dedicated circuits, or the same circuit is capable of stably producing polyrhythmic behavior [2, 26, 38, 60–65]. Input driven transitions between multiple stable attractors governing the CPG dynamics may underlie rhythm switching between different stable patterns as seen in gait switching in locomotion, transitions between swimming and crawling, and changes in the direction of blood flow in leeches [24, 66–68]. In Chapter 4, we focus on such multistable neural networks and briefly describe how Poinaré return maps were previously employed to study the emergence of stable polyrhythms, and their transitions in 3-cell networks. Then, we show how such return maps can be extended into higher dimensions, in conjunction with unsupervised machine learning [40–46], to study multistability in 4-cell and larger networks. We demonstrate the effects of changing network topologies, as well as intrinsic and extrinsic factors on network dynamics, allowing us to generate verifiable hypotheses for experimental neurophysiology. By combining these analytical tools and computational approaches, we can deconstruct the operating rules for the co-existence, stability and robustness of multiple rhythms in complex and modular CPGs, and investigate how smaller constituent motifs can drive complex polyrhythmic behaviors of modular networks.

In Chapter 5, we demonstrate the versatility and cross disciplinary nature of these techniques including symbolic methods and GPU-based parametric sweeps. We elaborate on the onset mechanisms of deterministic chaos due to complex homoclinic bifurcations in diverse nonlinear systems with the Lorenz attractor [69, 70, 70–75, 75–86], through a particular example of a three level optically pumped laser model [87, 88]. By reducing phase space dynamics to symbolic binary representations, we detect regions of simple and complex dynamics, as well as fine organization structures of the latter in parameter

space. We demonstrate how specific codimension-two bifurcations originate and pattern regions of chaotic and simple dynamics. We show detailed computational reconstructions of key bifurcation structures such as Bykov T-point spirals and inclination flips in 2D parameter space, as well as the spatial organization and 3D embedding of bifurcation surfaces, parametric saddles, and isolated closed curves (isolas). The methodologies developed in these studies and their generality would promote novel ideas and approaches for nonlinear science and modeling, with applications to biological, medical, and engineering systems.

# CHAPTER 2

# NEURAL ACTIVITY AND COMPLEX DYNAMICS

In this chapter, we discuss several basic mechanisms of generic activity types such as tonic spiking, bursting and quiescence in phenomenological and biologically plausible models of individual neurons, as well as the occurrence of chaos near the transition boundaries between activity types, where the system may also become bi-stable. The bifurcations underlying these transitions give rise to period-doubling cascades, various homoclinic and saddle phenomena, torus-breakdown, and chaotic mixed mode oscillations in such neuronal systems. This chapter is edited with permission based on the publication and further details can be found in [89].

## 2.1 Background

Neurons exhibit various activity regimes and state transitions that reflect their intrinsic ionic channel behaviors and modulatory states. The fundamental types of neuronal activity can be broadly defined as quiescence, subthreshold and tonic spiking oscillations, as well as bursting composed of alternating periods of spiking activity and quiescence. A single neuron can endogenously demonstrate various bursting patterns, varying in response to the external influence of synapses, or to the intrinsic factors such as channel noise. The co-existence of bursting and tonic spiking, as well as several different bursting modes have been observed in modeling [90–94] and experimental [95–97] studies. This complexity enhances the flexibility of the nervous and locomotive systems [98].

The functional role of chaotic behaviors, and the dynamical and bifurcational mechanisms underlying their onset at transitions between neural activity types like spiking, bursting and quiescence, have been the focus of various theoretical and experimental studies. Bursting is a manifestation of multiple time scale dynamics, composed of repeti-

tive fast tonic spiking and a slow quiescent phase. It has been observed in various fields of science as diverse as food chain ecosystems [99], nonlinear optics [100], medical studies of the human immune system [101], and neuroscience [102]. Various bursting patterns, whether regular or chaotic, endogenous or as emergent network phenomena, are the natural rhythms generated by central pattern generators (CPG) [103–107]. CPGs are neural networks made up of a small number of constituent neurons that often control various vital repetitive locomotive functions [105] such as walking and respiration of humans, or the swimming and crawling of leeches [108–111]. Polyrhythmic bursting dynamics have also been observed in multifunctional CPG circuits that produce several coexisting stable oscillatory patterns or bursting rhythms, each of which is associated with a particular type of locomotor activity of the animal [24, 28, 112]. Bursting has also been frequently observed in pathological brain states [113, 114], in particular, during epileptic seizures [115, 116]. Neurons in bursting modes differ in their ability to transmit information and respond to stimulation from those in tonic spiking mode and therefore play an important role in information transfer and processing in normal states of the nervous system.

Understanding and modeling the generic mechanisms regulating the neuronal connectivity and the transitions between different patterns of neural activity, including global bifurcations occurring in neuron models and networks, pose fundamental challenges for mathematical neuroscience, with a number of open problems [117]. The range of bifurcation and dynamical phenomena underlying bursting *transcends* the existing state of the theory [6, 118–127]: this includes the blue sky catastrophe [128, 129], torus-canard formation and breakdown, and homoclinic inclination/orbit-flip bifurcations, all of which can occur on the transition route to bursting in most square-wave and elliptic bursters. Studies of bursting require nonlocal homoclinic bifurcation analysis, which is often based on the Poincaré return mappings [130]. Return mappings have been employed for computational neuroscience in [131–134]. A drawback of mappings constructed from time series is sparseness, as they reflect only the dominating attractors of a system. In some cases, feasible reductions to one or two dimensional mappings can be achieved through slow–

fast scale decomposition of the phase variables for the system [135]. A new, computer assisted method for constructing a complete family of *onto* mappings for membrane potentials, for a better understanding of simple and complex dynamics in neuronal models, both phenomenological and of the Hodgkin–Huxley type [136], was proposed in [137]. With this approach one can study, for example, the spike-adding transitions in the leech heart interneuron model, and how chaotic dynamics in between is associated with homoclinic tangle bifurcations of some threshold saddle periodic orbits [54]. Qualitative changes in a system's activity at transitions often reveal the quantitative information about changes of certain biophysical characteristics associated with the transition. This approach has proven to be exemplary in neuroscience for understanding the transitions between silence and tonic-spiking activities [138]. Moreover, knowledge about the bifurcation (transition) predicts cooperative behavior of interconnected neurons of the identified types [139].

In this chapter, we discuss nonlocal bifurcations in generic, representative models of neurodynamics, described by high order differential equations derived through the Hodgkin-Huxley formalism. We consider neuroscience-related applications to reveal a multiplicity of causes and their bifurcation mechanisms leading to the onset of complex dynamics and chaos.

## 2.2 Neuronal activities and transition mechanisms

This Chapter deals with phenomenological and biologically plausible neuronal models that can produce complex and distinct dynamics such as tonic spiking, bursting, quiescence, chaos, and mixed-mode oscillations (MMOs) representing fast spike trains alternating with subthreshold oscillations. MMOs are typical for many excitable systems describing various (electro)chemical reactions, including the famous Belousov-Zhabotinky reaction, and models of elliptic bursters [140]. Geometrical configurations of slow-fast neuron models for bursting were pioneered in [138, 141, 142] and further developed in [143–145]. Dynamics of such singularly perturbed systems are determined by and centered around the attracting pieces of the slow motion manifolds. These are composed

of equilibria and limit cycles of the fast subsystem [146–153], that in turn constitute the backbones of bursting patterns in a neuronal model. Using the geometric methods based on the slow-fast dissection, where the slowest variable becomes a control parameter, one can detect and follow the branches of equilibria and limit cycles in the fast subsystem. The slow-fast decomposition allows for drastic simplification, letting one clearly describe the dynamics of a singularly perturbed system. A typical Hodgkin-Huxley model possesses a pair of such manifolds [142, 152]: quiescent and tonic spiking, respectively. The slow-fast dissection has been proven effective in low-order mathematical models of bursting neurons far from the bifurcation points. However, this approach does not account for the reciprocal, often complex interactions between the slow and fast dynamics, leading to the emergence of novel dynamical phenomena and bifurcations that can *only* occur in the whole system. Near such activity transitions, the bursting behavior becomes drastically complex and can exhibit deterministic chaos [6, 123, 124, 154–159].

### 2.2.1 Slow-fast decomposition

Many Hodgkin-Huxley type models can be treated as a generic slow-fast system

$$\mathbf{x}' = \mathbf{F}(\mathbf{x}, z) \quad z' = \mu G(\mathbf{x}, z, \alpha), \tag{2.1}$$

where $0 < \mu \ll 1$, $\mathbf{x} \in R^n$, $n \geq 2$, and $z$ is a scalar, or can be a vector in $R^2$ (as in the extended Plant model with two slow variables below); $\alpha$ is a control parameter shifting the slow nullcline, given by $G(\mathbf{x}, \alpha) = 0$, in the phase space. In the singular limit $\mu = 0$, the $z$-variable becomes a parameter of the fast subsystem to detect and continue the equilibrium state (ES), given by $\mathbf{F}(\mathbf{x}, z) = 0$, and the limit cycles (LC) of the fast subsystem. As long as they (ES/LC) remain exponentially stable, by varying $z$ one can trace down the smooth invariant manifolds in the phase space of (2.1) such as $\mathrm{M}_{\mathrm{eq}}$ with the distinct $Z$-shape typical for many Hodgkin-Huxley type models (see Fig. 2.1), while the limit cycles form a cylinder-shaped surface $\mathrm{M}_{\mathrm{lc}}$. Locally, either is a center manifold for (2.1) persisting in a closed system, in virtue of [146–148]. The stable upper and lower branches of $\mathrm{M}_{\mathrm{eq}}$

correspond to the de- and hyperpolarized steady states of the neuron, respectively. Folds on $\mathrm{M_{eq}}$ correspond to the saddle-node equilibrium states of the fast subsystem. The unstable de-polarized branch of $\mathrm{M_{eq}}$ can be enclosed by the tonic-spiking manifold $\mathrm{M_{lc}}$ typically emerging through an Andronov-Hopf bifurcation and terminating through a homoclinic bifurcation, which are the key features of the fast-subsystem of the square-wave bursters [49], like the Hindmarsh-Rose model [160] and the Chay model [133] (discussed below).

### 2.2.2 Poincaré mappings

To elaborate on the nature of complex oscillations like bursting and their evolutions, one needs to examine nonlocal bifurcations that often require the use of Poincaré return maps [131–133, 155, 161–165]. An obvious drawback of maps constructed from voltage time series is in their sparseness, as they can typically reveal some point-wise attractors of the system that trajectories fast converge to, unless there is a noise or small perturbations are added to get a more complete picture of the underlying structure. In some cases, a feasible reduction to low-dimensional mapping can be achieved through slow–fast scale decomposition of slow phase variables [128,130,135]. We proposed and developed a new computer assisted algorithm for constructing a dense family of *onto* mappings for membrane potentials in a Hodgkin–Huxley type neuronal model [125]. Such maps let us find and examine both the stable and unstable solutions in detail; moreover, unstable points are often the primary organizing centers globally governing the dynamics of the model in question. The construction of such a map begins with the localization of the tonic spiking manifold $\mathrm{M_{lc}}$ in the model, using the parameter continuation technique or the slow-fast dissection, see Fig. 2.1. Then, a curve on $\mathrm{M_{lc}}$ is defined, which corresponds to minimal (maximal) voltage values, denoted, say, by $\mathrm{V}_0$. By construction, the 1D map $M$ takes all $\mathrm{V}_0$ (outgoing solutions integrated numerically) on this curve back onto itself, after a single turn around $\mathrm{M_{lc}}$, i.e., $M: V_0 \to V_1$ for a selected value of the parameter. Two such maps are depicted in Figs. 2.1 and 2.2. One can see that these are non-invertible [166,167], uni-

modal maps with a single critical point [168,169], which happens to be a universal feature of many other square-wave bursters in neuroscience applications. With such maps, one can fully study the attractors, the repellers and their bifurcations, including saddle-nodes, homoclinic orbits, spike-adding, and period-doubling. We note that detection of homoclinics of a saddle periodic orbit in the phase space of a model is in general *state-of-the art* and the Poincaré map technique allows us to locate them with ease.

### 2.2.3 Classifications of bursting

The existing classifications [138, 141–145] of bursting are based on the bifurcation mechanisms of dynamical systems in a plane, which initiate or terminate fast trajectory transitions between the slow motion manifolds in the phase space of the slow-fast neuronal model. These classifications allow us to single out the classes of bursting by subdividing mathematical and realistic models into the following subclasses: elliptic or Hopf-fold subclass (FitzHugh-Rinzel [140] and Morris-Lecar models), square-wave bursters or fold-homoclinic subclass (Hindmarsh-Rose model [52,126], models of pancreatic $\beta$-cells, cells in the pre-Botzinger complex, as well as intrinsically bursting and chattering neurons in neocortex); parabolic or circle-circle subclass (model of R15 cells in the abdominal ganglion of the mollusk Aplysia [93, 112], the reduced leech interneuron model at certain parameter values); and fold-fold subclass, or top hat models [170], including the reduced heart interneuron model (2.3) discussed below.

### 2.2.4 Transition routes

The current description of the transition routes between tonic spiking and bursting activities is incomplete and remains a fundamental problem for both neuroscience and the theory of dynamical systems. The first theoretical mechanism revealed in [154], explained chaos in the so-called square wave bursters [142] emerging between tonic-spiking and bursting. Later, two global bifurcations that occur at the loss of stability of a tonic spiking periodic orbit through quite novel homoclinic saddle-node bifurcations, were discov-

ered and explained. The first transition, reversible and continuous, found in the reduced model of the leech heart interneuron [6, 122] and in a modified Hindmarsh-Rose model of a square-wave burster [126, 130], is based on the blue sky catastrophe [130, 171–174]. This was proven in [128] to be a typical bifurcation for slow-fast systems. This striking term [175], the *blue sky catastrophe*, stands for a novel bifurcation of a saddle-node periodic orbit with a 2D unstable manifold returning to the orbit making infinitely many revolutions. After the bifurcation, this homoclinic connection transforms into a long bursting periodic orbit with infinitely many spikes. The burst duration of the orbit near the transition is evaluated by $1/\sqrt{\alpha}$, where $0 < \alpha \ll 1$ is a bifurcation parameter. The second transition mechanism is due to a saddle-node periodic orbit with non-central homoclinics [176]. An important feature of this transition is the bi-stability of co-existing tonic spiking and bursting activities in the neuron model, see Fig. 2.1. In this case, the burst duration towards the transition increases as fast as $|\ln(\alpha)|$. Another feature of this bifurcation is the transient chaos where the neuron generates an unpredictable number of burst trains before it starts spiking tonically. This phenomenon is a direct consequence of the Smale horseshoe finite shift dynamics in the system [177], which is a rather atypical phenomenon for such slow-fast systems.

## 2.3 Chaos in neuron models

In this section, we present the basic mechanisms and routes to chaos in a variety of biophysically realistic neuronal models exhibiting rich and complex dynamics including tonic spiking, bursting and quiescence. A bifurcation describing a transition between neuronal activities typically occurs near saddle (unstable) orbits and results from reciprocal interactions involving the slow and fast dynamics of the model. Such interactions lead to the emergence of new dynamical phenomena and bifurcations that can occur only in the full model, but not in either of the slow or the fast subsystem. Chaotic dynamics can be characterized by unpredictable variations in the number of spikes during the active phases

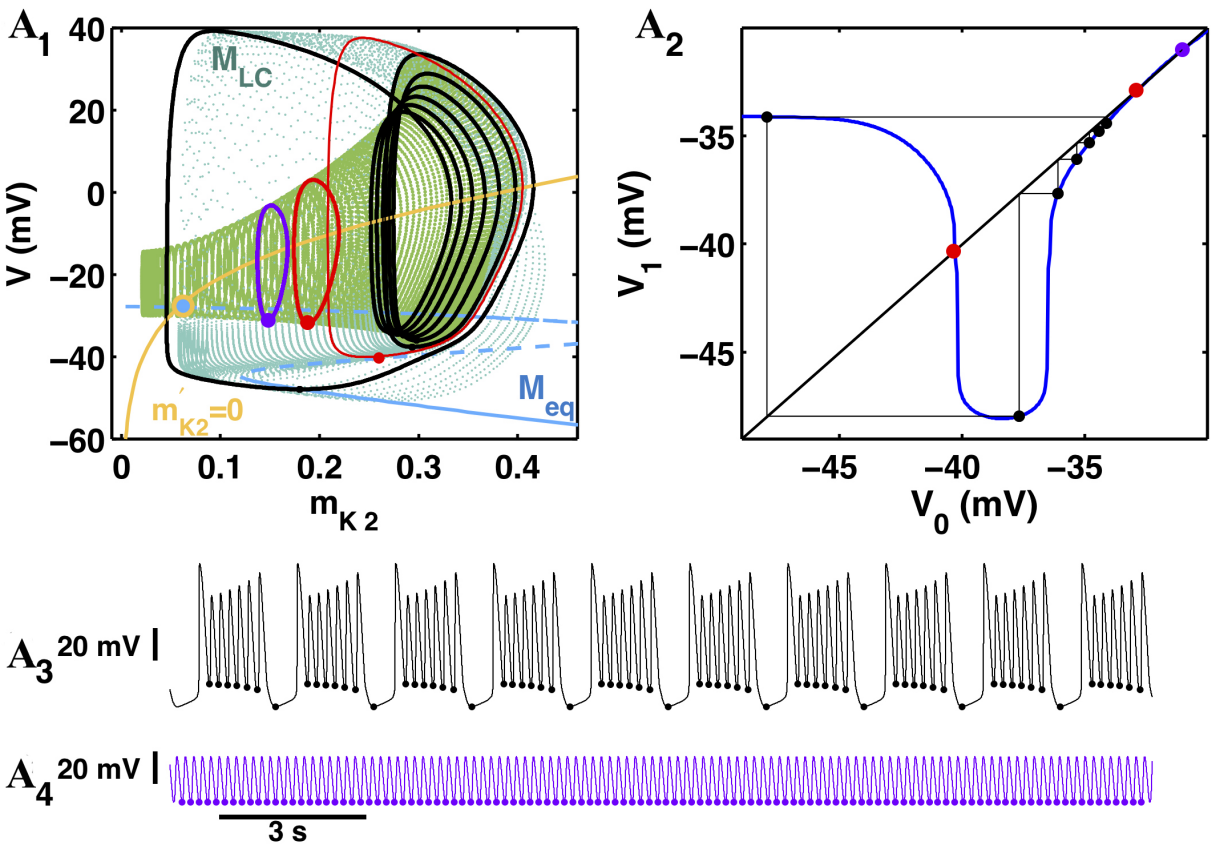


**Figure (2.1)** ($\mathbf{A_1}$) Bistability of the coexisting tonic-spiking and bursting in the 3D phase space of the leech heart interneuron model (2.3). Inset $\mathbf{A_2}$ depicts the shape of the corresponding 1D Poincaré map with stable fixed point corresponding to the tonic spiking periodic orbit (purple) with a single voltage minima, and period-7 bursting orbit, and 2 unstable fixed points (red): the right one separates attraction basins of tonic-spiking ($\mathbf{A_4}$) and bursting $\mathbf{A_3}$) activities, whereas the left one causes chaotic dynamics at spike adding transitions, see Fig. 2.2.

of bursting and/or the subthreshold oscillations. This phenomenon of chaotic dynamics is generally atypical in slow-fast systems as it occurs within narrow parameter windows only near the transition boundaries. Indeed, robust and regular dynamics of slow–fast neuron models contrast those of real bursting neurons exhibiting a phenomenal time dependent variability of oscillatory patterns.

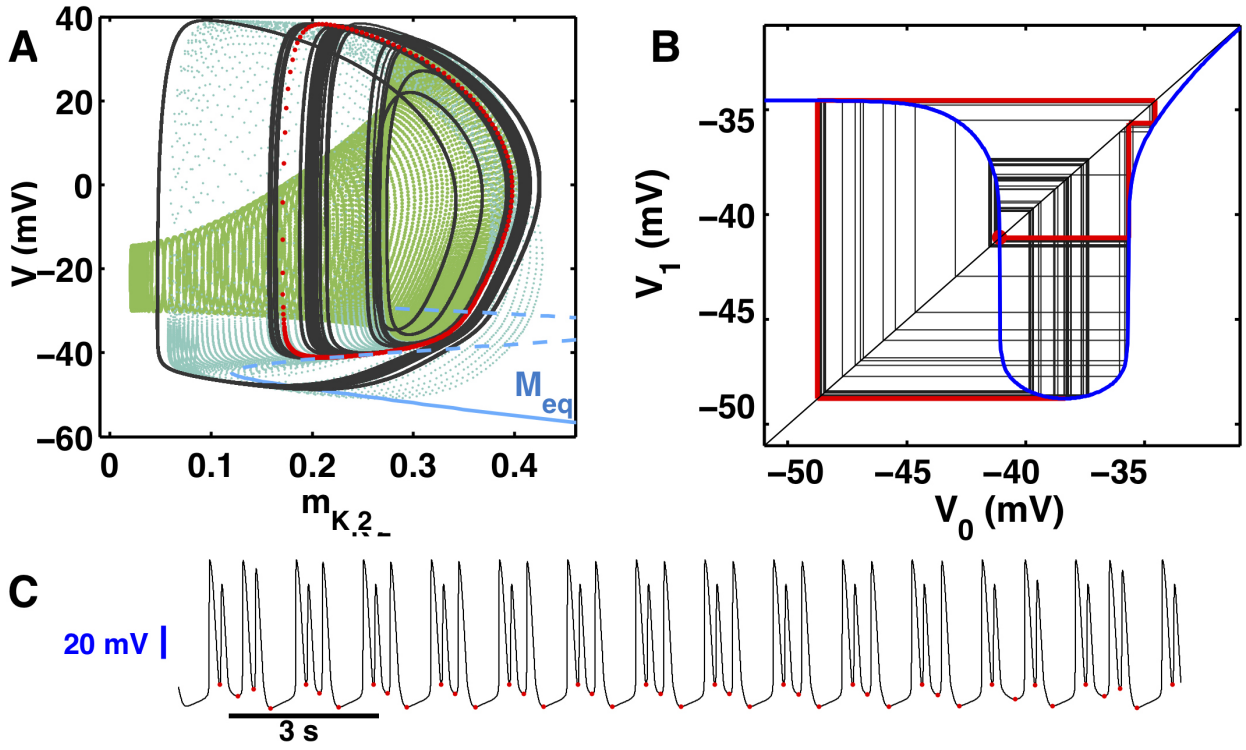


**Figure (2.2)** (**A**) Chaotic bursting in the phase space of the leech heart interneuron model (2.3) and the corresponding map (**B**) at a transition between two and three spikes per burst in the voltage trace (**C**) due to proximity of the primary homoclinic orbit of the repelling fixed point (red) corresponding to a single minimum of the saddle periodic orbit (red) in (**A**).

### 2.3.1 Leech heart interneuron model: period doubling cascades and the blue sky catastrophe

We first illustrate and discuss the onset of chaotic dynamics in the reduced (3D) model of the leech heart interneuron (see equations (2.3) of Appendix). This is a *typical* slow-fast Hodgkin-Huxley type (HH) model describing the dynamical interplay of a single slow variable – persistent potassium current, $\mathrm{I_{K2}}$, and two fast variable – the sodium current, $\mathrm{I_{Na}}$ and the membrane voltage $\mathrm{V}$ that can be recast in this generic form [49, 53, 122, 123]:

$$CV_i' = -\sum_j I_j - \sum_i I_i^{\mathrm{syn}}, \quad \tau_h\, h' = f_\infty(V) - h, \tag{2.2}$$

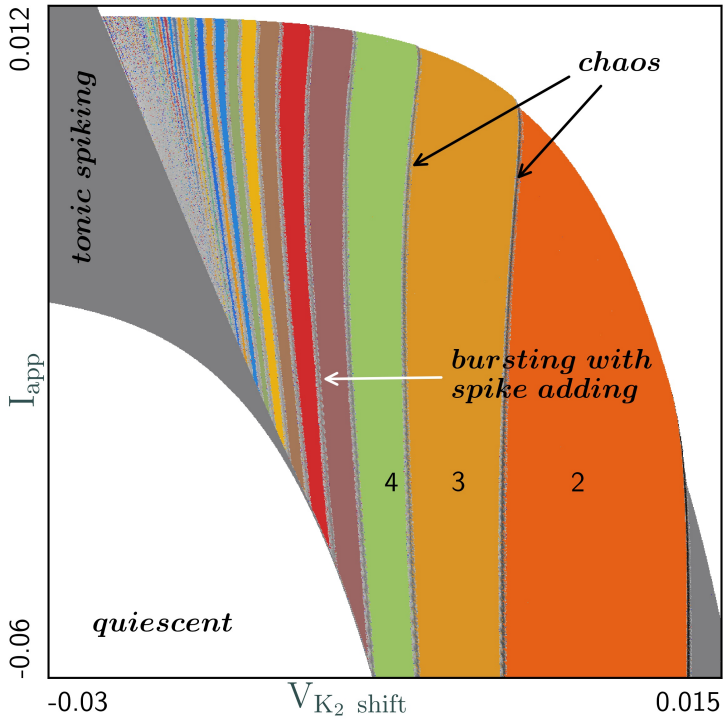


**Figure (2.3)** Bi-parametric sweep of the leech heart interneuron model (2.3) using the symbolic toolkit *Deterministic Chaos Prospector* [3–5] to process wave-form traces and to reveal regions of quiescent behavior, tonic spiking, as well as bursting activity with spike adding cascades: from 2 spikes (orange zone) to 3 spikes (yellowish zone), next to 4 spikes (light green zone) and so forth. The noisy regions near the boundaries of spike addition reveal the occurrence of chaos, while the noisy boundary between tonic spiking and bursting portrays the blue sky catastrophe [6] corresponding to infinitely long bursting.

where $C$ is a membrane capacitance, $V$ is a transmembrane voltage, $I_j$ stands for various in/outward currents including synaptic ones, $0 \leq h \leq 1$ stands for a gating (probability) variable, $f_\infty$ is a sigmoidal function, and $\tau_h$ is a time scale, fast or slow, specific for specific currents.

This model shows a rich set of dynamics and can produce various types of complex chaotic and bistable behaviors, including the period-doubling cascade *en a route* from tonic spiking through bursting [6, 124], as well as various types of homoclinic chaos. Following the period-doubling cascade, the model demonstrates a terminal phase of chaotic tonic spiking that coexists alongside another periodic tonic spiking activity. For a different set of parameter values compared to the period doubling cascade, the model can also ex-

hibit the blue sky catastrophe as a continuous and reversible mechanism of the transition between bursting and tonic spiking. Fig. 2.1 explains the nature of bi-stability in this model as it exhibits the co-existing tonic-spiking and bursting oscillations corresponding to the stable fixed point (FP) (purple) and the period-7 orbit in the 1D map, whose basins are separated by an unstable FP representing a saddle periodic orbit (red) on the 2D manifold $\mathrm{M}_{\mathrm{lc}}$ in the 3D phase space. The role of the other unstable (red) FP is revealed by Fig. 2.2. It is shown that the spike-adding in bursting is accompanied with an onset of chaotic dynamics orchestrated by the homoclinic orbits and bifurcations involving the other saddle orbit, see more details in [49, 52–54, 129, 140, 160]. Fig. 2.3 shows the bifurcation diagram of the system constructed as a parametric sweep using our previously developed symbolic toolkit called the *Deterministic Chaos Prospector* [3–5] to process symbolic sequences extracted from wave-form traces and analyze activity types and underlying bifurcations. This bifurcation diagram identifies the regions of quiescence, tonic spiking, as well as bursting with spike adding cascades. The noisy regions near the boundaries of spike addition reveal the occurrence of chaos. In addition, the blue sky catastrophe takes place at the noisy region near the boundary between bursting and tonic spiking.

### 2.3.2 Chaotic mixed-mode oscillations in the extended Plant model

The conductance-based Plant model of endogenous parabolic bursters was originally developed to model the R15 neuron in the abdominal ganglion of the slug Aplysia Californica [93]. This was later extended and adapted to model the swim CPG of the sea slug *Melibe Leonina*, see [112] for details of the model and the equations. This model can produce chaotic bursting activity, as shown in Fig. 2.4A near the boundary between tonic spiking and bursting activity. In addition, the model exhibits complex chaotic *mixed mode oscillations* (MMOs) near the transition between bursting and the co-existing hyper-polarized quiescence state. Fig. 2.4B illustrates the model generating spike-varying bursts and small amplitude sub-threshold oscillations. Such chaotic MMOs coexist with a hyperpolarized quiescent state resulting in bistability due to a subcritical Andronov-Hopf

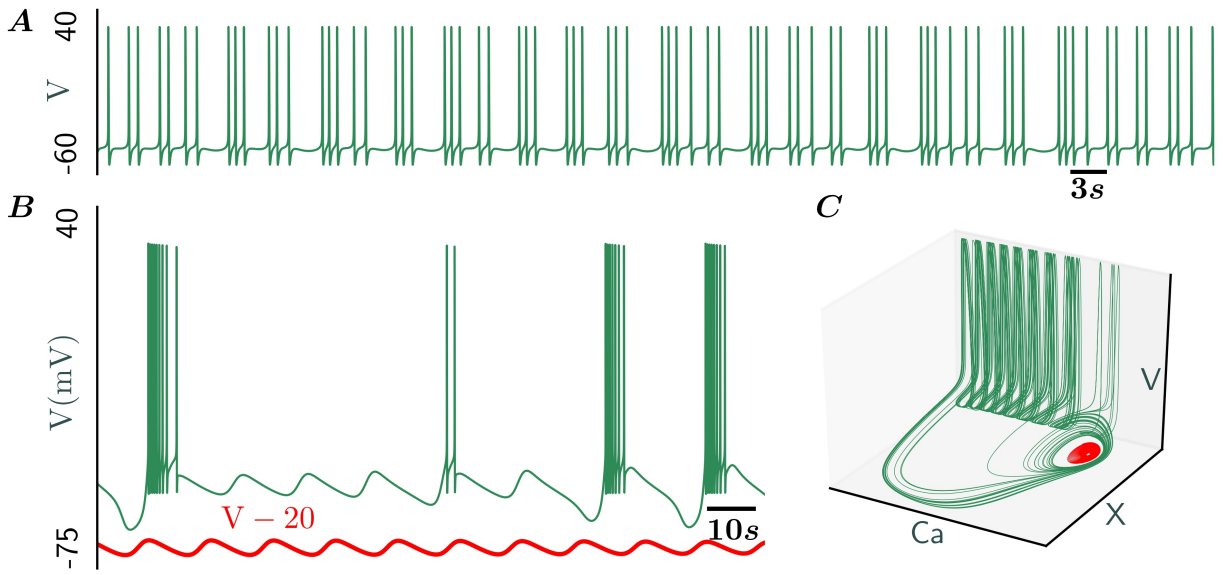


**Figure (2.4)** The extended Plant model can exhibit chaotic bursting near the boundaries of tonic spiking and bursting with spike-adding (**A**) as well as bistability with chaotic mixed mode oscillations (green) and hyperpolarized quiescence (red) near the transitions between bursting with spike-adding and hyperpolarized quiescence (**B**). The corresponding phase space projection of the bistable states of (**B**) are shown in (**C**). Following a subcritical Andronov-Hopf bifurcation, a saddle periodic orbit (not seen) separates the chaotic mixed mode bursts (green) from the hyperpolarized quiescent state with spiral convergence (red).

bifurcation that gives rise to a saddle periodic orbit whose stable manifold separates the chaotic bursting activity (green) from the stable (spiraling) hyperpolarized quiescent state (red) as shown in Fig. 2.4C. As the parameters are varied gradually the system transitions from this bistable state to the monostable hyperpolarized quiescence, or vice verse to a dominant bursting activity.

## Appendix

Leech heart interneuron model

The reduced leech heart model is derived using the Hodgkin-Huxley formalism:

$$\begin{aligned} C\,V' &= -I_{\mathrm{Na}} - I_{\mathrm{K2}} - I_{\mathrm{leak}} + I_{\mathrm{app}}, \\ \tau_{\mathrm{Na}} h'_{\mathrm{Na}} &= h^{\infty}_{\mathrm{Na}}(V) - h, \\ \tau_{\mathrm{K2}} m'_{\mathrm{K2}} &= m^{\infty}_{\mathrm{K2}}(V) - m_{\mathrm{K2}}, \end{aligned} \tag{2.3}$$

with

$$I_{\mathrm{leak}} = 8(V + 0.046), \quad I_{\mathrm{K2}} = 30\, m^2_{\mathrm{K2}}(V + 0.07), \quad I_{\mathrm{Na}} = 200[m^{\infty}_{\mathrm{Na}}(V)]^3\, h_{\mathrm{Na}}\,(V - 0.045),$$

and where $V$ is the membrane potential, $C = 0.5$; $h_{\mathrm{Na}}$ is a fast ($\tau_{\mathrm{Na}} = 0.0405$ sec) activation of $I_{\mathrm{Na}a}$, and $m_{\mathrm{K2}}$; $I_{\mathrm{L}}$ describes the slow ($\tau_{\mathrm{K2}} = 0.25$ sec) activation of $I_{\mathrm{K2}}$, $I_{\mathrm{app}}$ is an applied current. The steady states $h^{\infty}_{\mathrm{Na}}(V)$, $m^{\infty}_{\mathrm{Na}}(V)$, $m^{\infty}_{\mathrm{K2}}(V)$, of the of the gating variables are given by the Boltzmann equations given by

$$\begin{aligned} h^{\infty}_{\mathrm{Na}}(V) &= [1 + \exp(500(0.0333 + V))]^{-1}, \\ m^{\infty}_{\mathrm{Na}}(V) &= [1 + \exp(-150(0.0305 + V))]^{-1}, \\ m^{\infty}_{\mathrm{K2}}(V) &= [1 + \exp\left(-83(0.018 + \mathrm{V}^{\mathrm{shift}}_{\mathrm{K2}} + V)\right)]^{-1}. \end{aligned} \tag{2.4}$$

The bifurcation parameter $\mathrm{V}^{\mathrm{shift}}_{\mathrm{K2}}$ of the model is a deviation from the experimentally determined voltage $V_{1/2} = 0.018$V corresponding to the half-activated potassium channel, i.e. to $m^{\infty}_{\mathrm{K2}}(0.018) = 1/2$. In its range $\mathrm{V}^{\mathrm{shift}}_{\mathrm{K2}}$ is $[-0.025;\, 0.0018]$V the upper boundary corresponds to the hyperpolarized quiescent state of the neuron, whereas the model produces spiking oscillations at the lower end $\mathrm{V}^{\mathrm{shift}}_{\mathrm{K2}}$ values and bursts in between.

# CHAPTER 3

# SYMBOLIC METHODS FOR NEURAL DYNAMICS AND EMERGENT NETWORK BEHAVIORS

In this chapter, we present an approach based on the symbolic dynamics of voltage wave forms and parametric sweeps to study complex bahaviors arising in models of individual neurons and rhythmic neural circuits, as we vary intrinsic cell properties and external parameters that can be controlled in neurophysiological experiments with dynamic clamp. We analyze diverse activity types in isolated neurons such as tonic spiking, quiescence, or intrinsic bursting, and determine their bifurcation boundaries. We show how chaotic behavior can arise near activity transitions. Using an extended encoding scheme for coupled neurons, we demonstrate emergent network phenomena that can not be readily inferred from individual neuron properties. We demonstrate how a half-center oscillator (HCO), composed of two mutually inhibiting neurons, can produce anti-phase bursting oscillations, even when individual cells are not intrinsic bursters, as is seen in experimental neurophysiology. This is followed by the bottom up reconstruction of a 4-cell circuit, modeled after the swim central pattern generator (CPG) of the sea slug Dendronotus Iris. We build the circuit from the bottom up, starting from individual cells, to pairs of HCO oscillators, all the way up to the fully connected 4-cell circuit with multiple inhibitory, excitatory and electrical synapses. Through detailed parametric sweeps, we find appropriate model parameters to replicate experimentally determined CPG behavior of emergent 4-cell network bursting, where neither the individual cells nor the HCO pairs can themselves sustain bursting, without the synergistic interactions of excitation, inhibition and electric coupling in the full circuit.

### 3.1 Background

Common structural and functional building blocks of neural networks are seen in brain networks [1,8–10] as well as complex central pattern generators (CPGs). CPGs are rhythmic neural circuits that can control motor output, independent of rhythmic sensory feedback or input from higher centers. CPGs are seen in a variety of physiological networks such as those controlling walking, crawling, swimming, respiration, heartbeat, and digestion. [1, 11–23, 178]. A pair of bilaterally symmetric neurons with mutual inhibition resulting in anti-phase bursting, called a half-center oscillator (HCO), is commonly seen across various CPGs. Multiple HCOs may also interact through electrical and chemical synapses to form complex CPG networks like the swim CPGs of sea slugs Melibe leonina and Dendronotus iris [2, 17, 25, 27–32, 179, 180]. As networks grow, such building blocks are preserved and adapted for optimal network configurations [1, 24–26]. Simple and biologically relevant isolated neuron models can themselves show a variety of complex behaviors including quiescence, tonic firing, bursting with spike adding, square wave / plateau / parabolic bursting, chaotic spiking / bursting and mixed mode oscillations [5,25,49–54]. Dynamics analysis of individual neurons and the basic building blocks of neural circuits is important to discern complex network behaviors. Previous modeling studies of isolated neurons, neural circuits producing dedicated or multistable rhythms, and neural populations provided valuable insights into the working principles of biological neural networks. [24,33–39,181,182]. Simple and useful tools to study parametric transitions of synergistic network dynamics are lacking [55–57]. Studies employing parametric exploration have shown that disparate combinations of intrinsic and extrinsic parameters can result in almost identical network activity [58]. Approaches based on parametric optimization based on a cost function can be employed to match model output to experimental results, but they heavily depend on the cost functions, optimization algorithms, and initial parameter values chosen [59]. Techniques such as spike counting, Lyapunov exponents, or parameter continuation can be used to construct biparametric sweeps (such as

Fig. 3.3) for isolated neuron models and perform a detailed analysis of their behaviors, bifurcations, and transitions [5,51,52]. But they are either largely time consuming or require great expertise. In addition, such tools are not easily applicable for studying parametric transitions occurring in half center oscillators and more complex CPGs. In this chapter, we address these issues through a GPU-based approach of symbolic dynamics that serves as a fast, robust and extensive means to analyze activity types and identify transition boundaries in the parameter spaces of various models of isolated neurons and neural circuits. This approach is an extension of our previously developed toolkit called Deterministic Chaos Prospector (DCP) and is adapted for neurons and networks [3–5, 183]. DCP was previously employed to study the universal principles of homoclinic and heteroclinic bifurcations of saddle equilibria in Lorenz-like systems, and to detect regions of simple and chaotic dynamics in the parameter space [64,184,185,185–187]. Preliminary results for individual neuron models were presented in [5]. In the following sections, we will describe symbolic encoding using a simple partitioning scheme based on voltage values and time intervals between successive events, such as spiking or sub-threshold oscillations, obtained from voltage wave-form trajectories of neurons. We will demonstrate how this approach can be used to study the dynamics of the extended Plant model with non-intrinsic bursting, used to model the swim CPG of the sea slug Melibe Leonina [65]. This model was adapted from the conductance-based Plant model of endogenous parabolic bursters, originally used to model the R15 neuron in the abdominal ganglion of the sea slug Aplysia Californica [188]. We show the activity regimes of the extended model based on changes in intrinsic cell properties. We will then demonstrate how a HCO composed of two such non-intrinsic bursters can give rise to emergent network bursting. This is important to model experimental data, where often network bursting is observed in intrisically tonic spiking cells [2,31,65,179,180]. This is followed by the description of further modifications in the extended Plant model, to produce qualitatively similar dynamics as seen in the swim CPG of the sea slug Dendronotus Iris [2,31,65,179,180]. We employ detailed biparametric sweeps of intrinsic cell properties as well as external parameters chosen such

that they can be controlled in neurophysiological experiments through dynamic clamp. A bottom up reconstruction of its simplified 4-cell circuit, with multiple inhibitory, excitatory and electrical synapses, that mimics experimentally determined CPG behavior is presented, starting from individual cells, to pairs of HCO oscillators, all the way up to the fully connected 4-cell circuit, with emergent network bursting. Neither the individual cells nor the HCO pairs can themselves sustain bursting, without the synergistic interactions of excitation, inhibition and electric coupling.

## 3.2 Methods

### 3.2.1 Symbolic dynamics of neurons and circuits

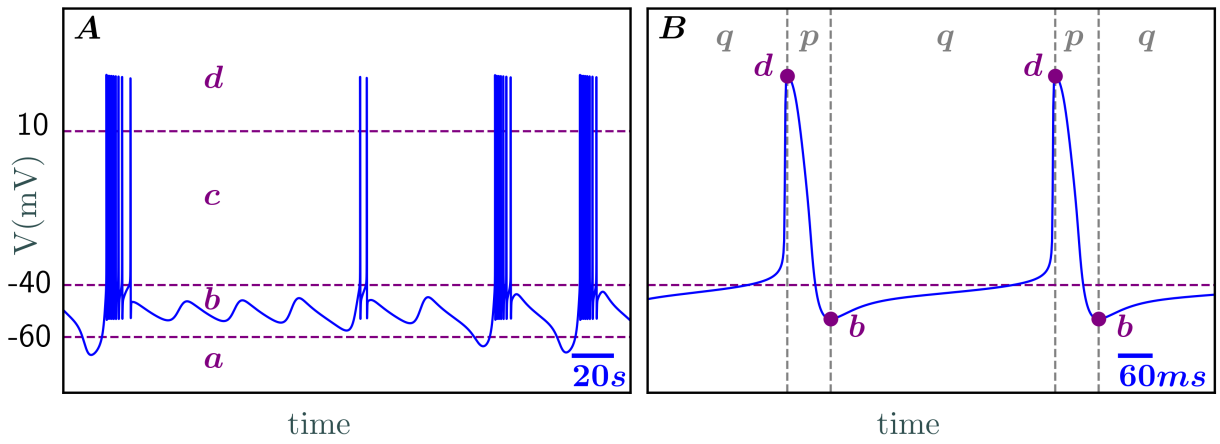


**Figure (3.1)** (A) Symbolic partitions for a complex mixed-mode chaotic bursting trace in the extended Plant model. Using $V_{bins} = [-60, -40, 10]mV$ (purple dashed lines) results in a set of 4 symbols $(a \leq -60 < b \leq -40 < c \leq 10 < d)$. A short segment within a burst is magnified in (B), showing two spikes, with corresponding descriptions of maximal and minimal voltage events (purple dots). Using $V_{bins}$, this segment is encoded as $(dbdb)$ (in purple). The encoding is $(qpqpq)$ (in gray) if we use $T_{bins} = [100]ms$, resulting in a set of 2 symbols $(p \leq 100 < q)$, for the time intervals between successive events (gray dashed lines enclosing spikes). A combination of both partitions gives a detailed symbolic sequence $(qdpbqdpbq)$.

Our method of symbolic encoding is inspired from experimental neurophysiology, where voltage wave-forms are usually the only observables available. One simple way to

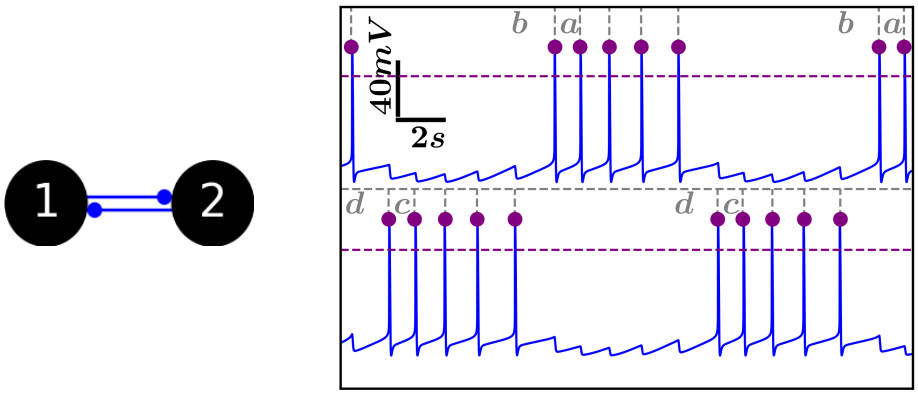


**Figure (3.2)** Symbolic encoding of anti-phase bursting oscillations in a HCO composed of a pair of the extended Plant model cells, that mutually inhibit each other (left). We use $V_{bins} = [10]mV$ to detect all maximal events above this threshold (purple dots), and $T_{bins} = 2.5s$ to encode the intervals between successive events (gray vertical lines), resulting in the symbols $(a \leq 2.5 < b)$ for cell $1$ and $(c \leq 2.5 < d)$ for cell $2$. When the first spike of a burst is encountered for cell $1$, it is marked by the symbol $b > 2.5$. The second spike is marked by the symbol $a < 2.5$. Successive spikes within the burst (to be marked $a$, otherwise) are omitted, to avoid conflicts when cells in the network have overlapping burst durations. Thus the repeating anti-phase bursting oscillations in the HCO are encoded as $(\overline{dcba})$.

construct a partitioning scheme is to break a voltage wave-form into equally spaced time-bins, shorter than the typical duration of a spike. Within each bin, we observe whether there is a spike, and mark its presence or absence using the symbols $1$ and $0$. Thus, a continuous voltage trace can be converted into a binary sequence. Another partitioning scheme can identify events of maximal and minimal voltage values in the trace. Whenever a maximal value above the firing threshold is detected, it is marked by the symbol $1$, while a minimal value detected below the threshold is marked by the symbol $0$. This approach is similar to spike counting, for a typical square-wave burster without sub-threshold oscillations. For our analysis, we employ a multi-bin symbolic partitioning scheme using both voltage and timing information to identify a variety of neuronal dynamics including quiescence, tonic spiking, spike addition, square-wave bursting, plateau-busting, parabolic bursting, mixed-mode oscillations, quasi-periodicity and chaos. Depending on the scope of investigation, one may appropriately choose as many symbols as needed, as described

below. Fig. 3.1 shows a chaotic bursting trace recorded in the extended Plant model [65] (described in the following sections), with unpredictable numbers of both spikes per burst as well as sub-threshold oscillations separating such bursts. We compute all the events corresponding to maximal and minimal voltage values (red dots in Fig. 3.1), and the time intervals between successive events (vertical gray dashed lines). Using voltage and time interval partitions, $V_{bins}$ and $T_{bins}$, we map the event and timing information from the trajectory into a sequence of symbols. For $V_{bins} = [-60, -40, 10]$mV (red dashed lines), we get four symbols $(a \leq -60 < b \leq -40 < c \leq 10 < d)$, corresponding to quiescence or burst termination, sub-threshold oscillations, plateau burst, and spiking, respectively. On the other hand, using $T_{bins} = [100]$ms, results in a set of $2$ symbols, $(p \leq 100 < q)$, representing successive events of maxima/minima that are separated by a duration shorter or longer than $100$ms, respectively. The symbolic representation of the short magnified segment of two spikes from inside a burst shown in Fig. 3.1B, using $V_{bins}$, $T_{bins}$, and a combination of both, are given by $(dbdb)$ (red), $(qpqpq)$ (gray) or $(qdpbqdpbq)$, respectively. Using an overbar to represent repeating sequences, a tonic spiking trace similar to this segment can be marked as $(\overline{db})$, $(\overline{qp})$ or $(\overline{qdpb})$. Similarly, a bursting trajectory with 3 spikes and no MMOs can be shown as $(\overline{dbdbda})$. Since there is no limit on the number of symbols that can be used with DCP, we can incorporate disparate symbol sets to simultaneously analyze the voltage traces of multiple cells within a circuit and study network rhythms, using these same techniques. Fig. 3.2 shows a HCO composed of a pair of the extended Plant model cells, mutually inhibiting each other. The modified symbolic encoding scheme for the anti-phase bursting rhythm in the network is shown. We use a combination of $V_{bins} = [10]mV$ and $T_{bins} = [2.5]s$, with relatively loosely defined criteria compared to the encoding of isolated cells, in order to allow for some variability in spike timing across cells, while producing stable rhythms. All maximal events (purple dots) in voltage above the threshold of $V_{bins}$ are detected. The time intervals between successive events (gray vertical lines) is computed and encoded using $T_{bins}$. The symbols $(a \leq 2.5 < b)$ are used for cell $1$ and $(c \leq 2.5 < d)$ for cell $2$. When the first spike of a burst is encountered for cell $1$, it is marked

by the symbol $b > 2.5s$. The second spike is marked by the symbol $a < 2.5s$. Successive spikes within the burst (to be marked $a$, otherwise) are omitted, to avoid spike timing conflicts when cells in the network have overlapping burst durations. Thus the repeating anti-phase bursting oscillations in the HCO are encoded as $(\overline{dcba})$. We also measure and keep track of the average number of spikes per burst, when there is a well defined rhythm, or the total spikes, if there is no network bursting. Since this study deals with dedicated circuits producing a single stable network rhythm, these set of loose criteria are sufficient as demonstrated below. For multifunctional circuits, an appropriate combination of the partitions and other criteria must be chosen to account for multiple phase locked states. For the Dendronotus model described below, we use $V_{bins} = [10]mV$ to detect maximal events and $T_{bins} = [1]s$ for burst detection.

### 3.2.2 Biparametric sweeps

Biparametric sweeps such as Fig. 3.3 are obtained by computing long voltage traces of individual neurons or networks, as two parameters are varied across a grid. We use the fourth order Runge-Kutta method with fixed step size for numerical integration. The computation of these trajectories is parallelized on separate GPU threads using CUDA. Visualization is performed in Python. Appropriate combinations of $V_{bins}$, $T_{bins}$ and other criteria are chosen for symbolic encoding. Long-term behaviors of solutions are analyzed after omitting long transients. All shift-symmetric periodic sequences are normalized using a one-way hash function that produces identical hash value for all circular variations of a periodic sequence [189]. For example, the HCO burst in 3.2 can be represented by any of $(\overline{dcba})$, $(\overline{cbad})$, $(\overline{badc})$ or $(\overline{adcb})$, depending upon the length of the omitted transient. All of these are normalized to result in the same numerical hash value. Parameters resulting in topologically identical behaviors, result in the same hash value, and are shown in the same colors in the sweep. Chaotic traces are marked by aperiodic symbolic sequences, which are processed using the Lempel-Ziv (LZ) compression algorithm [4,190] to measure its complexity. The algorithm works by scanning a string, and adding new words to its

vocabulary continuously. The size of LZ-vocabulary towards the end, normalized by the length of the string, is used as the complexity measure. These are represented in the bi-parametric sweeps in gray shades, with darker gray representing greater LZ-complexity and greater instability. For biparametric sweeps of a HCO, we also track the average number of spikes per burst and enrich the sweep with this data (Fig. 3.5) when network burst is detected. When it not detected, the total number of spikes in each of cells $1$ and $2$ is used to differentiate between tonic spiking state, one cell suppressing the other, or quiescence (Fig.3.6). For the Dendronotus network, this is done using the spike numbers of cells $3$ and $4$, to determine the behavior of their HCO, as they undergo external synaptic influence from cells $1$ and $2$. Several biparametric sweeps can be evaluated and inspected together, as additional parameters are varied, as seen in 3.10 with additional third and fourth parameters. Compare this with 3.11 to see the affects of a fifth parameter. All the techniques and methods developed are open source and freely available at `https://bitbucket.org/pusuluri_krishna/deterministicchaosprospector/`

### 3.3 Extended Plant model

The equations of the extended Plant model [65] used for the swim CPG of the sea slug Melibe Leonina are given below:

$$\begin{aligned}
\dot{V} &= -I_{Na} - I_K - I_{Ca} - I_{KCa} - I_h - I_{leak} - I_{syn} \\
\dot{Ca} &= \rho[K_c x(V_{Ca} - V + Ca_{shift}) - Ca] \\
\dot{x} &= ((1/(e^{0.15(-V-50+x_{shift})} + 1)) - x)/\tau_x \\
\dot{z} &= [z_\infty(V) - z]/\tau_z(V), where\ z = h, n, y
\end{aligned} \tag{3.1}$$

This is a conductance based model employing the Hodgkin-Huxley formalism, with fast inward sodium current $I_{Na}$, outward potassium current $I_K$, slow TTX-resistant calcium current $I_{Ca}$ and an outward calcium sensitive potassium current $I_{KCa}$. In addition, there are also the generic ohmic leak current $I_{leak}$, h-current $I_h$, and synaptic current $I_{syn}$ (due

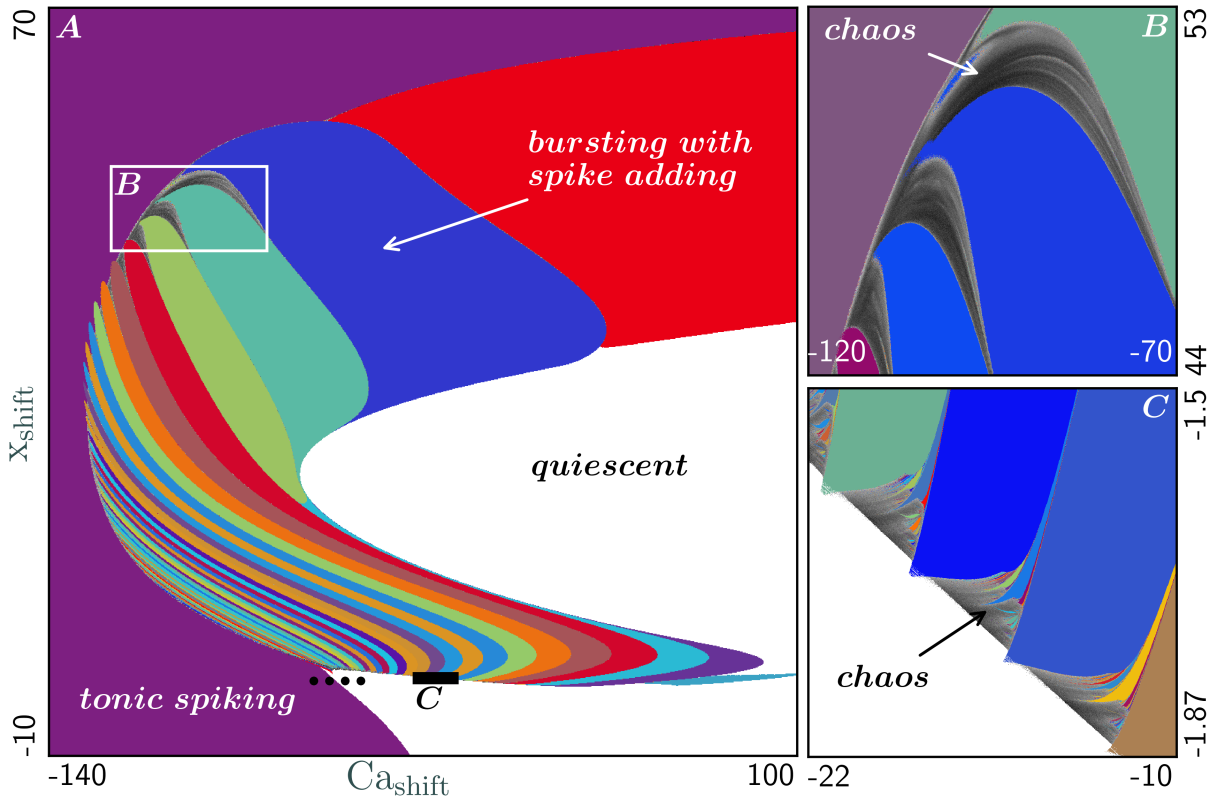


**Figure (3.3)** (A) Biparametric sweep of the extended Plant model showing a variety of activity types and transitions as the intrinsic properties of the cell are varied. Bursting, quiescence and tonic spiking are depicted in Fig. 3.4A and B. Chaotic (gray regions) spiking/bursting occurring near the boundary between bursting and tonic spiking is magnified in B and a sampled trajectory is shown in Fig. 3.4D. Chaotic mixed mode oscillations occurring near the boundary between bursting and quiescence are magnified in C, with a sampled trajectory depicted in Fig. 3.4C. Black dots near the bottom boundary between tonic spiking and quiescence in A mark four different sets of parameter values (left to right for Fig. 3.5 A to D) sampled for emergent HCO bursting from non-intrinsic bursters shown in Fig. 3.5.

to one or more presynaptic neurons). $Ca$ describes the intracellular calcium concentration given by the slowest equation. $h$, $x$, $n$, and $y$ represent the inactivation, slow activation, inactivation gating and h-current activation variables, respectively. Compared to the original Plant model of parabolic bursters for R15 neurons [188], two additional bifurcation parameters $Ca_{shift}$ and $x_{shift}$ were introduced for Melibe swim interneurons, which do not burst in isolation. The parameter $Ca_{shift}$ serves as an intrinsic parameter controlling the

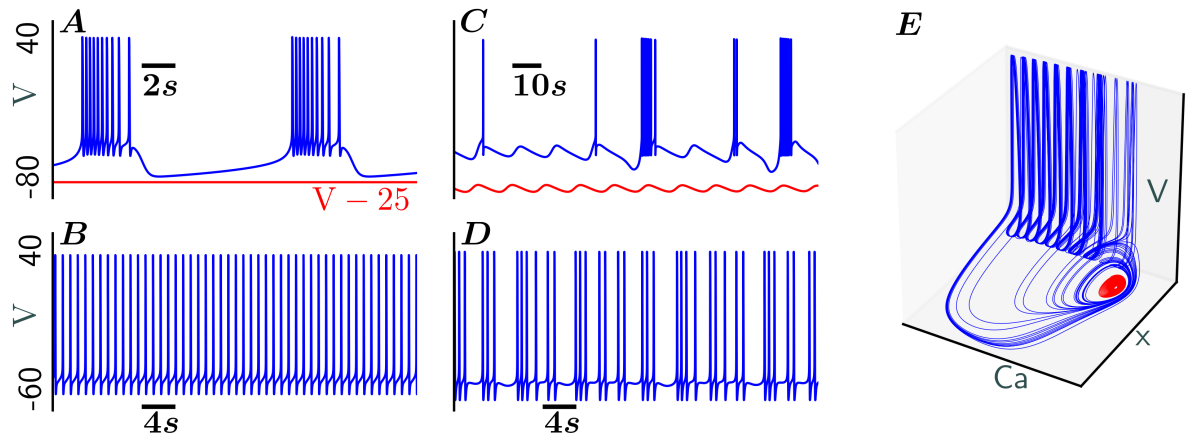


**Figure (3.4)** Repertoire of activity types shown by the extended Plant model. (A) Bursting with 10 spikes per burst (blue) and quiescence (red, shifted downwards by 25mV) (B) Tonic spiking (C) Bistability with chaotic mixed mode oscillations (blue) and hyperpolarized quiescent state (red, shifted downwards by 25mV) with spiral convergence, with the corresponding phase space projection shown in (E). The bistable states are separated by a saddle periodic orbit (not seen) that emerges following a subcritical Andronov-Hopf bifurcation. (D) Chaotic spiking/bursting

reversal potential of Calcium, which is known to vary between $80mV$ to $140mV$. The second parameter $x_{shift}$ modifies the dynamics of the slow variable $x$ and is used to eliminate bursting or hysteresis in the model. At $Ca_{shift} = x_{shift} = 0$, the system is similar to the original Plant model with intrinsic bursting. Further details of the model can be found in [65].

### 3.3.1 Isolated cell dynamics

Fig. 3.3 shows the biparametric sweep of the extended Plant model, depicting various activity types and transitions, as the intrinsic properties of the cell are varied. The model can exhibit bursting with spike adding, quiescence and tonic spiking, as well as two different modes of chaotic behavior. Example trajectories for different activity types are shown in Fig. 3.4. Near the boundary between tonic spiking and bursting, as shown in the magnification of Fig. 3.3B and the trajectory in Fig. 3.4D, chaotic spiking/bursting can occur. Alternatively, close to the boundary between quiescence and bursting, magnified

in Fig. 3.3C and the trajectory shown in Fig. 3.4C, chaotic mixed mode oscillations occur with an unpredictable number of spikes within bursts, separated also by an unpredictable number of subthreshold oscillations. The system is bistable along with a hyperpolarized quiescent state with spiral convergence, separated by a saddle periodic orbit that emerges following a subcritical Andronov-Hopf bifurcation.

### 3.3.2 Emergent HCO bursting from non-intrinsic bursters

In this section, we discuss the emergence of HCO bursting in a pair of identical non-intrinsic bursting cells given by Eq.3.1, mutually coupled with slow inhibitory synapses given by:

$$\begin{aligned} I_{syn} &= g_{inh} S(V_{post} - V_{rev}) \\ \dot{S} &= \alpha(1-S)/(1+e^{-10(V_{pre}+20)}) - \beta S/(1+e^{10(V_{pre}+20)}) \end{aligned} \tag{3.2}$$

Here, $V_{pre}$ and $V_{post}$ refer to the voltages in the pre- and post-synaptic cells, respectively, and $V_{rev}$ is the reversal potential of the ion channel. The parameters $g_{inh} = 0.01$, $\alpha$ and $\beta$ are set to be identical for both the synapses in the HCO. For the sake of simplicity, one may treat $\alpha$ as the amount of neurotransmitter released into the synapse from the presynaptic neuron and $\beta$ as the rate at which the neurotransmitter is removed from the synapse through reuptake or enzymatic degradation. As such, a strengthening synapse can be modeled by increasing $\alpha$ or decreasing $\beta$ values, while keeping $g_{inh}$ constant. These synaptic parameters can be regulated in neurophysiological experiments through dynamic clamp. Fig.3.5 shows four bi-parametric sweeps for the HCO (Fig. 3.2 left), composed of either both intrinsic tonic firing cells (A,B) or both quiescent (C,D), using parameters $x_{shift} = -2.$ and $Ca_{shift} = [-55., -50, -45, -40]$ sampled at the black dots in Fig. 3.3 near the boundary between tonic spiking and quiescence. As we vary the slow synaptic properties $\alpha_{inh}$ and $\beta_{inh}$ of mutual inhibition in the biparametric sweeps, we observe that the network can produce a variety of firing patterns including both cells tonically spiking (red regions),

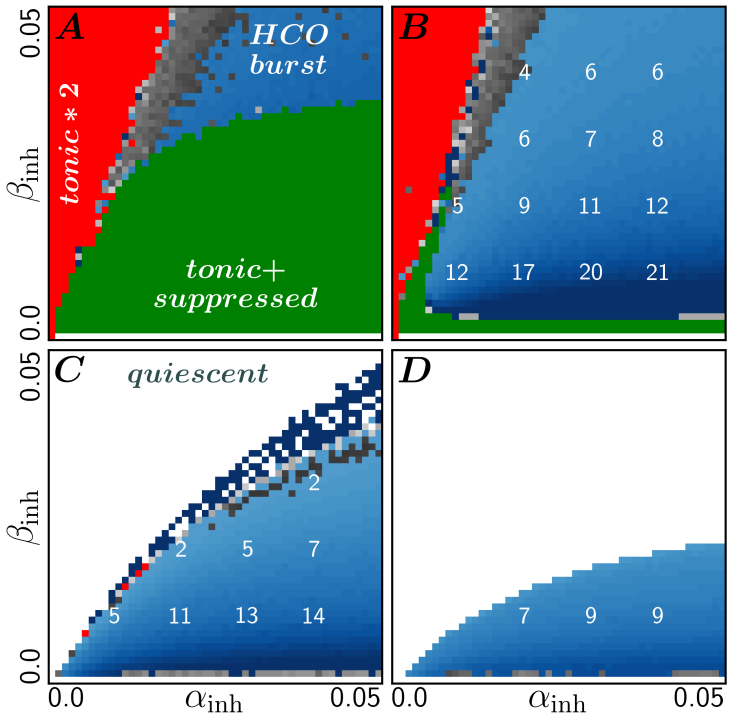


**Figure (3.5)** Emergent network bursting in a HCO composed of two identical neurons of the extended Plant model (Fig. 3.2 left), that are not intrinsic bursters. The intrinsic parameters for (A-D) are sampled along the black dots in Fig. 3.3 near the boundary between tonic spiking and quiescence with $x_{shift} = -2.$ and $Ca_{shift} = [-55., -50, -45, -40]$. Biparametric sweeps varying the slow synaptic properties $\alpha_{inh}$ and $\beta_{inh}$ of mutual inhibition, show how the intrinsic and synaptic parameters regulate network behaviors, including both cells tonically spiking (red), both cells quiescent (white), chaotic bursting (gray), one tonic firing cell suppressing the other into quiescence (green), as well as emergent HCO bursting (blue) superimposed with the average number of spikes per burst in cell $2$ (darker blue indicates higher spikes per burst). The neurons are intrinsic tonic spikers in A and B, while they are quiescent in C and D, in the absence of synapses. This is also seen by the respective red and white regions near weak synaptic coupling (at low values of $\alpha_{inh}$). As $x_{shift}$ and $Ca_{shift}$ values are sampled away from the boundary between tonic spiking and quiescence (as well as bursting) in Fig. 3.3, the regions of emergent HCO bursting (blue) vanish, see Fig. 3.8(right).

both cells quiescent (white), chaotic bursting (gray), one tonic firing cell suppressing the other into quiescence (green), as well as emergent HCO bursting (blue) superimposed with the average number of spikes per burst in cell $2$ (darker blue indicates higher spikes per burst). The presence of red tonic spiking regions near weak synaptic coupling (at low values of $\alpha_{inh}$) in A and B, and that of quiescence (white) in C and D is expected based

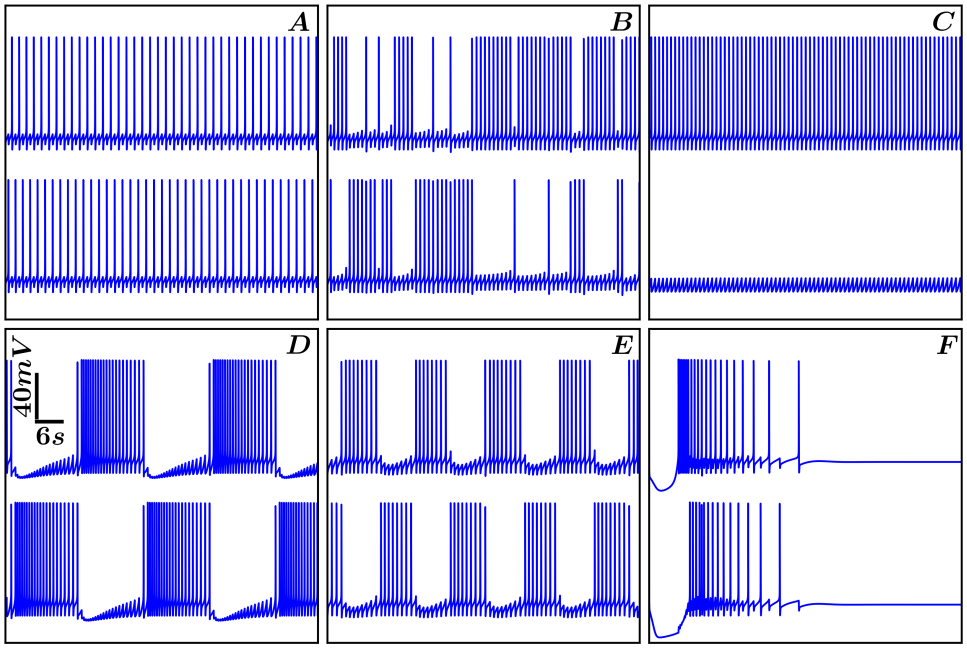


**Figure (3.6)** Voltage trajectories and emergent behaviors in a HCO (Fig. 3.2 left) of non-intrinsic bursters. (A) Both cells tonic spiking (B) Chaotic bursting and (C) One tonic spiking cell suppression the other into quiescence (D) Emergent bursting with 21 spikes per burst (E) Emergent bursting with 8 spikes per burst (F) Both cells return to stable quiescence after an external perturbation induces brief spiking. By virtue of symmetry in the network, at the parameter values for C, the system is bistable, where cell $2$ can also fire tonically suppressing cell $1$, depending on the initial conditions or external perturbations. A,B,C are sampled from Fig. 3.5A at $Ca_{shift} = -55$ for the slow synaptic parameters (A) $\alpha = 0.01$, $\beta = 0.04$ (B) $\alpha = 0.02$, $\beta = 0.04$ (C) $\alpha = 0.02$, $\beta = 0.01$. D, E are sampled from Fig. 3.5B at $Ca_{shift} = -50$ for the synaptic parameters (D) $\alpha = 0.04$, $\beta = 0.01$ for 21 spikes (E) $\alpha = 0.04$, $\beta = 0.03$ for 8 spikes per burst. F is sampled from Fig. 3.5C at $Ca_{shift} = -45.$, $\alpha = 0.01$ and $\beta = 0.04$.

on the intrinsic behaviors of the cells at these $Ca_{shift}$ values. The corresponding voltage trajectories are shown in Fig. 3.6A,B and C for both cells tonic spiking, chaotic bursting and one tonic spiking cell suppressing the other into quiescence at parameter values sampled from Fig. 3.5A. When cell $2$ can fire tonically and suppress cell $1$, by virtue of symmetry in the network, the system is bistable at these parameter values and cell $1$ can also suppress cell $2$, depending on the initial conditions or external perturbations. Emergent bursting with 21 spikes per burst and 8 spikes per burst are shown in Fig. 3.6D,E for parameters sampled from Fig. 3.5B. Fig. 3.5B shows the stable quiescent state for both

the cells, sampled in the white region of Fig. 3.5C. An external perturbation can briefly induce spiking in these cells, but they eventually return to quiescence. As the synapses are strengthened in Fig.3.5 through increasing values of $\alpha_{inh}$, or decreasing values of $\beta_{inh}$, the network transitions gradually through tonic spiking, chaotic bursting, emergent network bursting and suppression for the case of intrinsic tonic spikers (Fig.3.5A,B). For intrinsic quiescent cells (Fig.3.5C,D), the network transitions through quiescence, chaotic bursting and emergent network bursting as the synapse is strengthened gradually. If $x_{shift}$ and $Ca_{shift}$ values are sampled further away from the boundary between tonic spiking and quiescence (as well as bursting) in Fig. 3.3, the regions of emergent HCO bursting (blue) shrink and eventually vanish eliminating network bursts (compare with Fig. 3.8B). The parametric sweeps thus reveal how the synergistic interactions of intrinsic and synaptic properties control emergent bursting in the HCO, as well as other important properties such as the average number of spikes per burst.

### 3.4 Dendronotus model

The CPG governing the swimming behavior of the sea slug Dendronotus Iris is described in [ [2, 179, 180]]. The simplified 4-cell circuit and the bursting rhythm generated by the network model (described below) producing similar rhythmic output as seen in real animals are presented in Fig. 3.7. Such bursting oscillations of the network control the rhythmic motions of the animal during swimming. The network essentially consists of a pair of HCOs with synergistic interactions. Cells $1$ and $2$ mutually inhibit each other (blue connections), as do cells $3$ and $4$. In addition, there is a strong cross excitation (purple) from $3$ to $2$, and from $4$ to $1$, as well as inhibitory connections going in the opposite directions (blue). A pair of electrical cross connections also exist between these cells. Recent recordings due to A. Sakurai have shown that this could be a unidirectional rectified electrical coupling. In the absence of synaptic coupling, none of the cells burst intrinsically. Cells $1$ and $2$ are quiescent, while cells $3$ and $4$ are modeled as intrinsic tonic spikers. In the rest of this section, we will describe how parametric sweeps can be employed to

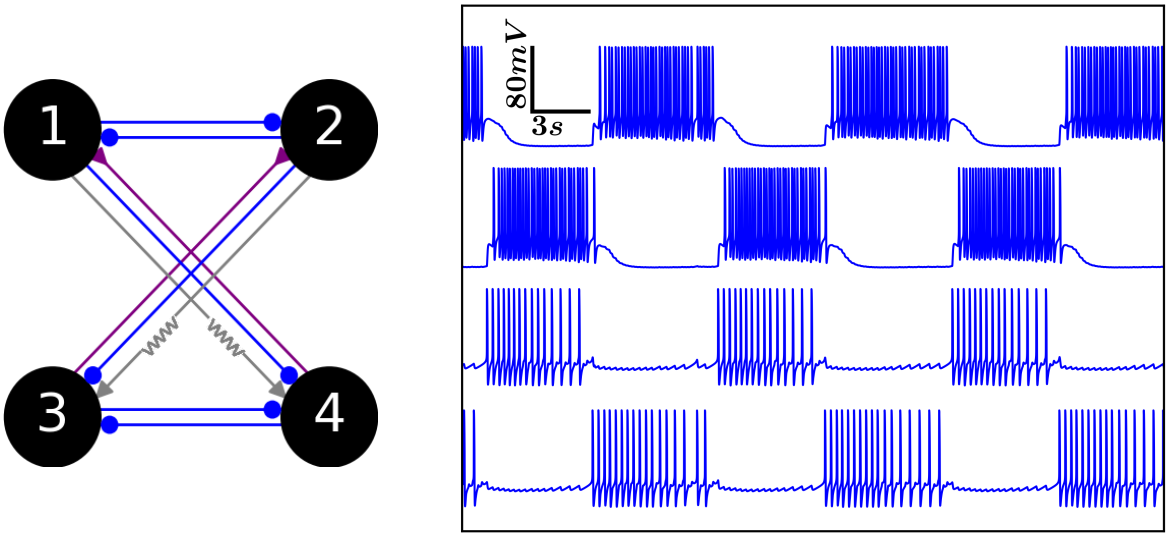


**Figure (3.7)** The simplified 4-cell circuit modeled after the Dendronotus swim CPG and the bursting rhythm generated by this network model, resembling typical neurophysiological recordings in the animal. The network consists of a pair of HCOs with synergistic interactions. Inhibitory, excitatory and rectified electrical connections are shown in blue, purple and gray, respectively. In the absence of synaptic coupling, none of the cells burst intrinsically, with cells $1$ and $2$ modeled as quiescent, and cells $3$ and $4$ as intrinsic tonic spikers. Parameter values for the network bursting rhythm (right) are given by $g_{14\_23\_inh} = 0.006$, $g_{41\_32\_exc} = 0.04$, $\alpha_{34\_43\_inh} = 0.04$, $\beta_{34\_43\_inh} = 0.006$, see Fig.3.11D at 18 spikes per burst.

study the synergistic interactions of various network parameters to produce successful network bursting oscillations and to control important properties such as the spikes per burst or burst durations as seen in Fig. 3.7 and Fig. 3.9C (with 18 or 14 spikes per burst in cell $4$, here). The model employed for this network is similar to the extended Plant model in Eq.3.1, although the individual properties of the synaptic currents are tuned to match experimental recordings, such as shorter spikes, faster sodium and potassium currents, scaled voltage dependent time rates etc. Detailed equations and parameters of the model can be found in the software repository accompanying this chapter at

`https://bitbucket.org/pusuluri_krishna/deterministicchaosprospector/`.

Inhibitory and excitatory connections are modeled using slow alpha synapses given by:

$$\begin{aligned} I_{syn} &= g_{inh\_or\_exc} S(V_{post} - V_{rev}) \\ \dot{S} &= \alpha_{inh\_or\_exc}(1 - S)/(1 + e^{-10(V_{pre}+20)}) - \beta_{inh\_or\_exc} S \end{aligned} \tag{3.3}$$

The default values of the synaptic connections, unless otherwise specified, are as follows. The network is bilaterally symmetric from left to right. As such, $g_{12\_inh} = g_{21\_inh} = g_{12\_21\_inh} = 0.02$ , represents the mutual inhibitory strength between cells $1$ and $2$, while the corresponding parameters controlling the synapse are given by $\alpha_{12\_21\_inh} = 0.04$ and $\beta_{12\_21\_inh} = 0.001$. The mutual inhibition is given by $g_{34\_43\_inh} = 0.04$, $\alpha_{34\_43\_inh} = 0.01$, $\beta_{34\_43\_inh} = 0.005$; cross excitatory coupling $g_{41\_32\_exc} = 0.08$, $\alpha_{41\_32\_exc} = 0.02$, $\beta_{41\_32\_exc} = 0.004$; cross inhibition $g_{14\_23\_inh} = 0.0055$, $\alpha_{14\_23\_inh} = 0.01$, $\beta_{14\_23\_inh} = 0.001$; and rectified electrical coupling $g_{14\_23\_elec} = 0.002$.

### 3.4.1 Absence of bursting in isolated cells and HCOs

Fig.3.8 (left) shows the $Ca_{shift}$ vs. $x_{shift}$ parametric sweep (left) of the Dendronotus neuron model. These neurons in isolation mostly produce tonic spiking or quiescence, with a smaller region of the parameter space corresponding to intrinsic bursting, compared to the extended Plant model in Fig. 3.3. The parameters $Ca_{shift} = -110.$, $x_{shift} = -3.5$ in the tonic spiking region (white dot) are chosen to model the intrinsic tonic spiker cells $3$ and $4$ in the network of Fig.3.7. We then analyzed the HCO of these cells varying the synaptic parameters $\alpha_{34\_43\_inh}$ and $\beta_{34\_43\_inh}$ in Fig.3.8 (right). This sweep shows that the HCO can only produce tonic spiking or suppression, but not emergent bursting, in the absence of synaptic connections with cells $1$ and $2$. Compare this sweep with Fig. 3.5 for a different HCO of the extended Plant model neurons, where emergent bursting can be seen.

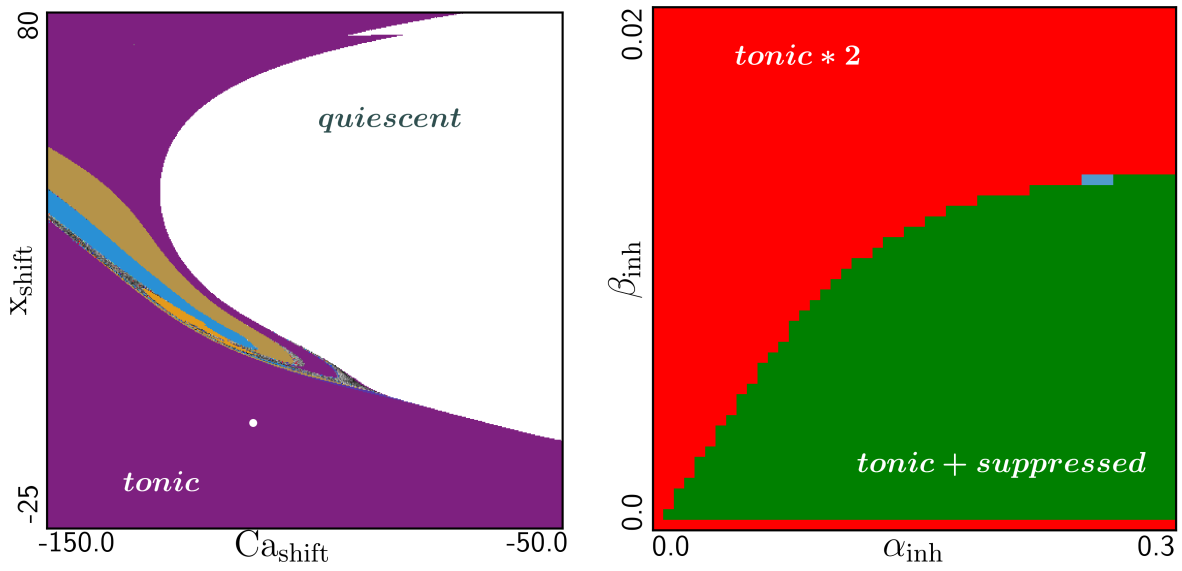


**Figure (3.8)** $Ca_{shift}$ vs. $x_{shift}$ parametric sweep (left) of the Dendronotus neuron model reveals that the neurons intrinsically produce mostly tonic spiking (purple) or quiescence (white), with very small regions of intrinsic bursting behavior, compared to the extended Plant model in Fig. 3.3. White dot ($Ca_{shift} = -110.$, $x_{shift} = -3.5$) in the tonic spiking region corresponds to the parameter values used to model the HCO between intrinsic tonic spiker cells $3$ and $4$ in the network of Fig.3.7. The parametric sweep of this HCO (right) as the synaptic parameters $\alpha_{34\_43\_inh}$ and $\beta_{34\_43\_inh}$ are varied, reveals that the HCO produces only tonic spiking or suppression, but not emergent bursting, in the absence of synaptic connections with cells $1$ and $2$.

### 3.4.2 Synergistic interactions of excitation, inhibition and electric coupling for emergent 4-cell bursting

For modeling the full 4-cell circuit, intrinsic parameters $Ca_{shift}$ and $x_{shift}$ for tonic spiking cells $3$ and $4$ are set at $Ca_{shift} = -110.$, $x_{shift} = -3.5$ (white dot in Fig. 3.8left), while those for the intrinsic quiescent cells $1$ and $2$ are set at $Ca_{shift} = 0.$, $x_{shift} = -3.5$ (in the white quiescent regions to the right, outside the plot boundaries of Fig. 3.8left). In the absence of all of cross inhibition, cross excitation and electrical coupling between the two HCOs, neither of the HCOs is capable of emergent bursting. The parametric sweep for the tonic spiking HCO between cells $3$,$4$ in Fig. 3.8right shows just tonic spiking and suppression. Such a sweep for the HCO between cells $1$,$2$ would have just the white

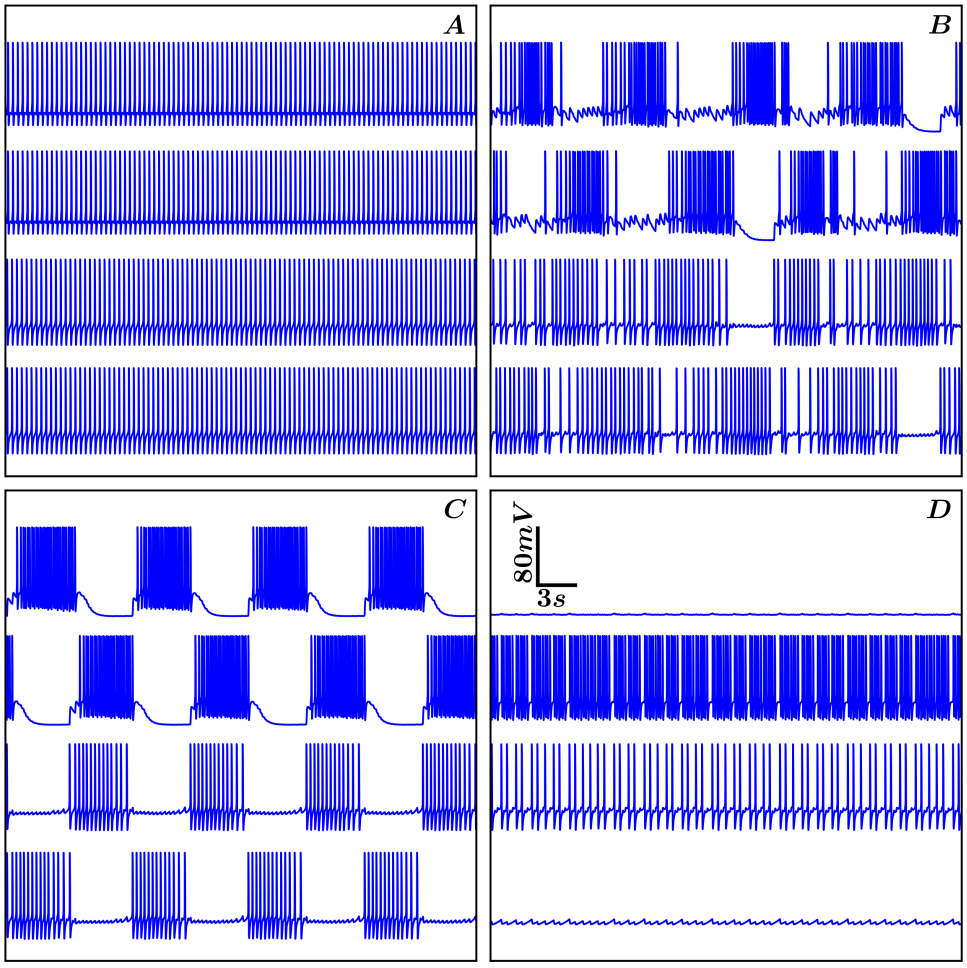


**Figure (3.9)** Activity types seen in the 4-cell network include (A) All cells tonic spiking (B) Chaotic spiking/bursting (C) Emergent network bursting (with 14 spikes per burst, here) and (D) Suppression. Parameter values given by $g_{41\_32\_exc} = 0.04$, $g_{14\_23\_inh} = 0.006$ (see Fig.3.11D); $\alpha_{34\_43\_inh}$ through $[0.004, 0.01, 0.02]$ and $\beta_{34\_43\_inh} = 0.008$ for A-C; $\alpha_{34\_43\_inh} = 0.04$ and $\beta_{34\_43\_inh} = 0.004$ for D;

quiescent region. In the following sections, we will keep the synaptic properties of the quiescent HCO between cells $1$,$2$ constant and study the behavior of the HCO between the tonic spiking cells $3$, $4$ and therefore, of the whole network, as modulated by cross excitation, cross inhibition and electrical coupling, as well as the synaptic properties of the mutual inhibition between cells $3$ and $4$. The voltage trajectories of activity types seen in the 4-cell network are shown in Fig.3.9. At parameter values given by $g_{41\_32\_exc} = 0.04$, $g_{14\_23\_inh} = 0.006$ (see Fig.3.11D), and $\beta_{34\_43\_inh} = 0.005$, the network can produce

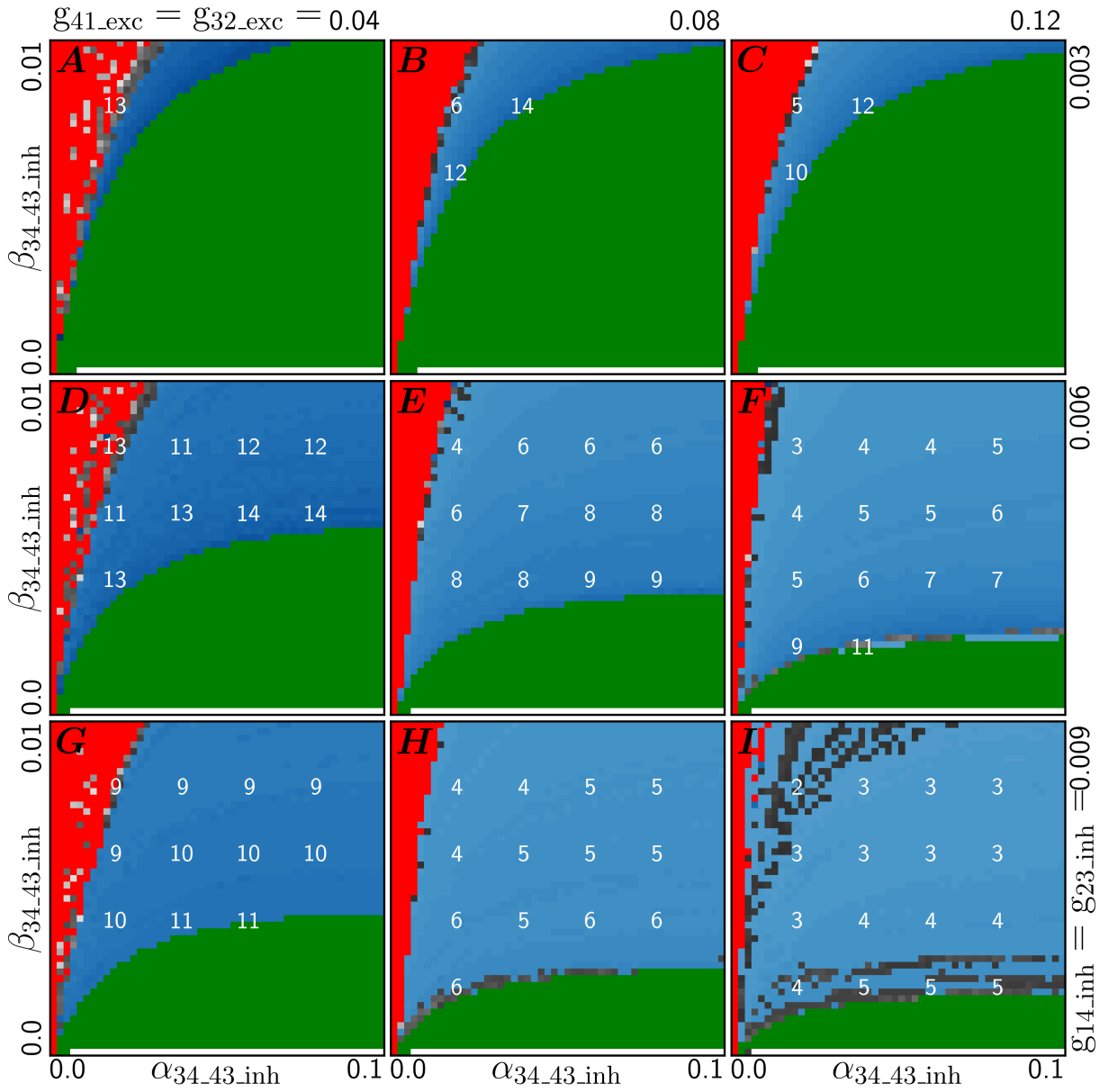


**Figure (3.10)** A grid of $\alpha_{34\_43\_inh}$ vs. $\beta_{34\_43\_inh}$ parametric sweeps, varying the cross excitation $g_{41\_32\_exc}$ horizontally, and the cross inhibition $g_{14\_23\_inh}$ vertically. Each individual sweep shows the network behavior as the synaptic properties of the mutual inhibition between the tonic spikers 3,4 are varied. The sweeps show that the synergistic interactions between various synapses can result in tonic spiking (red), chaotic bursting (gray), suppression (green) as well as emergent network bursting with varying number of spikes per burst (numbers for cell 4 are shown in bursting regions). Voltage trajectories are shown in Fig.3.9. Here, $g_{14\_23\_elec} = 0.001$. See Fig.3.11 for this grid at $g_{14\_23\_elec} = 0.002$

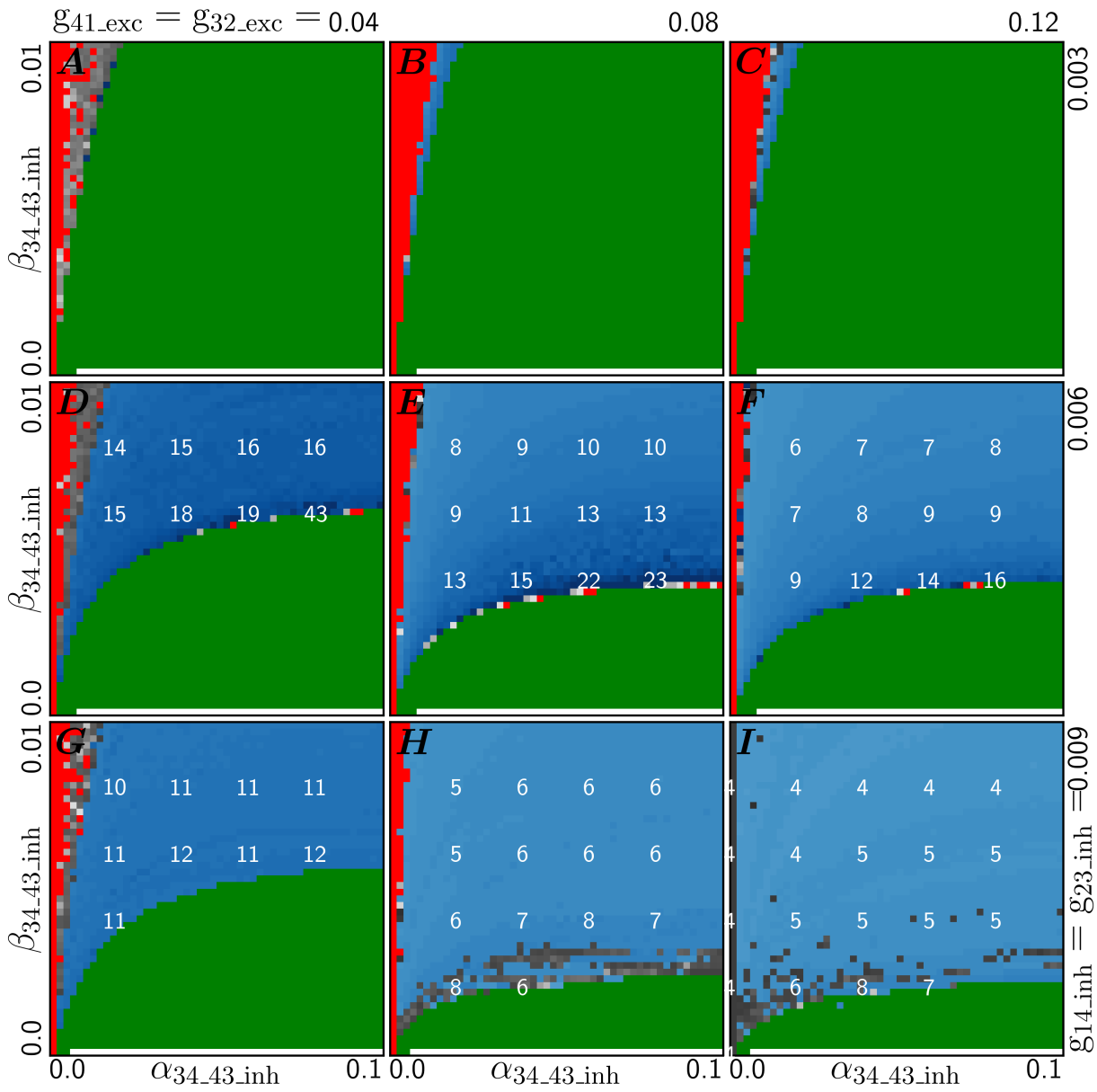


**Figure (3.11)** A grid of $\alpha_{34\_43\_inh}$ vs. $\beta_{34\_43\_inh}$ parametric sweeps, as we vary the cross excitation $g_{41\_32\_exc}$ horizontally, and the cross inhibition $g_{14\_23\_inh}$ vertically at $g_{14\_23\_elec} = 0.002$. Descriptions similar to Fig.3.10 at $g_{14\_23\_elec} = 0.001$.

different behaviors including all cells tonic spiking in Fig.3.9A, chaotic spiking/bursting in Fig.3.9B, and emergent network bursting (with 14 spikes per burst in cell 4, here) in Fig.3.9C, as the synaptic inhibition ($\alpha_{34\_43\_inh}$) between cells 3,4 is gradually increased through $[0.004, 0.01, 0.02]$. At $\alpha_{34\_43\_inh} = 0.04$ and $\beta_{34\_43\_inh} = 0.004$, we see suppression

of cell $4$ by cell $3$ ,or vice versa, (as well as suppression between cells $1$ and $2$) in Fig.3.9D. Compare the activity types of cells $3$,$4$ in these trajectories, with those seen in HCOs made from intrinsic tonic spiking neurons of the extend Plant model in Fig.3.5A,B which also show tonic spiking, chaotic bursting, emergent bursting and suppression.

Fig.3.10 shows a grid of parametric sweeps at $g_{14\_23\_elec} = 0.001$, varying the cross excitation $g_{41\_32\_exc}$ horizontally, and the cross inhibition $g_{14\_23\_inh}$ vertically. Each individual sweep shows the network behavior as the synaptic properties $\alpha_{34\_43\_inh}$ and $\beta_{34\_43\_inh}$ of the tonic spiking HCO cells $3$,$4$ are varied. The sweeps show that the synergistic interactions between various synapses can result in tonic spiking (red), chaotic bursting (gray), suppression (green) as well as emergent network bursting with varying number of spikes per burst. The voltage trajectories of the network are shown in Fig.3.9. Tonic spiking is seen for weak synapses (at low values of $\alpha_{34\_43\_inh}$), as expected from their intrinsic tonic spiking nature, while suppression is seen for strong synapses (at high values of $\alpha_{34\_43\_inh}$ or low values of $\beta_{34\_43\_inh}$). At moderate values of $\alpha_{34\_43\_inh}$ and $\beta_{34\_43\_inh}$ , emergent bursting and chaotic bursting (less pronounced) are seen. Increasing the cross inhibition as we move vertically upwards on the grid, the regions of emergent bursting diminish in size, while the number of spikes per burst increase. Increasing the cross excitation as we move horizontally on the grid, the size of emergent bursting regions remain almost the same, while the number of spikes per burst gradually decrease. The grid for $g_{14\_23\_elec} = 0.002$ is shown in Fig.3.11, with similar behaviors of cross excitation and cross inhibition. Increasing $g_{14\_23\_elec}$ from Fig. 3.10 to Fig. 3.11, results in smaller/vanishing regions of emergent bursting, while increasing the number of spikes per burst. Outside of these ranges of cross inhibition, cross excitation and electrical coupling, emergent bursting becomes less pronounced.

### 3.4.3 The role of excitation and inhibition in emergent 4-cell bursting

We end this section with a discussion of the individual roles of cross excitation, cross inhibition and the mutual inhibition between the tonic spiking HCO cells $3$,$4$ while all other

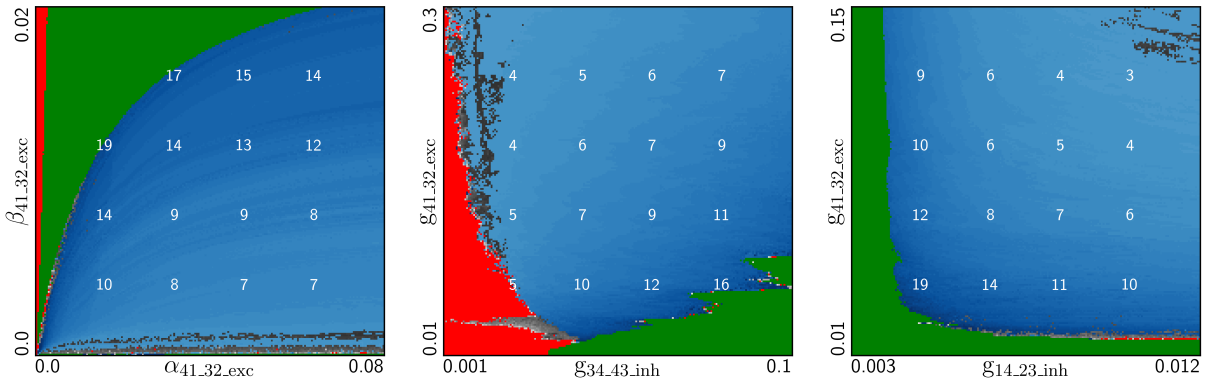


**Figure (3.12)** The role of excitation and inhibition is depicted, as all other network parameters remain constant. (left) Biparametric sweep of the slow synaptic properties $\alpha_{41\_32\_exc}$ and $\beta_{41\_32\_exc}$ of cross excitation shows tonic spiking (red) and suppression (green) at weaker strengths, while emergent bursting appears for stronger excitation (larger $\alpha$ values). (middle) Biparametric sweep of the strength of mutual inhibition of the tonic spikers $g_{34\_43\_inh}$ vs cross excitation $g_{41\_32\_exc}$ shows that for low values of $g_{41\_32\_exc}$, the network produces only tonic spiking or suppression. As we increase $g_{41\_32\_exc}$, emergent bursting can be seen at moderately strong mutual inhibition. Fig.3.12(right) inspects the role of cross inhibition $g_{14\_23\_inh}$ vs. cross excitation $g_{41\_32\_exc}$. For weak synaptic strengths in either, we see suppression (green). Emergent bursting is seen at moderate values of both, with the number of spikes per burst decreasing at larger values.

parameters remain constant. It was shown in [ [179]] that cross excitation plays an important role in emergent bursting and removing the cross excitation can suppress network bursting. Fig.3.12left shows a biparametric sweep as we vary the slow synaptic properties $\alpha_{41\_32\_exc}$ and $\beta_{41\_32\_exc}$ of this cross excitation. For weak excitatory synapses, we see tonic spiking (red) and suppression (green), while emergent bursting appears at stronger synapses (larger $\alpha$ values). This can be elaborated further in Fig.3.12(middle) showing the biparametric sweep of the strength of mutual inhibition of the tonic spikers $g_{34\_43\_inh}$ vs cross excitation $g_{41\_32\_exc}$. For zero or low values of $g_{41\_32\_exc}$, the network produces only tonic spiking or suppression, as the mutual inhibition of the tonic spikers $g_{34\_43\_inh}$ is increased. This is expected from their intrinsic nature as well as seen from the parametric sweep for the tonic spiker HCO in Fig. 3.8(right). As we increase $g_{41\_32\_exc}$, emergent bursting can be seen at moderately large values of the mutual inhibition. Fig.3.12(right) inspects the role of cross inhibition $g_{14\_23\_inh}$ vs. cross excitation $g_{41\_32\_exc}$. For weak

synaptic strengths in either, we see suppression (green). Emergent bursting is seen at moderate values of both, with the number of spikes per burst decreasing at larger values. These results confirm the essential role of both cross excitation and cross inhibition.

### 3.5 Summary

We adapted our toolkit, Deterministic Chaos Prospector, and presented a powerful approach of symbolic dynamics and parametric sweeps to study complex behaviors arising in neuron models, and emergent network phenomena in neural circuits. We discussed a variety of activity types in individual neurons, the onset of half-center bursting oscillations from non-intrinsic bursting cells, as well as emergent 4-cell bursting dynamics in the Dendronotus network model, where the individual cells or the HCOs can not produce bursting, without the synergistic interplay of excitation, inhibition and electric coupling in the full network. We explored detailed transitions and the roles of various intrinsic cell properties and the synaptic dynamics. Our approach can be employed to study the effects of several realistic and essential network parameters, that can be manipulated in neurophysiological experiments. Future work could include detailed modeling and fitting of the parameters, integrating with experimental data. For larger networks, with several tens or hundreds of parameters, these symbolic methods may be employed for a detailed study of the essential parameters, in conjunction with other machine learning and parameter optimization techniques based on cost functions for error minimization between observed and modeled behaviors.

# CHAPTER 4

# COMPUTATIONAL EXPOSITION OF MULTISTABLE RHYTHMS IN 4-CELL NEURAL CIRCUITS

The co-existence of multistable rhythms generated by oscillatory neural circuits made up of 4 and more cells, their onset, stability conditions, and the transitions between such rhythms are not well understood. This is partly due to the lack of appropriate visual and computational tools. In this chapter, we employ modern computational approaches including unsupervised machine learning (clustering) algorithms and fast parallel simulations powered by graphics processing units (GPUs) to further extend our previously developed techniques based on the theory of dynamical systems and bifurcations. This allows us to analyze the fundamental principles and mechanisms that ensure the robustness and multifunctionality of such neural circuits. In addition, we examine how network topology affects the dynamics, and the rhythmic patterns transition/bifurcate as network configurations are altered and the intrinsic properties of the cells and the synapses are varied. This chapter elaborates on a set of inhibitory coupled 4-cell circuits that can exhibit a variety of mono- and multistable rhythms including pacemakers, paired half-centers, traveling-waves, synchronized states, as well as various chimeras. Our detailed analysis is helpful to generate verifiable hypotheses for neurophysiological experiments with biological central pattern generators. This chapter is edited with permission based on the publication and further details on multistability of 4-cell networkss can be found in [191]. Detailed multistability analysis of symmetric and asymmetric 3-cell networks can be found in [182].

## 4.1 Multistability in Central Pattern Generators

Rhythmic oscillations underlie a variety of sensory, motor and cognitive functions. Brain disorders such as schizophrenia, epilepsy, autism, Alzheimer's disease, and Parkin-

son's disease are characterized by dysfunction of neural oscillations. As such, mechanisms underlying rhythmic activities can help in designing therapeutic interventions for such conditions. Brain networks are composed of smaller structural and functional building blocks of neural networks called *motifs* [1, 8–10]. Such motifs have been identified in various animal central pattern generators (CPGs), which are biological neural networks producing rhythmic motor output without sensory feedback or central input. Rhythmic patterned motor activity under the control of CPGs is widespread across many vertebrate and invertebrate species in a diversity of neural networks including ones governing locomotion, swimming, respiration and heartbeat [1, 11–23]. As networks evolve and become more complex, the existing motifs are preserved while new elements are added to maximize the available number of configurations and to support the robustness of the networks [1, 24–26]. For example, a common constituent of many known CPGs is a half-center oscillator (HCO) that is made up of 2 bilaterally symmetric neurons that reciprocally inhibit each other to produce alternating bursting patterns in anti-phase. Multiple HCOs can be combined using chemical and/or electrical synapses to form complex modular CPG networks such as the well described swim CPGs in sea slugs *Melibe leonina* and *Dendronotus iris* [17, 25, 27–32]. In order to gain insights into the dynamical principles that regulate the behaviors of larger networks, it is essential to understand the workings of individual neurons as well as the basic motifs. Mathematical modeling studies at multiple levels ranging from isolated neurons to small networks and populations have resulted in significant understanding of the working principles of biological neural networks [33–39].

A fundamental challenge in theoretical and experimental research on CPGs is to understand the mechanisms by which such neural networks can adapt structurally and functionally to serve as dedicated circuits for monostable rhythms, or as multifunctional circuits producing several stable rhythmic behaviors [2, 26, 38, 60–65]. Moreover, intrinsic capability for rhythm switching, such as gait transitions in locomotion and changes in the direction of blood flow in leeches, can be accomplished by input-driven perturbations that switch between multiple attractors representing various rhythmic patterns generated by

a multistable CPG [24, 66–68]. In addition, these attractors, which can be fixed points or periodic orbits, can bifurcate – lose stability or vanish, thereby explaining the continuous or the sudden transitions in the system state due to changes in network connectivity, external inputs and the intrinsic dynamics of individual neurons [49]. The emergence of stable polyrhythms, and their transitions, exhibited by half-center oscillators and 3-cell motifs, along with their dynamics under the influence of external input and varying chemical (inhibitory and excitatory) and electrical synaptic connectivity, have been thoroughly demonstrated using Poincaré return maps for phase lags (described in the next section) and other techniques. Note that 4-cell circuits and more complicated CPGs that produce dedicated functionality have also been studied in real animals as well as computational models [1, 18–24, 60, 192–196]. The basic principles underlying the co-existence and stability of multiple rhythms in 4-cell networks and larger CPGs have long remained unclear, in part, due to the exponentially increasing algorithmic complexity and computational costs needed to systemically explore such networks. Another major problem with using approaches like Poincaré return maps for larger networks is that, unlike the 3-cell circuits that are well described by 2-dimensional (2D) maps, the corresponding well populated maps for larger networks become 3D and higher dimensional, which are hard to analyze visually.

Traditional computational approaches using single threaded computing fall short both in terms of the amount of time required for the computations as well as the breadth and comprehensiveness that could be achieved. Recent advances in parallel processing and GPU computing with technologies such as CUDA, OpenAcc, OpenMP and OpenMPI offer tremendous performance improvements and make it possible to study problems in neuroscience and nonlinear dynamics that could not be solved earlier [3–5, 47, 48]. In this chapter, we will address the lack of such visual and computational tools and further extend the developed techniques based on dynamical systems theory for neuroscience applications by implementing elements of unsupervised machine learning for clustering analysis in higher dimensions [40–46] and GPU parallelization for faster simulations of densely

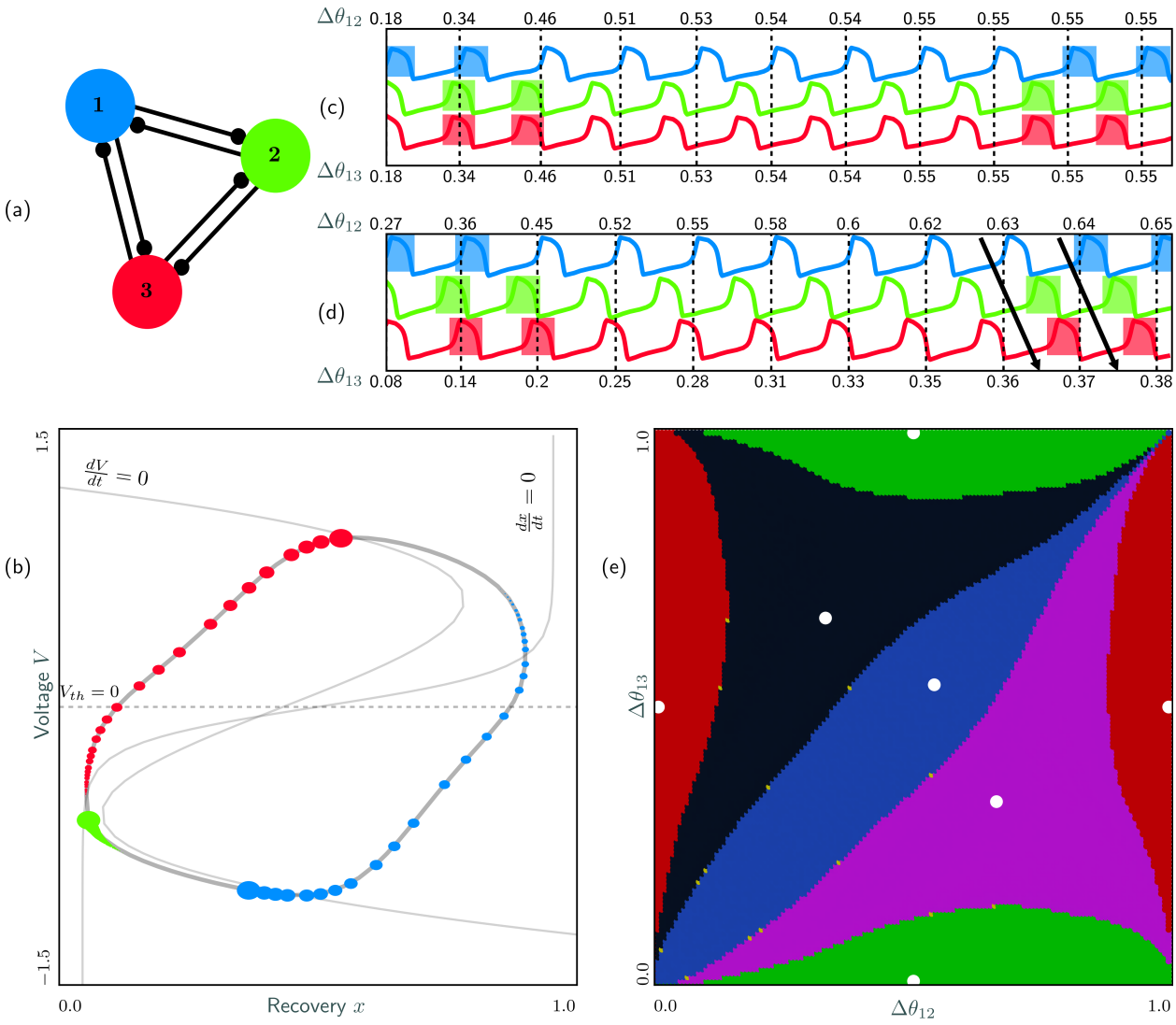


**Figure (4.1)** A fully connected 3-cell network of the generalized Fitzhugh-Nagumo type cells with mutually inhibitory synapses is shown in (a). The phase space of a neuron (under weak coupling) is depicted in (b), with the slow recovery variable $x$ and the fast voltage variable $V$, superimposed with the corresponding nullclines (light gray): slow $\frac{dx}{dt} = 0$ and fast $\frac{dV}{dt} = 0$, and the limit cycle (dark gray). The colored dots depict the phase space coordinates of the three coupled cells traversing the limit cycle to generate a traveling-wave pattern. Horizontal dashed line represents the activation threshold $V_{th}$. Two long trajectories converging towards (c) the blue pacemaker rhythm $(\Delta\theta_{12}\ ,\ \Delta\theta_{13}) = (0.55, 0.55)$ or (d) the clockwise traveling-wave rhythm $(\Delta\theta_{12}\ ,\ \Delta\theta_{13}) = (0.67, 0.33)$ are shown. Evolution of the phase lags $\Delta\theta_{12}$ and $\Delta\theta_{13}$ at those moments when the reference cell 1 (blue) crosses above the threshold (vertical dotted lines) are shown at the top and the bottom, respectively. Multistability analysis (e) of the network using 2D Poincaré return map on a grid of $70 \times 70$ initial conditions or phase lags between the reference cell 1, and cells 2 and 3. All the initial conditions that converge to the same attractor are shown in identical colors to visualize the attraction basins of the five co-existing fixed points (shown as white dots), representing five stable rhythms of the circuit. These are 3 pacemaker (red, green, and blue) and two travelling wave (pink - clockwise, black - anti-clockwise) rhythms. Here, $I_{app} = 0.426$, $g_{inh} = 0.01$ and $\varepsilon = 0.3$.

populated trajectories in such coupled circuits. By combining the analytical tools with these computational approaches, we deconstruct the operating rules for the co-existence, stability and robustness of stable polyrhythms in complex CPGs. We demonstrate the effectiveness of this approach in homogenous 4-cell neural circuits with inhibitory coupling and show how network topologies, intrinsic and extrinsic parameters result in bifurcations and alter network behaviors. The development and incorporation of such mathematical and computational tools is essential to unravel the multifarious behaviors arising in neuroscience. The methods developed are interdisciplinary with applications to complex dynamical systems and networks of coupled oscillators ranging across (electro)chemical reactions, population dynamics, electronic circuits, nonlinear optics, regulatory genetic networks and excitatory dynamics of cellular membranes and heart beats, to name a few.

## 4.2 Models and numerical methods

We construct our neural circuits using identical neurons of a *generalized* Fitzhugh-Nagumo type with a cubic fast nullcline and a sigmoidal slow nullcline as described in [68]. The equations are given by:

$$\begin{aligned} \frac{dV_i}{dt} &= V_i - {V_i}^3 - x_i + I_{app} + \sum_{j \neq i} g_{inh}^{ji}\, G(V_i, V_j) \\ \frac{dx_i}{dt} &= \varepsilon\, [x_\infty(V_i) - x_i] \end{aligned} \tag{4.1}$$

The voltage variable $V_i$ and the recovery variable $x_i$ together determine the state of the $i^{th}$ neuron. The parameter $\varepsilon$ for time-scale separation determines the slow dynamics of $x_i$ with respect to $V_i$; the slow nullcline $\frac{dx_i}{dt} = 0$ is given by the sigmoidal function:

$$x_\infty(V_i) = \frac{1}{1 + e^{-10\ (V_i - V_{sh})}} \quad \text{where} \ \ V_{sh} = 0.$$

Parameter values are initially chosen so that the system has a unique repelling equilibrium state at the intersection of the middle, unstable branch of the $V$-nullcline (where

$\frac{dV}{dt} = 0$) and the slow $x$-nullcline (where $\frac{dx}{dt} = 0$), surrounded by a stable limit cycle, as shown in Fig. 4.1b. The reciprocal interactions between these two variables result in oscillatory behavior through dynamical hysteresis where the voltage variable becomes bistable between the active ($V_i \geq V_{th}$) and the inactive ($V_i < V_{th}$) states for a fixed value of the recovery variable, with the activation threshold given by $V_{th} = 0$. Relaxation oscillations are constituted by the relatively slow transient active and inactive meta-states and the fast switching between the corresponding branches (for $0 < \varepsilon < 1$). The external drive $I_{app}$ horizontally shifts the position of the $V$-nullcline and controls the release and escape mechanisms of the otherwise stationary states of the neuron [68]. The parameter range for $I_{app}$ is chosen between $0.4$ and $0.6$, where the cells produce intrinsic bursting-like behaviors. Below and above this range, the cells become quiescent and tonic spiking, respectively.

Inhibitory synaptic coupling between the neurons in a network is modeled using fast-threshold modulation with a sigmoidal coupling function. An inhibitory synapse, due to $E_{rev} = -1.5$, from neuron $j$ to neuron $i$, with strength $g_{inh}^{ji}$ in equation (4.1) is given by

$$G(V_i, V_j) = (E_{rev} - V_i)\,\Gamma(V_j), \text{ where } \Gamma(V_j) = \frac{1}{1 + e^{-100\,(V_j - E_{th})}}, \text{ and } E_{th} = 0$$

The voltage variable $V_i$ is driven by a summation of such synaptic inputs from all other neurons $j \neq i$ in the circuit. Identical values are used for all the synaptic strengths $g_{inh}^{ji}$ within a network, except where specified otherwise. The range for $g_{inh}$ is chosen between $0.005$ and $0.03$ for stable network bursting. For very large values of $g_{inh}$ beyond this range, a cell in the active state forcibly drags down the other cells due to strong synaptic inhibition, and various chimera-like behaviors described later become more prominent. The external drive $I_{app}$, the time-scale constant $\varepsilon$, and the network coupling strength $g_{inh}$ serve as key bifurcation parameters that determine the circuit dynamics. The choice of the model used in the chapter provides computational simplicity while retaining the essential dynamical features and mechanisms of rhythmogenesis seen in the detailed Hodgkin-Huxley type of neuronal models. Further details of this neuron model and the multistability

analysis of 3-cell networks can be found in [68], while such analysis for detailed Hodgkin-Huxley type of neurons is presented in [24].

### 4.2.1 Poincaré return maps for phase lags

Figure 4.1a shows a 3-cell motif comprised of generalized Fitzhugh-Nagumo type neurons with mutually inhibitory synapses, as described by equations (4.1). Figures 4.1c,d show two voltage traces that converge to stable pacemaker (blue) and traveling-wave (clockwise) rhythms with phase-locked states in this network. The possible polyrhythms in such 3-cell motifs have been previously described using Poincaré return maps for phase lags (see Fig. 4.1e) to determine the attraction basins, stability and bifurcations of the fixed points corresponding to phase locked states in the voltage patterns [24,63,64,68,197,198]. These maps are built using specific events in time when the cells cross the threshold voltage from below. A sequence of phase lags is defined for each cell, as the delay in the burst initiation of a reference cell with respect to that of this cell, normalized over the bursting period. Thus, in the 3-cell CPG shown in Fig. 4.1a, if $t_1^n$, $t_2^n$, and $t_3^n$ represent the times at which cell 1 (blue), cell 2 (green) and cell 3 (red) cross the threshold for the $n^{th}$ time, using cell 1 as the reference cell, the ($n^{th}$) phase lags are given by:

$$\Delta\theta_{12} = \frac{t_1^{n+1} - t_2^n}{t_2^{n+1} - t_2^n} \text{ and } \Delta\theta_{13} = \frac{t_1^{n+1} - t_3^n}{t_3^{n+1} - t_3^n}$$

Ordered pairs of phase lags ($\Delta\theta_{12}$, $\Delta\theta_{13}$) are used to construct a Poincaré return map in the 2D discrete phase space. A sequence of ordered pairs yields a forward phase trajectory on a 2D torus (Fig. 4.1e), which maps the phases of cells 2 and 3 with respect to the reference cell 1, defined for values between $0$ and $1$. A phase lag of either $0$ or $1$ represents an in-phase relationship with the reference cell while a phase lag of $0.5$ represents an anti-phase relationship. A fixed point in the system corresponds to a stable rhythmic oscillatory pattern that arises out of well defined phase lags between the burst initiations of individual neurons of the CPG, which remain phase-locked over time. All trajectories

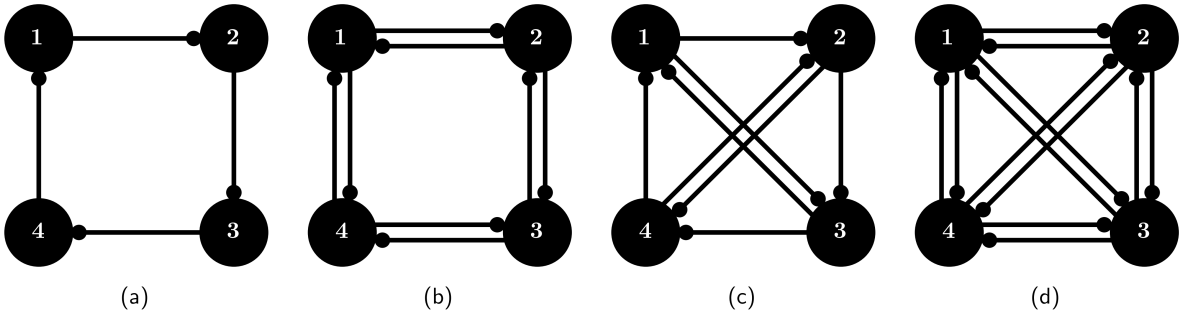


**Figure (4.2)** Homogenous network topologies for 4-cell circuits with inhibitory synaptic coupling between neurons: (a) One-way inhibitory loop (b) Two-way inhibitory loop (c) Mixed (d) Fully connected. In each of these network configurations, all the neurons have identical parameter values and receive the same number of incoming synapses of identical strengths.

starting from a wide range of initial phase lags that converge to the same fixed point or stable rhythm are marked by identical colors, depicting the attractor of the rhythm in the phase space. By analyzing the phase space of the Poincaré map, it is possible to predict the characteristics of the rhythmic behaviors of the corresponding CPG. The Poincaré map in Fig. 4.1e reveals the existence of a penta-rhythmic state in the CPG with 3 pacemakers (blue - Fig. 4.1c, green and red) and two traveling-waves (pink - Fig. 4.1d, black). The blue, green and red pacemakers correspond to the fixed points on the Poincaré map represented by the ordered pairs $(0.5, 0.5)$, $(0.5, 0)$ and $(0, 0.5)$ respectively, for the phase lags ($\Delta\theta_{12}$, $\Delta\theta_{13}$), while the clockwise (pink) and anti-clockwise (black) traveling-waves are represented by $(0.67, 0.33)$ and $(0.33, 0.67)$, respectively. Using Poincaré return maps for phase lags, the problem of existence and stability of multiple bursting rhythms in the CPG is reduced to the bifurcation analysis of fixed points, attractors and invariant cycles in the system.

### 4.2.2 Unsupervised machine learning

In order to analyze multistability of larger networks whose corresponding Poincaré return maps are of dimension 3D and higher, we employ unsupervised machine learning

techniques to computationally evaluate the attraction basins of the stable polyrhythms (read stable fixed points), and analyze their corresponding bifurcations. We investigate multi-stable dynamics in homogenous networks comprised of 4 generalized Fitzhugh-Nagumo type neurons given by equations (4.1), with identical mutual inhibition between neurons. Such a model provides computational simplicity while showing the dynamics topologically similar to more complex models based on the Hodgkin-Huxley formalism [24, 68]. For meaningful application of Poincaré maps, homogeneity ensures similar bursting periods across different neurons by $(1)$ using identical parameter values for all the neurons and $(2)$ keeping the sum of the synaptic strengths of all the inputs received by a neuron the same as those of any other neuron in the network. Figure 4.2 shows various homogenous network topologies for the 4-cell circuits, with gradually increasing complexity, starting from the one-way inhibitory loop (Fig. 4.2a), to the two-way inhibitory loop (Fig. 4.2b), to the mixed network (Fig. 4.2c), and finally the fully connected network (Fig. 4.2d).

We analyze the Poincaré return maps using hierarchical clustering schemes [40–46]. We begin by first identifying multiple initial conditions with varying phase lags for the cells, spread out uniformly across the 3D phase torus on a $(25 \times 25 \times 25)$ grid. For each of those initial conditions, we obtain long traces of firing activity of the circuit and compute the corresponding phase trajectory of ordered tuples ( $\Delta\theta_{12}$ , $\Delta\theta_{13}$, $\Delta\theta_{14}$ ) of phase lags. Using clustering methods, all the trajectories from different initial conditions that converge to a very close neighborhood of each other are determined to be within a cluster. This is done by first identifying the converging ordered tuples of phase lags for each trajectory and then performing agglomerative hierarchical clustering with complete linkage on those converging ordered tuples. Since the phase lags are defined on the 3D torus with modulo-1, implying the phase lags $0.0$ and $1.0$ are identical, the distance metric for clustering the converging phase lag ordered tuples was obtained as the sum of squares of the smallest difference along each dimension, wrapping around the phase torus. For example, the smallest difference between the phase lags $0.05$ and $0.95$ is $0.1$ and not $0.9$, as we wrap around. The circular mean of all the phase lag ordered tuples within

**Table (4.1)** Multistability analysis of the fully connected 4-cell CPG (Fig. 4.2d) with 3D phase torus of Poincaré maps is simplified using clustering to reveal three stable paired half-center rhythms.

| CCM | CCSD | PC |
|---|---|---|
| (0.5, 0., 0.5) | (0., 0., 0.) | 33.2% |
| (0.5, 0.5, 0.) | (0., 0., 0.) | 33.5% |
| (0., 0.5 ,0.5) | (0., 0., 0.) | 33.2% |

$g_{inh} = 0.025$, $I_{app} = 0.575$ and $\varepsilon = 0.5$

a cluster defines the fixed point or the stable rhythm marked by the cluster. We also measure the circular standard deviation to reflect the degree of variability within a cluster. Circular means and circular standard deviations are rounded to two decimal points. The total number of initial conditions whose trajectories converge to each cluster serves as a measure for the relative size of the attraction basin of the stable rhythm. Numerical integration is performed using the fourth order Runge-Kutta method with a fixed step size. Computation of neural trajectories and phase lags, and parallelization across GPU threads is achieved using CUDA and OpenAcc [6]. Clustering analysis and visualizations are done using Python. The software tools developed are open source and available at `https://bitbucket.org/pusuluri_krishna/cpg_multistability`. The multistablity results obtained remain generally consistent across a reasonable range of values for the settings of the clustering algorithm, with the values becoming significant near bifurcations where fixed points (and therefore, the clusters) undergo transitions.

For example, the Poincaré return map on the 3D phase torus for the fully connected 4-cell circuit (see Fig. 4.2d) has three distinct attractors (with green, blue, and red basins) of the paired half-center rhythms, where two pairs of cells fire in anti-phase while cells within a pair fire in synchrony (see Fig. 4.4 paired half-center). The phase lag ordered tuples ( $\Delta\theta_{12}$ , $\Delta\theta_{13}$, $\Delta\theta_{14}$ ) for these rhythms are given by $(0.5, 0., 0.5)$, $(0.5, 0.5, 0.)$, and $(0., 0.5, 0.5)$ for the green, blue, and red attractors, respectively. Constructing and decoding such 3D phase space trajectories visually is rather hard and time consuming. Table 4.1

illustrates the results of the clustering approach to automate the detection of these multistable states (fixed points), the phase relationships of the cells at these attractors, the degree of variability in their convergence, and the relative sizes of the attraction basins of various rhythmic states by means of cluster circular means (CCM), cluster circular standard deviations (CCSD) and the percentage of convergence (PC). We emphasize that GPU parallelization allows this multistability analysis to be performed within just a couple of minutes.

While phase dynamics and the parametric sweeps such as Fig. 4.3 effectively portray the broad picture of system dynamics for stable network bursting, we note that several other chimera-like behaviors are also seen at very strong synaptic inhibition. It is also possible that there could be small regions or transitory periods within the parameter ranges studied, that can also exhibit chimera like rhythms, but are not seen here as only a few discrete parameter values are used in constructing these sweeps. Depending on the objective of parametric exploration and the rhythms under consideration, future work could focus on particular transitions and perform detailed sweeps near those regions to obtain such states, as well as enhance such sweeps by incorporating other details such as amplitude differences during post processing to, say, distinguish between the fully synchronous states and the phase synchronous states highlighted later.

We investigate the multistable rhythms generated by various homogenous network configurations of 4-cell CPGs given in Fig. 4.2. We find the network topologies that drive monostable or multistable behaviors. We also identify the transitions occurring in these networks as parameters such as the synaptic and external drives are varied, to determine the principles underlying stable polyrhythms in such networks.

## 4.3 Multifunctionality repertoire of the fully connected network

Figure 4.3 is an illustration of the multistability and bifurcation analysis performed on the fully connected 4-cell circuit, as we vary two parameters of the network, the synaptic strength ($g_{inh}$) and the external drive ($I_{app}$), on a $7 \times 6$ grid, while keeping a fixed $\varepsilon = 0.5$.

For each set of parameters in the grid, clustering analysis of Poincaré return maps of the 3D torus is performed to identify the stable rhythmic behaviors (clusters). Each block in the grid represents the clusters and the rhythmic behaviors identified for the particular parameter values. The rhythmic state associated by each cluster is given by the cluster circular mean (CCM). Homogeneity and symmetry of the network imply that, for every stable rhythm in the network, one can find stable symmetric variations of the rhythm obtained by circular permutations or relabeling of the identical cells in the network. We will refer to such coexisting rhythms as isomorphisms. For example, the orange block marked $A$ at $g_{inh} = 0.025$ and $I_{app} = 0.575$ represents the existence of 3 stable isomorphisms of the paired half-center rhythms whose phase lag ordered tuples $(\Delta\theta_{12}\ ,\ \Delta\theta_{13},\ \Delta\theta_{14})$ are given by $(0.5, 0., 0.5)$, $(0.5, 0.5, 0.)$, and $(0., 0.5, 0.5)$. Cell 1 could fire in phase with either of cells 2, 3 or 4, while the remaining two cells fire in anti-phase relationship with cell 1 (and synchronously with each other). This is also shown in the clustering results for the 3D phase torus in Table 4.1. For any given parametric block of Fig. 4.3, each color indicates the existence of a stable rhythm, along with all of its isomorphisms. Multiple colors within the same block indicate the co-existence of different stable rhythmic patterns in the phase space. The sizes of the colored regions proportionately relate to the sizes of the attraction basins of those rhythms, given by the percentage of trajectories converging to those rhythms (PC). Noise within the colored region representing a cluster is proportional to the cluster's circular standard deviation (CCSD) and is indicative of the variability within the cluster. The clustering analysis for the network across different $g_{inh}$ vs. $I_{app}$ blocks at $\varepsilon = 0.5$ in Fig. 4.3 shows that the network can exhibit a plethora of different stable rhythms, pictured in Fig. 4.4. Clustering details with CCM, CCSD and PC at some of these parametric blocks are presented in Table. 4.2. Mixed traveling-waves are seen at a different $\varepsilon = 0.05$ (see supplementary Fig.4.8).

### 4.3.1 Paired half-centers

This is the most dominant rhythm of the fully connected network as seen from the bifurcation diagram of Fig. 4.3 (orange regions such as $A$) at $\varepsilon = 0.5$, as well as at $\varepsilon = 0.3$ shown in the bifurcation diagram of supplementary Fig. 4.7. These 2-phasic rhythms are characterized by two pairs of cells that oscillate in anti-phase relationship with each other, while the cells within each pair oscillate in-phase. By virtue of symmetry of the fully connected network, there exist 3 stable isomorphisms of this rhythm. The phase-lag ordered tuple for one such rhythm is given by $(\Delta\theta_{12},\ \Delta\theta_{13},\Delta\theta_{14}) = (0., 0.5, 0.5)$ and is shown in Fig. 4.4, while the corresponding limit cycle orbit of the voltage and the recovery variables is represented in Fig. 4.5 (orange). Note here that the voltage amplitude of the orbit for the paired half-center rhythm is slightly smaller than that of an isolated cell (grey), due to the continuous inhibition experienced by a cell in its active state from its phase locked counterpart.

### 4.3.2 Synchronized state

Surprisingly, we see that the fully connected network of neurons reciprocally coupled with fast-inhibition can also exhibit stable synchronization of neuronal activity with $(\Delta\theta_{12}$ , $\Delta\theta_{13},\ \Delta\theta_{14}) = (0., 0., 0.)$, for particular values of the parameters: $I_{app} = 0.435$ and for $0.013 \leq g_{inh} \leq 0.025$ (see green regions in Fig. 4.3). The synchronized state coexists with the 3 paired half-center rhythms at these parameter values. The corresponding orbit for the voltage and recovery variables is shown in Fig.4.5 (green). The voltage amplitude of this orbit is even shorter than those of either the isolated cell (grey) or the paired half-center rhythm (orange), due to the greater inhibitory push experienced by a neuron in its active state from the 3 other phase locked counterparts. With increasing $g_{inh}$ in Fig. 4.3, the size of the attractor for the synchronized state gradually increases through $g_{inh} = 0.025$ (Fig. 4.3B), beyond which it loses stability and gives rise to a chimera state at $g_{inh} = 0.029$ (Fig. 4.3C). Note that the stable synchronized state is seen in the network only at $\varepsilon = 0.5$ (Fig. 4.3) but not at either $\varepsilon = 0.3$ (supplementary Fig. 4.7) or $\varepsilon = 0.05$ (sup-

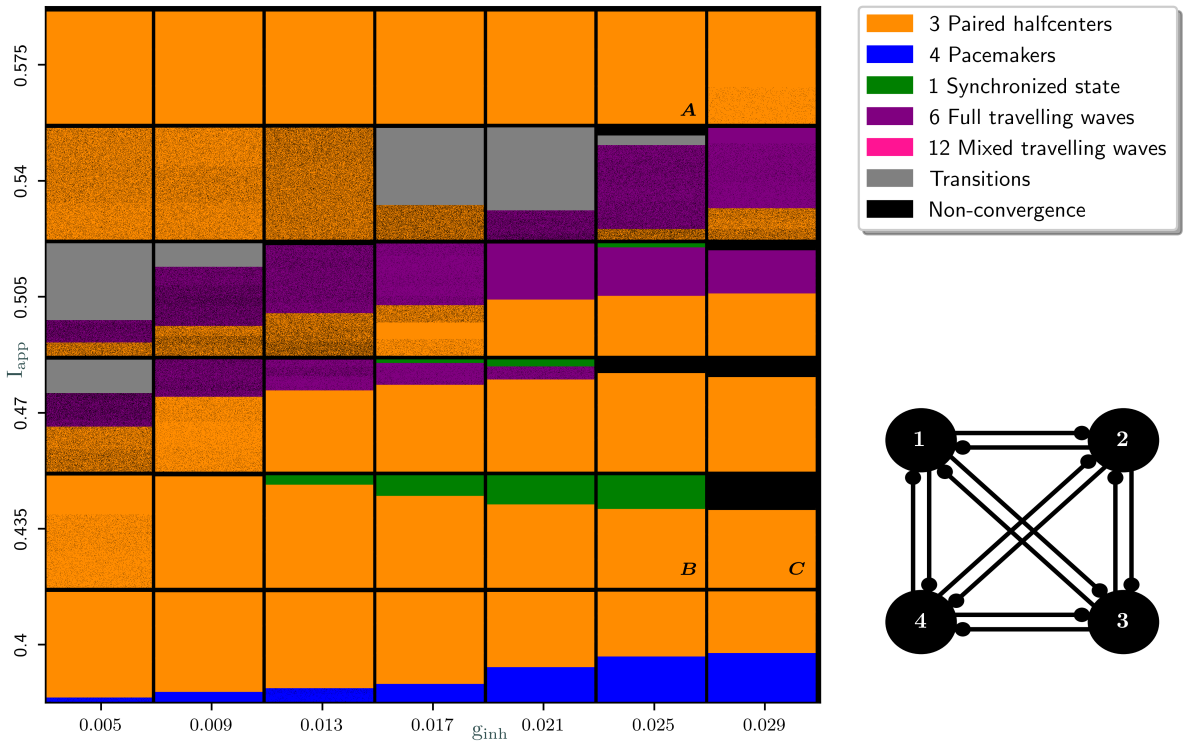


**Figure (4.3)** Multistability and bifurcation analysis of the fully connected 4-cell circuit with varying synaptic strength ($g_{inh}$) and external drive ($I_{app}$) on a $7 \times 6$ grid, at $\varepsilon = 0.5$. Each block in the grid depicts the clusters and the stable rhythms identified for the particular parameter values, shown in different colors in proportion to the size of their attraction basins in the phase space. Noise within a cluster is proportional to its circular standard deviation. Clustering results for some of these parametric blocks are shown Table 4.1,4.2. The bifurcation diagram identifies the rich repertoire of stable rhythms and all their isomorphisms expected from the symmetry of the circuit, including paired half-centers, pacemakers, traveling-waves, synchronization, stable transitory rhythms, and trajectories with non-converging phase lags (chimeras), as pictured in Fig. 4.4.

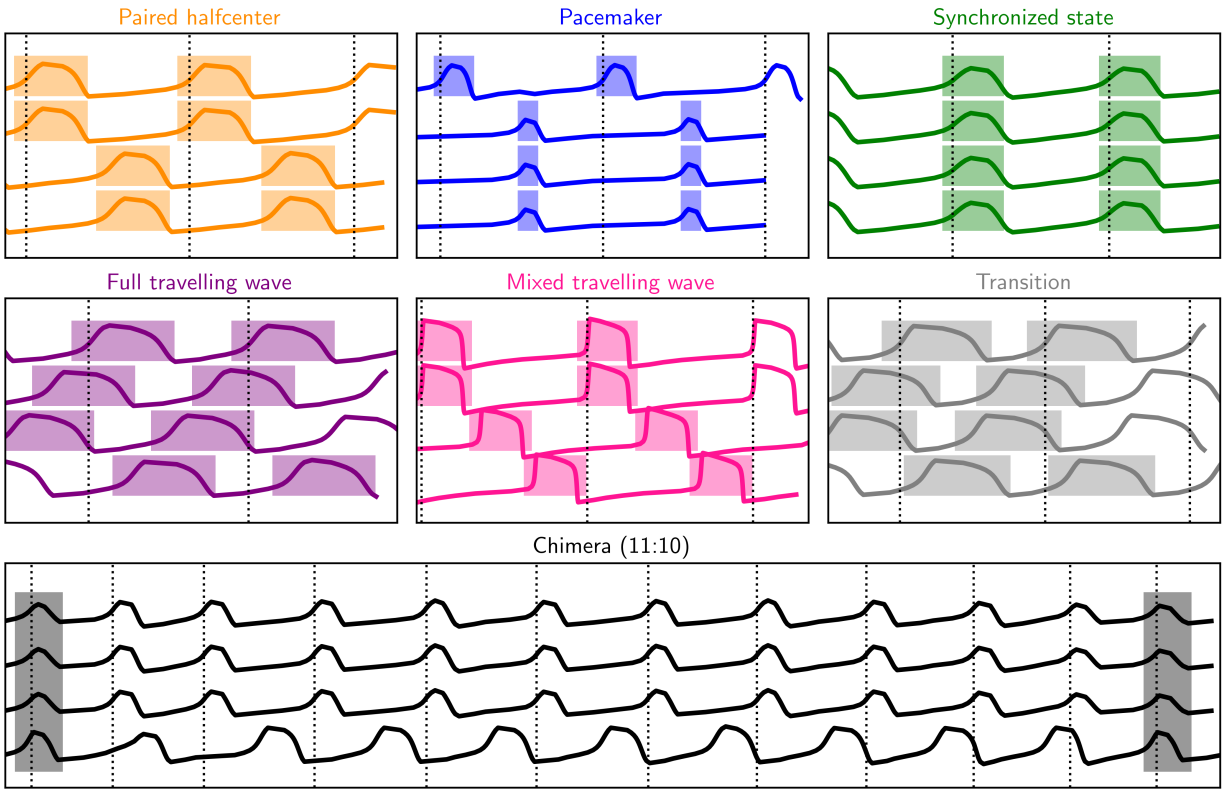


**Figure (4.4)** Rhythmic capacity of the fully connected 4-cell circuit (Fig. 4.2d), depending on the parameter values (see Fig. 4.3), includes 3 paired half-centers, 4 pacemakers, a single fully synchronous state, 6 full traveling-waves, 12 mixed traveling-waves, stable transitory rhythms between paired half-centers and full traveling-waves, and 4 chimera states featuring a 11:10 resonance.

plementary Fig. 4.8). We also note that, as $I_{app} = 0.435$ and $g_{inh} = 0.025$ are kept constant (see Fig. 4.3B) while $\varepsilon$ is gradually reduced from $0.5$ to $0.48$, the corresponding synchronized orbit undergoes period doubling such that all the four cells yet continue to maintain phase synchrony, while splitting into two pairs that continuously alternate between orbits of slightly shorter and longer amplitudes.

### 4.3.3 Chimera states

Further increase of $g_{inh}$ through $0.029$ at $I_{app} = 0.435$ (see Fig. 4.3C) shows a non-converging state (black regions) from the clustering analysis of Poincaré maps. Detailed inspection reveals the presence of chimera states characterized by two sub-populations

firing at distinct frequencies. Three of the cells continuously fire in phase, while the fourth cell experiences phase slipping and synchronizes with the other three once every 10 cycles, when those cells complete 11 cycles, thereby resulting in a chimera with a 11:10 resonance as shown in Fig. 4.4. Note the shorter voltage amplitude of the three cells firing in sync compared to the cell undergoing phase slipping, for reasons described previously. By virtue of the symmetry of the network, there exist four isomorphisms of this rhythm, with any one of the four cells undergoing phase slipping while the other three fire in phase. Further increase of $g_{inh}$ to $0.033$ (not shown in Fig. 4.3) results in the chimera states morphing into pacemaker rhythms. Thus, the chimera state serves as a transition mechanism between the synchronized state and the pacemaker patterns. At other values of the parameters, we also observe chimera states with different resonances, including 7:8 resonance at $\varepsilon = 0.55$ and 14:16 resonance at $\varepsilon = 0.56$ for $g_{inh} = 0.025$ and $I_{app} = 0.435$. For larger values of $g_{inh} > 0.03$, several other chimera like states become prominent as cells in the active state, through strong inhibition, quickly inactivate or shutdown the post synaptic cells.

### 4.3.4 Pacemakers

At small values of external drive $I_{app} = 0.4$, the fully connected network can exhibit 2-phasic pacemaker rhythms co-existing with the paired half-center rhythms (Fig. 4.3, supplementary Fig. 4.7). These rhythms are characterized by one cell driving the rhythm and firing in anti-phase with three other cells that oscillate in-phase. Four stable isomorphisms exist for this rhythm, with each of the four cells capable of driving such a pacemaker pattern. The phase lag ordered tuple for one such rhythm is given by $(\Delta\theta_{12}$ , $\Delta\theta_{13}$, $\Delta\theta_{14}) = (0.5, 0.5, 0.5)$ and is shown in Fig. 4.4, which also reveals the shorter voltage amplitudes of the three driven cells in comparison to that of the driving pacemaker cell.

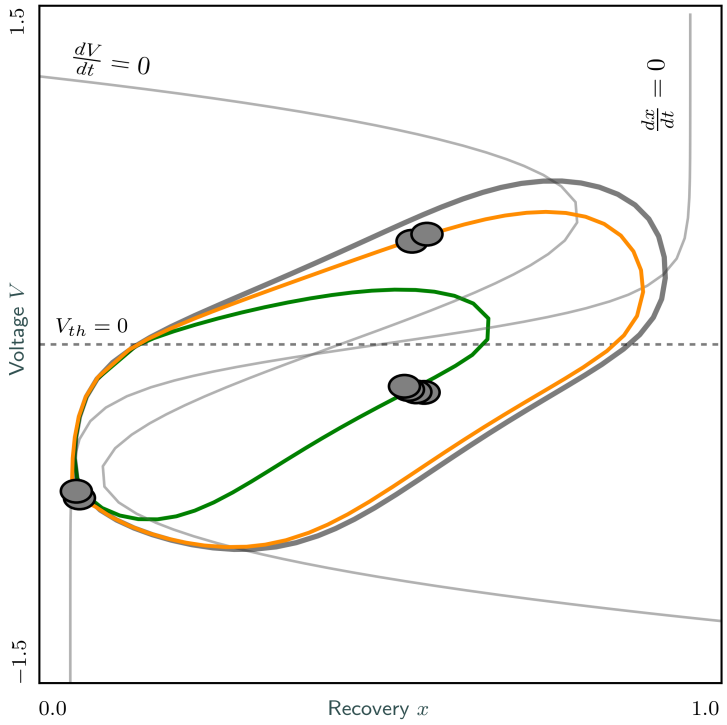


**Figure (4.5)** Voltage-recovery phase space shows how the limit cycle of an isolated neuron (grey) changes its shape in a fully connected 4-cell circuit based on its initial conditions, to produce either a paired half-center rhythm (orange) or the synchronized state (green) (Fig. 4.3B). The size of the orbit for the paired half-center (orange) is smaller than that of an isolated cell (grey) due to the continuous inhibition from their phase locked counterparts affecting the cells in their active state (and shortening the corresponding section of the limit cycle). For the synchronized state, the orbit becomes even smaller (green) due to the greater consolidated inhibition on a postsynaptic cell by the 3 other cells in sync.

### 4.3.5 Traveling-waves

The network can produce 6 isomorphisms of a full 4-phasic traveling-wave rhythm, where the cells fire sequentially one after the other in a cyclic fashion (see Fig. 4.3, supplementary Fig. 4.7, supplementary Fig. 4.8). The phase-lag ordered tuple for one such rhythm is given by $(\Delta\theta_{12}\ ,\ \Delta\theta_{13},\ \Delta\theta_{14}) = (0.25, 05., 0.75)$, while the corresponding voltage trace is depicted in Fig. 4.4. We observe that at $\varepsilon = 0.05$ (supplementary Fig. 4.8), the network can also exhibit a different type of traveling-wave rhythm that is referred to as a *mixed* 3-phasic traveling-wave, where two cells fire in phase while oscillating sequentially with the other two cells. The network can produce a total of 12 isomorphisms of

**Table (4.2)** Details of the clustering analysis for multistability of the fully connected network at three representative parametric blocks of Fig. 4.3 at $g_{inh} = 0.025$ and $\varepsilon = 0.5$.

| $I_{app}$ | CCM | CCSD | PC |
|---|---|---|---|
| 0.4 | (0.5, 0., 0.5) | (0., 0., 0.) | 18.9% |
| | (0.5, 0., 0.) | (0., 0., 0.) | 8.9% |
| | (0.5, 0.5, 0.5) | (0., 0., 0.) | 15.8% |
| | (0.5, 0.5, 0.) | (0., 0., 0.) | 18.8% |
| | (0., 0., 0.5) | (0., 0., 0.) | 8.9% |
| | (0., 0.5, 0.5) | (0., 0., 0.) | 18.9% |
| | (0., 0.5, 0.) | (0., 0., 0.) | 9.3% |
| 0.435 | (0., 0., 0.) | (0., 0., 0.) | 28.5% |
| | (0., 0.5, 0.5) | (0., 0., 0.) | 23.9% |
| | (0.5, 0., 0.5) | (0., 0., 0.) | 23.8% |
| | (0.5, 0.5, 0.) | (0., 0., 0.) | 23.8% |
| 0.54 | (0.5, 0.25, 0.74) | (-0., 0.02, 0.02) | 12.7% |
| | ( 0.74, 0.25, 0.5 ) | ( 0.03, 0.03, -0. ) | 12.6% |
| | ( 0.25, 0.5, 0.74) | ( 0.03, -0., 0.03) | 12.4% |
| | ( 0.25, 0.74, 0.5 ) | ( 0.03, 0.03, -0. ) | 12.9% |
| | ( 0.74, 0.5, 0.25) | ( 0.02, -0., 0.02) | 12.8% |
| | ( 0.5, 0.74, 0.25) | (-0., 0.03, 0.03) | 12.7% |
| | ( 0.49, 0.98, 0.49) | (0.03, 0.04, 0.04) | 4.3% |
| | ( 0.95, 0.47, 0.48) | ( 0.03, 0.03, 0.03) | 2.6% |
| | (0.05, 0.52, 0.53) | ( 0.03, 0.03, 0.04) | 3.1% |
| | ( 0.48, 0.47, 0.95) | ( 0.03, 0.04, 0.03) | 1.5% |
| | ( 0.53, 0.53, 0.05) | ( 0.04, 0.04, 0.04) | 6% |

such mixed traveling-wave rhythms; one is shown in Fig. 4.4 with the phase lags locked at $(\Delta\theta_{12}\ ,\ \Delta\theta_{13},\ \Delta\theta_{14}) = (0., 0.67, 0.33)$.

### 4.3.6 Stable transitions

Figure 4.4 shows a stable "transitory" rhythm given by $(\Delta\theta_{12}\ ,\ \Delta\theta_{13},\ \Delta\theta_{14}) = (0.41, 0.5, 0.91)$ at $g_{inh} = 0.025$ and $I_{app} = 0.552$. Such rhythms serve as stable intermediate states between some of the rhythms previously described. As we move downward from Fig. 4.3A where there are just 3 paired half-center rhythms at $I_{app} = 0.575$, the system gives rise to 6 full traveling-wave rhythms at $I_{app} = 0.505$, in addition to the 3 paired

half-centers. Between these values of $I_{app}$, the full traveling-waves lose stability via a supercritical pitch fork bifurcation and give rise to two such stable transitory rhythms (grey). For example, when the full traveling-wave given by $(\Delta\theta_{12}\ ,\ \Delta\theta_{13},\ \Delta\theta_{14}) = (0.25, 0.5, 0.75)$ loses stability, the anti-phase relationships $\Delta\theta_{13} = 0.5$ and $\Delta\theta_{24} = 0.5$ are maintained, but the active phase of cell $1$ could get closer and closer to that of either of cell $2$ or $4$, while the phases of the remaining two cells also start getting closer and closer, until they give rise to either of the paired half-centers given by $(0., 0.5, 0.5)$ (1,2 vs. 3,4) or $(0.5, 0.5, 0.)$ (1,4 vs. 2,3). Therefore, for intermediate values of $I_{app}$, we could gradually see stable transitory rhythm pairs such as $(0.15, 0.5, 0.65)$, $(0.35, 0.5, 0.85)$, and $(0.05, 0.5, 0.55)$, $(0.45, 0.5, 0.95)$.

### 4.4 Robust monostable/bistable network topologies

Multistability and bifurcation analysis for the other 4-cell network topologies of Fig. 4.2 (see supplementary Fig.4.9,4.10,4.11) shows that the two-way inhibitory loop (Fig. 4.2b) and mixed (Fig. 4.2c) networks exhibit robustly monostable rhythms (their $g_{inh}$ vs. $I_{app}$ parametric sweeps show a single stable rhythm across all parametric blocks) given by the phase lag ordered tuples $(0.5, 0., 0.5)$ (paired half-center) and $(0.25, 0.5, 0.75)$ (full traveling-wave), respectively, while the one-way inhibitory loop network (Fig. 4.2a) exhibits robust bistability with both these rhythms $(0.5, 0., 0.5)$ and $(0.25, 0.5, 0.75)$, as the parameters $g_{inh}$, $I_{app}$, and $\varepsilon$ are varied. Note that no other stable isomorphisms of these full traveling-wave and paired half-center rhythms are stable in these network configurations due to the missing connections from the fully connected circuit (Fig. 4.2a). Compare the full traveling-wave rhythm of the mixed network (Fig. 4.2c) with a similar reduced swim CPG found in the sea slug *Melibe leonina* (with additional excitatory connections) [31, 65] (see Fig. 3.3 from Ref. [65]). Neurophysiological experiments with this CPG reported the occurrence of a similar full traveling-wave pattern in the voltage traces.

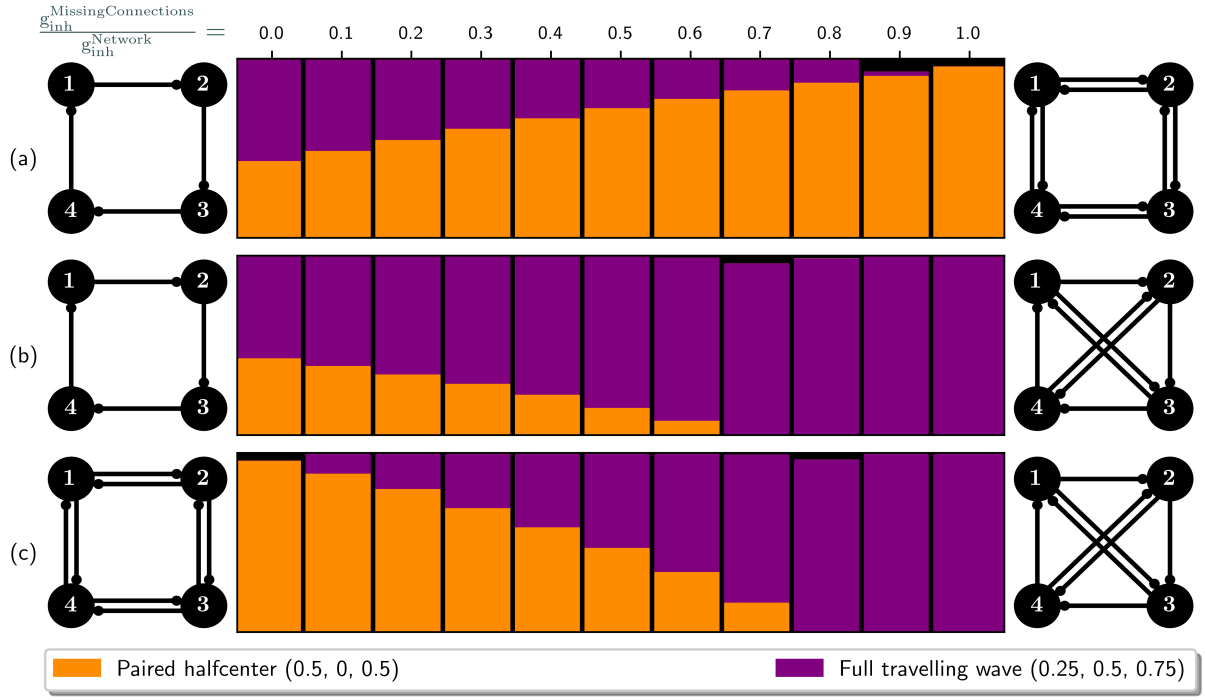


**Figure (4.6)** Structural changes in a network promote or suppress rhythmic behaviors. Gradual strengthening or weakening of the synapses converts the circuits on the left into the circuits on the right. Purple regions represent the 4-phasic full traveling-wave rhythm of $(0.25, 0.5, 0.75)$ while orange regions represent the 2-phasic paired half-center $(0.5, 0., 0.5)$, with sizes proportional to their attractors in the phase space. One-way inhibitory loop network exhibits robust bistability with both these rhythms while two-way inhibitory loop and mixed networks show robust mono-stability with the paired half-center and the traveling-wave pattern, respectively. (a) Transition from bistability to monostable paired half-center rhythm while the traveling-wave rhythm is gradually suppressed. (b) Bistable network transitions to monostable traveling-wave rhythm. (c) Transitions from one monostable rhythm (paired half-center) to another (full traveling-wave). At intermediate synaptic changes when not all synapses between the neurons have equal strengths, the network is bistable. Here, $g_{inh}^{Network} = 0.029$, $I_{app} = 0.54$ and $\varepsilon = 0.3$

## 4.5 Network transitions/rewiring

Our approach can generate verifiable hypotheses for experimental manipulations and rewiring of real animal CPGs with dynamic clamping experiments [199]. We can investigate how network topologies and synaptic changes can alter the rhythmic behavior of the network and promote or suppress multistability. Fig. 4.6 shows the functional changes in CPG rhythms and their mono/multi-stable behaviors due to structural changes in network topology. The network on the left is gradually transitioned into the network on the right by synaptic changes, while the rhythmic behaviors and multistability are analyzed during these transitions. Purple regions represent the full traveling-wave rhythm $(0.25, 0.5, 0.75)$ while orange regions represent the paired half-center $(0.5, 0., 0.5)$, with sizes proportional to their attractors in the phase space. Gradual strengthening of the anti-clockwise inhibitory connections in Fig. 4.6a converts the bistable one-way inhibitory loop network into the monostable two-way inhibitory loop network. The paired half-center rhythm is promoted while the traveling-wave rhythm is suppressed. In Fig. 4.6b, mutual inhibitions between cells 1,3 and cells 2,4 are gradually strengthened to convert the bistable one-way inhibitory loop network on the left to the monostable mixed network on the right. The traveling-wave rhythm is gradually promoted while the paired half-center rhythm is suppressed. In Fig. 4.6c, by gradually weakening the anti-clockwise inhibitory loop and simultaneously strengthening mutual inhibitions between cells 1,3 and cells 2,4, the network transitions from one monostable rhythm (paired half-center) to another (full traveling-wave). At intermediate synaptic changes, the network is bistable. Also, note that at such intermediate stages, the synaptic strengths in the network are not all identical, but the homogeneity of the neurons in the network is maintained, with all of them receiving similar total synaptic inputs.

## 4.6 Summary and future directions

In summary, we combine the existing techniques of dynamical systems theory with modern computational approaches such as unsupervised machine learning (clustering) algorithms and faster GPU-parallelized simulations of heavily populated trajectories to reveal the rhythmic capacities of homogenous 4-cell networks. This chapter extends our knowledge of the basic principles guiding multi-stable rhythmic behaviors in such neural networks and shows that mono/multistability of a CPG depends on the complex interaction of several intrinsic and extrinsic factors including network topology, slow-fast dynamics, synaptic strength, and external current drive. Such factors alter the positions and shapes of the fast $V$-nullcline and the slow $x$-nullcline, as well as the gap between them, to control the release and escape mechanisms of a bursting neuron [68]. We identify network topologies that exhibit robust monostable rhythms (Fig. 4.2b,c) or robust bistability (Fig. 4.2a) for a range of parameter values and are resilient to external perturbations, while other network configurations (Fig. 4.2d) display a rich array of multistable behaviors that intricately depend upon the internal and external parameters. We demonstrate how the fully connected 4-cell network can exhibit a plethora of multistable rhythmic states composed of pacemakers, paired half-centers, full and mixed traveling-waves, synchronized states, and chimeras. Symmetry of the network implies the coexistence of several stable isomorphic rhythms. We note that the paired half-center rhythms, where half the cells are firing at any point of time in anti-phase with the remaining half, are prominent in the fully connected network at faster $\varepsilon = 0.5$ (Fig.4.3 orange regions), while various traveling wave rhythms (full and mixed) become prominent for slower $\varepsilon = 0.05$ (supplementary Fig.4.8 pink and purple regions).

We identify the transitions and bifurcations that occur with changing network topologies and other parameters to identify factors promoting or suppressing monostable/multistable rhythmic output, allowing us to predict the changes in patterns of activity and multistability. Such synaptic modifications and rewiring (as shown in Fig. 4.6) on real animal

CPGs can be performed using dynamic clamping technique, and our analysis can serve as a precursor to determine the most relevant hypotheses to test in such experiments, in order to identify the significance of various connections of the circuit in producing robust rhythmic behaviors. For example, the reduced swim CPG of the sea slug Melibe leonina [31,65] closely resembles the mixed network (Fig. 4.2c) (with additional excitatory connections), and produces a robust full traveling wave rhythm. Our analysis shows that rewiring of this mixed network can lead to bistability (Fig. 4.6b) or a monostable paired half-center rhythm (Fig. 4.6c). Such analyses can, therefore, be performed with models tuned to the particular animal CPGs of interest and the most relevant hypotheses identified can then be tested in neurophysiological experiments.

Our analysis can help non-biological systems from engineering, economics, and environmental studies, where loss of resilience is a challenge to predict and can cause catastrophic effects. Such understanding is also essential to study motor control, dynamic memory, information processing, and decision making in animals and humans [200]. It also has implications for gaining insights into complex neurological phenomena in higher animals along with neurological disorders related to CPG arrhythmia, and the development of mechanisms to treat such disorders. Before such techniques can be applied to humans, we need to achieve a comprehensive understanding of the working of these modular networks in lower animals and through computational models. While this project deals with networks of single neurons, the methodology might also be applied to study networks of brain regions or neural populations that synergistically excite or inhibit each other and produce rhythmic patterns of firing [201,202]. The insights in CPG multistability gained from this research might help in the design and development of more efficient robot locomotion [203–214]. An important aspect of these analytical and computational techniques is their validity across a wide range of oscillatory networks without dependence on the underlying mathematical equations. Hence they are applicable to a variety of rhythmic neuronal and non-neuronal activities beyond motor control and will benefit a wide audience of interdisciplinary researchers for studies of diverse nonlinear applications.

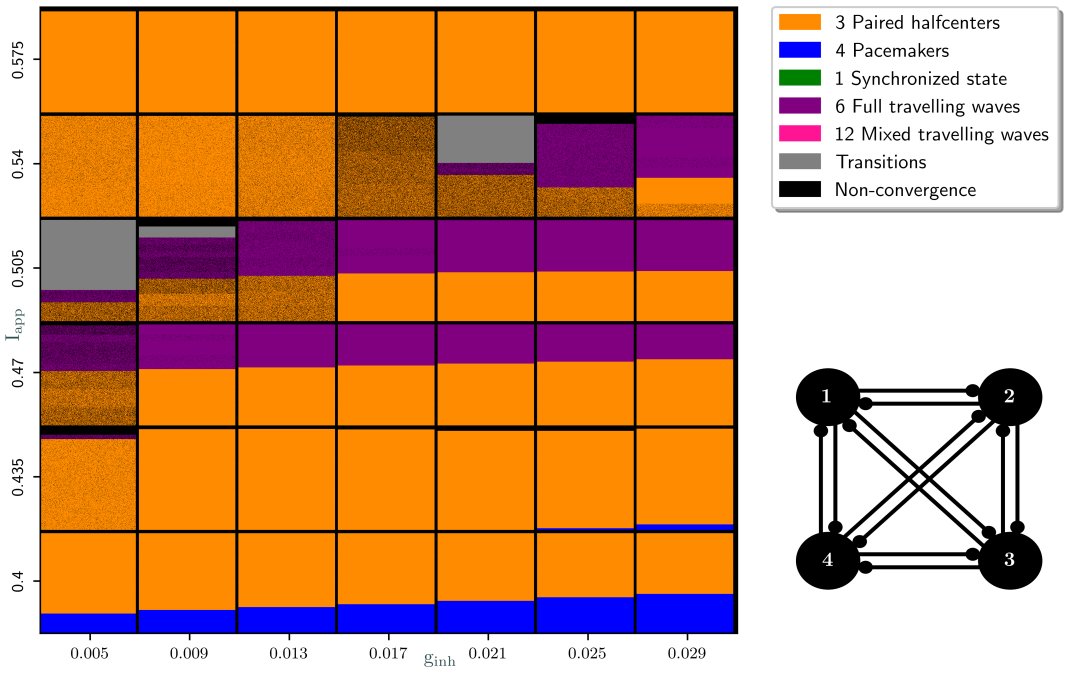


**Figure (4.7)** Multistability and bifurcation analysis of the fully connected 4-cell network at $\varepsilon = 0.3$ shows similar rhythmic capacity as Fig.4.3 (at $\varepsilon = 0.5$), except for the lack of stable synchronized state.

## Supplementary Material

Supplementary figures are presented below.

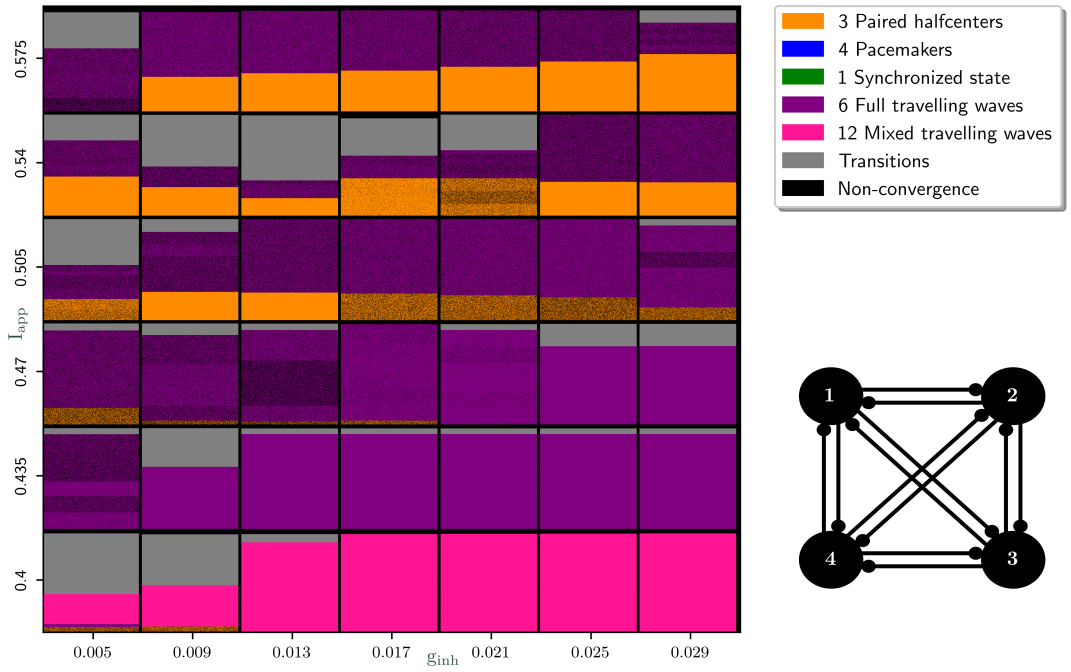


**Figure (4.8)** Multistability and bifurcation analysis of the fully connected 4-cell circuit at $\varepsilon = 0.05$ shows the dominant expression of the traveling-wave (full and mixed) rhythms, compared to the paired half-centers.

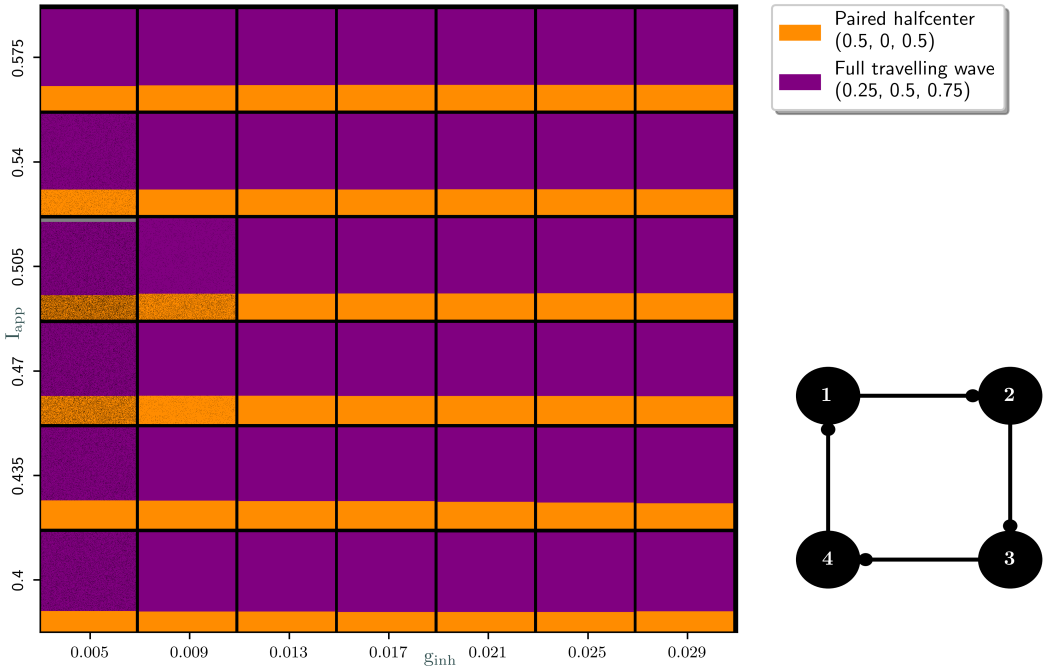


**Figure (4.9)** Robust bistability of the one-way inhibitory loop network with the full travelling wave rhythm of $(0.25, 0.5, 0.75)$ and the paired half-center $(0.5, 0., 0.5)$. No other stable isomorphisms of these rhythms exist due to the missing synaptic connections compared to the fully connected network. $\varepsilon = 0.5$.

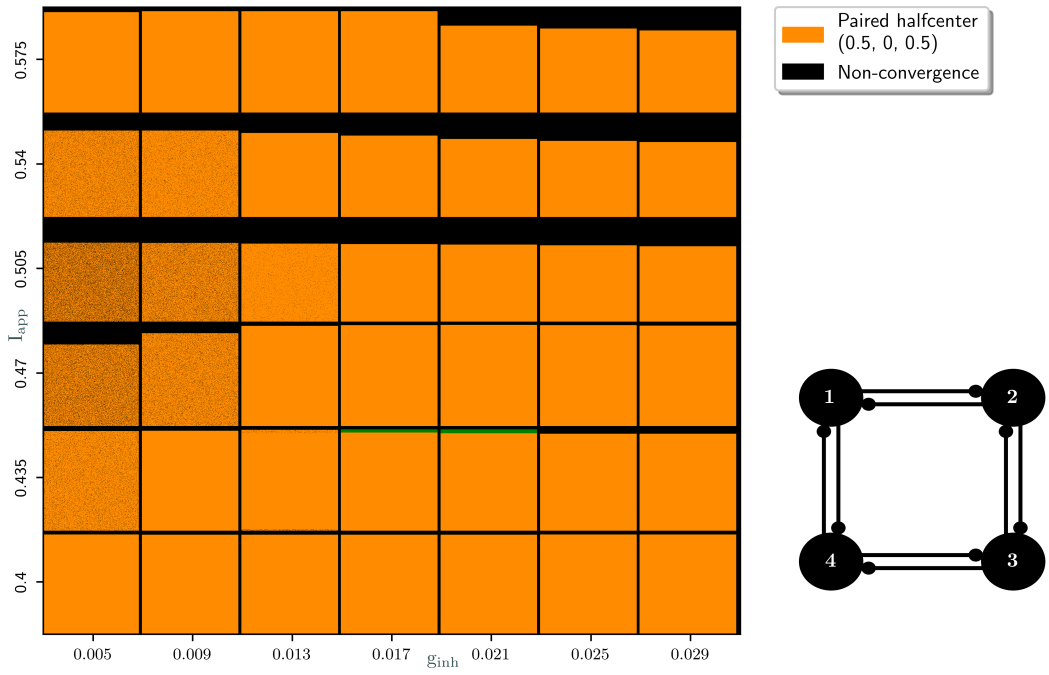


**Figure (4.10)** Robust monostability of the two-way inhibitory loop network with the paired half-center rhythm $(0.5, 0., 0.5)$ (no other stable isomorphisms). $\varepsilon = 0.5$.

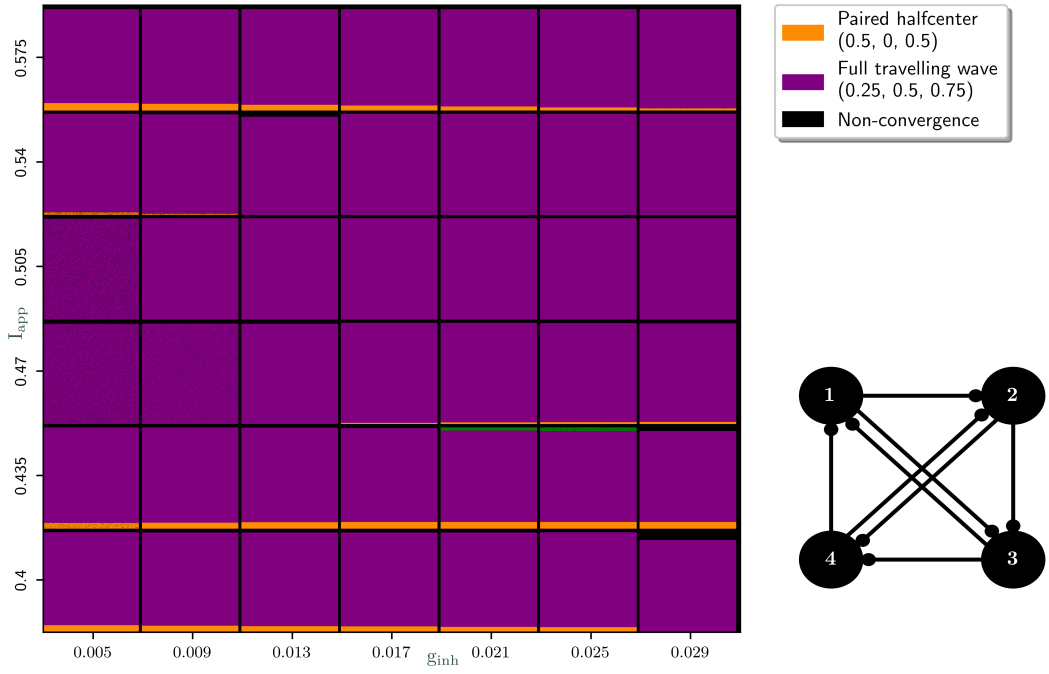


**Figure (4.11)** Robust monostability of the mixed network with the full travelling wave rhythm of $(0.25, 0.5, 0.75)$ (no other stable isomorphisms). $\varepsilon = 0.5$.

# CHAPTER 5

## APPLICATIONS BEYOND NEUROSCIENCE: CHAOTIC NONLINEAR SYSTEMS

Although the main focus of this thesis is to understand the behaviors of biological neural network dynamics, the methods and approaches we developed have broad applications for the study of cross-disciplinary nonlinear phenomena at large. The technique Deterministic Chaos Prospector (DCP) reduces phase space dynamics to symbolic representations, allowing us to detect regions of simple and complex dynamics, and to elaborate on the onset mechanisms of deterministic chaos due to complex homoclinic bifurcations in diverse systems with a Lorenz-like chaotic attractor. Massively parallel simulations can shorten the computational time to disclose highly detailed bifurcation diagrams to just a few seconds. In this chapter, we demonstrate this for a nonlinear laser model and discuss the multiplicity and self-similarity of homoclinic and heteroclinic bifurcation structures in its 2D and 3D parameter spaces. We show detailed computational reconstructions of key bifurcation structures such as Bykov T-point spirals and inclination flips in 2D parameter space, as well as the spatial organization and 3D embedding of bifurcation surfaces, parametric saddles, and isolated closed curves (isolas). This chapter is edited with permission based on the publications and further details can be found in [4,183]. The application of these techniques for the global organization of bi-parametric structures that underlie the emergence of chaos in a simplified resonantly coupled wave triplet system can be found in [3]. The knowledge and the methodology created in these studies would further advance new ideas and approaches for nonlinear science, while the generality of our modeling approaches makes them applicable to other biological, medical, and engineering systems [89].

## 5.1 Background

*New directions in science are launched by new tools much more often than by new concepts.* Dyson F. [215]. Break-through discovery of deterministic chaos in [infra-red gas] lasers in nonlinear optics was established and pioneered both theoretically and experimentally long time ago [216–220]. Recent developments in semiconductor lasers and nano-optics have stimulated newest advances in optical synchronization and photonic integrated circuits for the needs of cryptography [221–226]. Nowadays, a real advance in deterministic nonlinear science stimulating the progress of cutting-edge engineering is hardly possible without significantly deepening the knowledge and beneficial usage of complex elements borrowed from dynamical systems theory. This in turn is hardly possible without development and incorporation of new mathematical and computational tools, including for parallel Graphics Processing Unit(GPU) based platforms.

In this chapter, we demonstrate how our newly developed toolkit, called "Deterministic Chaos Prospector (DCP)," lets us disclose and elaborate on the origin of complex chaotic dynamics in a 6D model of a resonant 3-level optically-pumped laser (OPL) [227, 228]. In addition to simple dynamics associated with stable equilibria and periodic orbits, it reveals a broad range of bifurcation structures that are typical for many ODE models from nonlinear optics and other diverse applications [229–233]. These include homoclinic orbits and heteroclinic connections between saddle equilibria that are the key building blocks of deterministic chaos in most systems. Their bifurcation curves with characteristic spirals around T(terminal)-points along with other codimension-2 points are the organizing centers that shape regions of complex and simple dynamics in the parameter space of such systems. The detection of these bifurcations has long remained the state-of-the-art involving a meticulous and time consuming parameter continuation technique to disclose a few sparse elements of the otherwise rich and fine organization of the bifurcation set. We note that while the brute-force approach based on the evaluation of Lyapunov exponents can effectively locate stability windows within regions of chaos [234, 235], it fails to

disclose these essential structures that are imperative for the exhaustive understanding of complex dynamics and their origin. We will demonstrate how our approach exploiting the sensitivity of deterministic chaos and its symbolic representation using binary sequences combined with Lempel-Ziv complexity algorithms [236], can effectively reveal regions of complex, structurally unstable and simple stable dynamics in this and other systems.

## 5.2 3-level optically pumped laser model

The 3-level optically pumped laser model [227, 228] is given by

$$\begin{aligned}
\dot{\beta} &= -\sigma\beta + 50p_{23}, \\
\dot{p}_{21} &= -p_{21} - \beta p_{31} + aD_{21}, \\
\dot{p}_{23} &= -p_{23} + \beta D_{23} - ap_{31}, \\
\dot{p}_{31} &= -p_{31} + \beta p_{21} + ap_{23}, \\
\dot{D}_{21} &= -b(D_{21} - D_{21}^0) - 4ap_{21} - 2\beta p_{23}, \\
\dot{D}_{23} &= -b(D_{23} - D_{23}^0) - 2ap_{21} - 4\beta p_{23},
\end{aligned} \tag{5.1}$$

with variable $\beta$ and parameter $a$, being the Rabi flopping quantities representing the electric field amplitudes at emission and pump frequencies, resp.; $\sigma = \{1.2;\ 1.5;\ 10\}$ is the cavity loss parameter; $b$ is the ratio of population to polarization decay rates; $p_{ij}$ is the normalized density matrix element corresponding to the transitions between levels $i$ and $j$, while $D_{ij}$ is the population difference between the $i$-th and $j$-th levels. Note that this system is $\mathbb{Z}_2$-symmetric under the involution $(\beta, p_{21}, p_{23}, p_{31}, D_{21}, D_{23}) \leftrightarrow (-\beta, p_{21}, -p_{23}, -p_{31}, D_{21}, D_{23})$, which is typical for Lorenz-like systems [231, 237]. Depending on $(a, b)$-values, the laser model has either a single non-lasing steady state, $O$, or an extra pair of equilibria, $C^{\pm}$ (Fig. 5.1a), emerging as $O$ loses stability through a pitch-fork ($PF$) bifurcation and becomes a saddle. All three steady states can independently undergo super-

critical Andronov-Hopf ($AH$) bifurcations (curves labelled with $AH_0$ and $AH_{1,2}$ in the $(a,\ b)$-parameter plane in Fig.5.2) giving rise to stable periodic orbits (PO) in the phase space of the laser model.

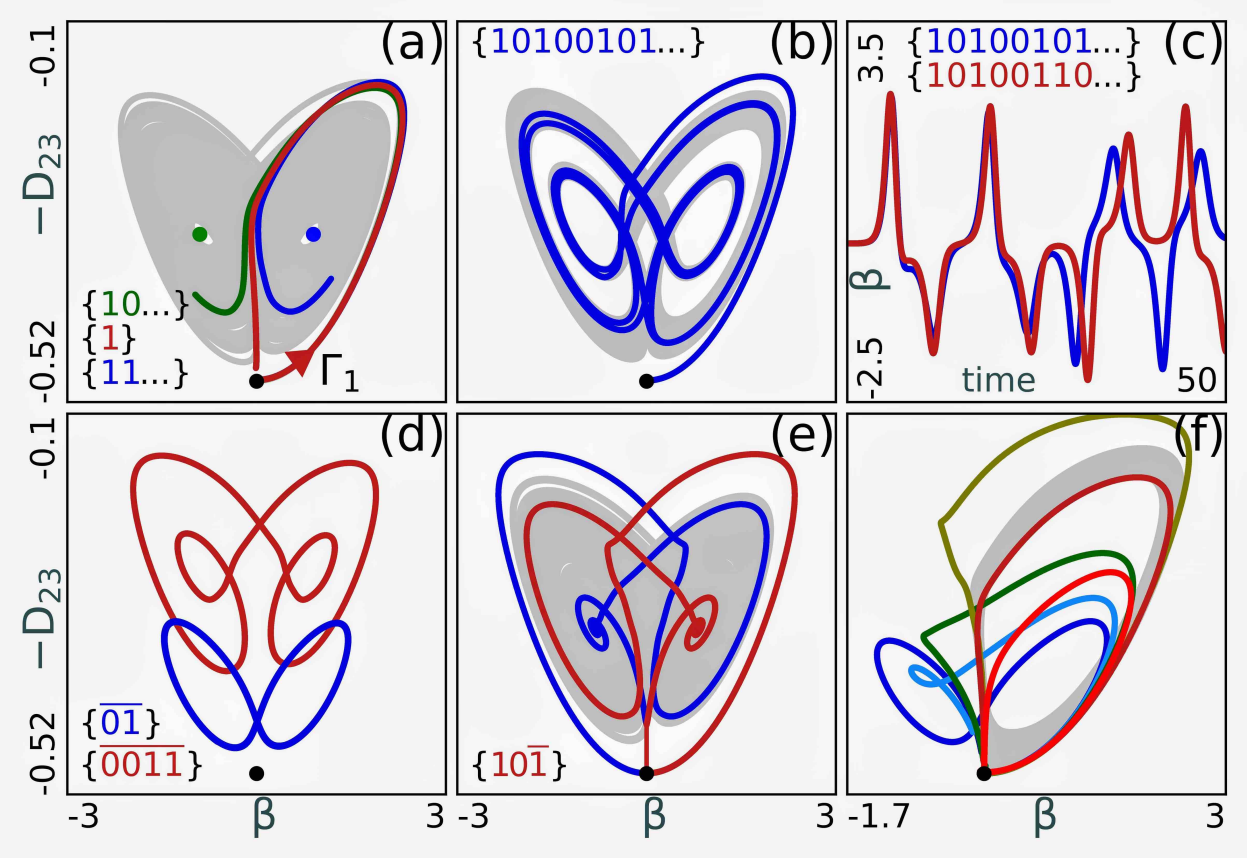


**Figure (5.1)** (color online) (a) $(\beta, -D_{23})$-phase space projection showing the primary homoclinic orbit (red, coded as $\{1\}$) splitting leftward/rightward (green/blue, $\{11...\}$ or $\{11...\}$) when the separatrix $\Gamma_1$ misses the saddle $O$ (black dot) after completing a single turn around the saddle-focus $C^+$, with the Lorenz attractor (in grey) in background (b) Chaotic transient of $\Gamma_1$ generating a binary sequence starting with $\{10100101...\}$ (c) Time-evolutions of the $\beta$-coordinate of $\Gamma_1$ (in (b)) and of a close trajectory (red), and their binary codes, before they diverge. (d) Two stable symmetric POs coded as $\{\overline{01}\}$ and $\{\overline{0011}\}$ (e) Heteroclinic connections (red $\{10\overline{1}\}$, blue symmetric counterpart) at the $T_1$-point (Fig. 5.2) (f) Samples ($P_j$) of the primary homoclinic orbit morphing to a double loop after the inclination-flip, $IF_1$, on the curve $H_0$ in the $(a, b)$-parameter plane in Fig.5.2; here $\sigma = 1.5$

### 5.3 Symbolic encoding and parametric sweeps

Both structural and dynamical instability in the model are due to an abundance of homoclinic bifurcations ($HB$) of the saddle $O$, whose 1D unstable separatrix $\Gamma_1$ (and the symmetric counterpart $\Gamma_2$) densely fills out the two spatially-symmetric wings of the butterfly-shaped strange attractor (Fig. 5.1a,e) [237]. As parameters are varied $\Gamma_1$ constantly and unpredictably changes its flip-flop switching patterns within the Lorenz attractor. These patterns change whenever $\Gamma_1$ comes back to $O$ to undergo a homoclinic bifurcation. This observation is the core for the proposed symbolic approach that converts chaotic and periodic patterns of $\Gamma_1$ around the equilibria $C^{\pm}$ into binary sequences $\{k_n\}$ as follows:

$$k_n = \begin{cases} 1, & \text{when the separatrix } \Gamma_1 \text{ turns around } C^{+}; \\ 0, & \text{when the separatrix } \Gamma_1 \text{ turns around } C^{-}. \end{cases}$$

As such, the periodic sequence $\{111\ldots\}$, or $\{\overline{1}\}$, corresponds to $\Gamma_1$ converging to the equilibrium state $C^{+}$ or a periodic orbit emerging from it through AH-bifurcation, while the sequence $\{100\ldots\}$ or $\{\overline{10}\}$ corresponds to $\Gamma_1$ converging to $C^{-}$ and so forth. Wherever small parameter variations do not change $\Gamma_1$-progressions and hence their binary representations, the system demonstrates structurally stable dynamics, which can be due to stable equilibria or periodic orbits (PO), such as the symmetric POs turning once [figure-8 shaped] or twice around $C^{-}$ and $C^{+}$ in Fig. 5.1d, with corresponding binary sequences $\{\overline{01}\}$ and $\{\overline{0011}\}$, resp. An aperiodic binary sequence is associated with chaotic dynamics that is characterized by the sensitive dependence on small parameter variations that change $\Gamma_1$-progressions and corresponding symbolic sequences (Fig. 5.1c). Changes occur at homoclinic bifurcations when $\Gamma_1$ comes back to saddle $O$. The primary homoclinic orbit (shown in Fig. 5.1a,f) coded with a finite sequence $\{1\}$ separates periodic patterns coded as $\{\overline{1}\}$ and $\{\overline{10}\}$. It occurs on the bifurcation curve $H_0$ in the $(a, b)$-parameter plane in Fig. 5.2. There are two special points labeled as $IF_1$ and $IF_2$ on $H_0$ that correspond to the so-called inclination-flip (IF) bifurcation of codimension-two [238]. Its feature is that it

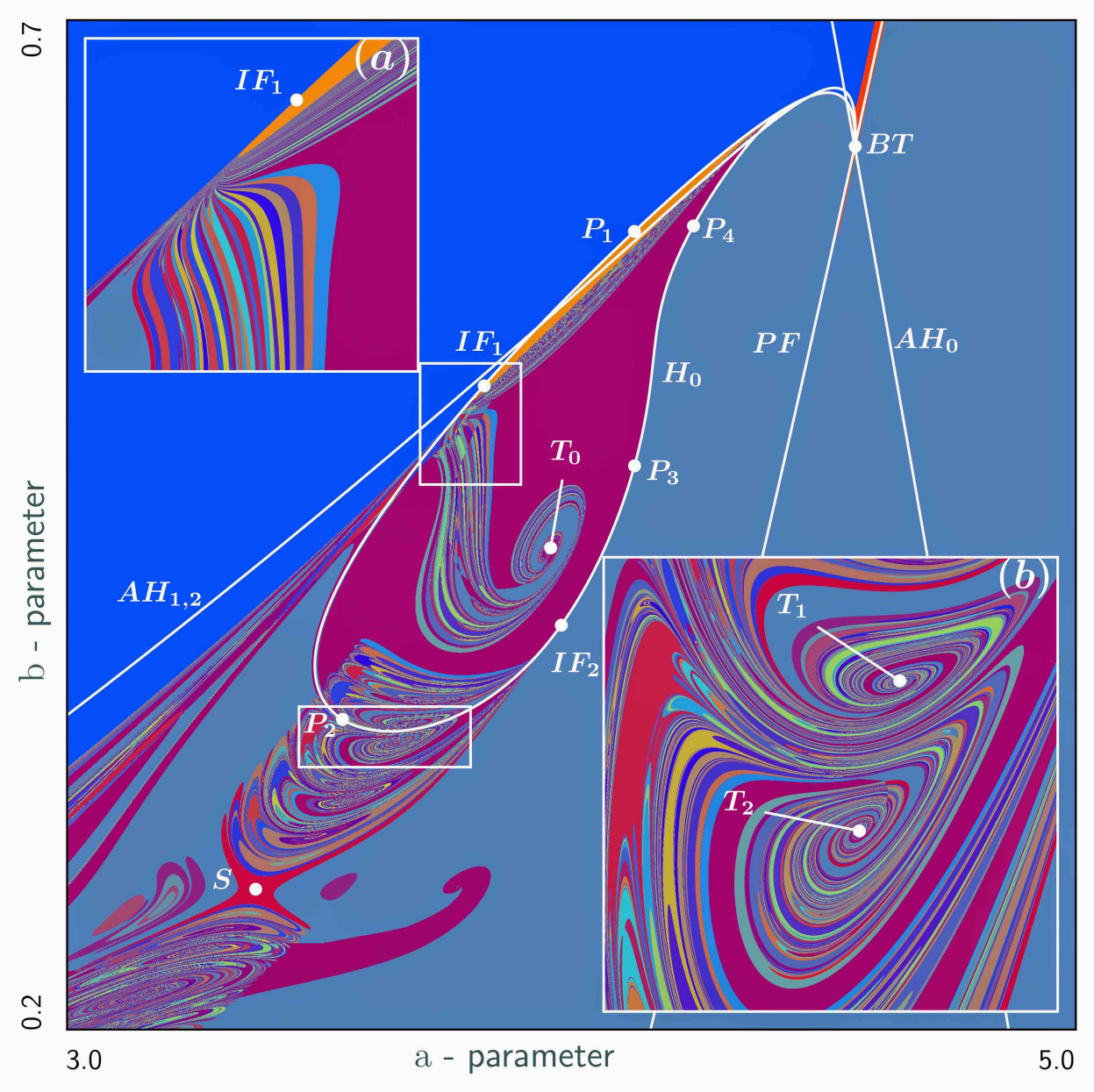


**Figure (5.2)** (color online) ($a$, $b$)-parameter sweep of [5–12]-length reveals an abundance of homoclinic bifurcations emerging from two cod-2 points, $IF_1$ & $IF_2$, on $H_0$, that corresponds to the primary homoclinic butterfly of saddle $O$, along with self-similar characteristic spirals around T-points, labelled $T_{0,1,2}$, corresponding to distinct heteroclinic cycles between $O$ and saddle-foci $C^{\pm}$. Cod-2 Bogdanov-Takens, $BT$, unfolding includes Andronov-Hopf $AH_0$, $AH_{1,2}$ and pitch-fork $PF$ bifurcation curves for $O$ and $C^{\pm}$, resp.; here $\sigma = 1.5$.

gives rise to instant homoclinic chaos in the phase space and complex bifurcation structures in the parameter space of the system. With our new computational-symbolic toolkit

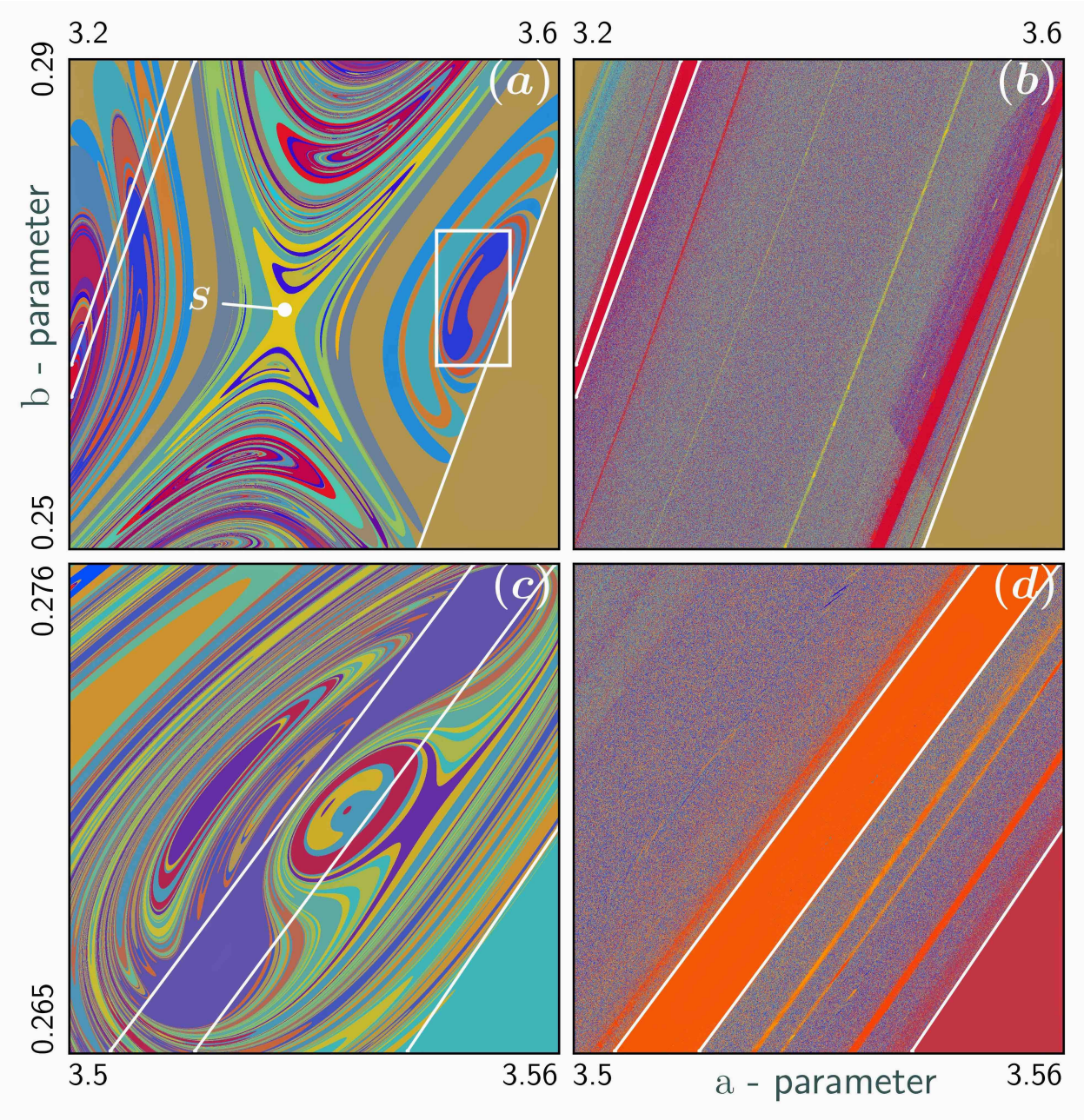


**Figure (5.3)** (color online) (a) Short [8–15] and (b,d) long [100–123]-length $(a, b)$-sweeps reveal fine self-similar organization of homo- and heteroclinic bifurcations underlying the regions of chaotic and regular dynamics of the laser model for $\sigma = 1.5$. A small area (white box) in (a) is magnified with a longer [15–22]-sweep in (c). (b,d) reveal stability windows (solid colors) within "noisy" regions of structurally unstable chaos; white lines demarcate boundaries of some stability windows.

we can clearly and quickly identify such bifurcations and their fine organizations in the parameter space along with regions of chaotic and regular dynamics. First, we define a

formal power series $P(N)$ for a finite binary sequence $\{k_n\}$ of length $N$, after omitting the first $j$ symbols for initial transients of the separatrix $\Gamma_1$ or any other trajectory, as follows:

$$P(N) = \sum_{n=j+1}^{j+N} \frac{k_n}{2^{(N+j+1)-n}}. \tag{5.2}$$

By construction, the range of $P(N)$ is [0, 1], including the sequences $\{\overline{0}\}$ and $\{\overline{1}\}$ (in the limit as $N \to \infty$). For example, $P(8)$ for the aperiodic sequence $\{10100101\}$ generated by $\Gamma_1$ in Fig. 5.1b, with $j = 0$ and $N = 8$, is given by: $P(8) = 1/2^8 + 0/2^7 + 1/2^6 + 0/2^5 + 0/2^4 + 1/2^3 + 0/2^2 + 1/2^1 = 0.64453125$. The $P$-quantities are used as invariants to discriminate or conjugate finite progressions of the separatrix $\Gamma_1$ of the saddle against each other to identify and trace down corresponding bifurcation curves in the parameter space. Moreover, the quantities generated from long periodic and aperiodic binary sequences let us efficiently detect regions of regular and chaotic dynamics, resp. Keeping $\sigma$ fixed at 1.2, 1.5 or 10, we 1) vary $a$ and $b$ to get a bi-parametric sweep on a 2000x2000 grid 2) to follow $\Gamma_1$-progressions 3) generating binary sequences $\{k_n\}$ that 4) result in $P(N)$-quantities. Next 5) we colormap all found $P(N)$ values onto the parameter plane, where regions are identified by their equivalent colors, and the borderlines between adjacent regions correspond to homoclinic bifurcation curves. The colormap differentiates between $P(N)$-values grouped into $2^8$ bins with preset RGB-color values. Numerical integration is performed using the classic Runge-Kutta method (RK4) with fixed step size $dt = 0.01$. The computation of these trajectories is massively parallelized by running on separate GPU threads using CUDA. This allows for the construction of bi-parametric scans such as Fig. 5.2, in as little as 8 seconds on an Nvidia Tesla K40 GPU. Visualizations are done in Python. In order to construct complex bifurcation structures in the 3D parametric space, such as Figs. 5.7a,5.8,5.10, we obtain a large number of biparametric scans in the $(a, b)$ parametric plane, as we continuously vary the third parameter $\sigma$. Such arrays of scans are then rendered together using the open source volume exploration tool Drishti [239], which performed the best with our huge datasets, compared to other avail-

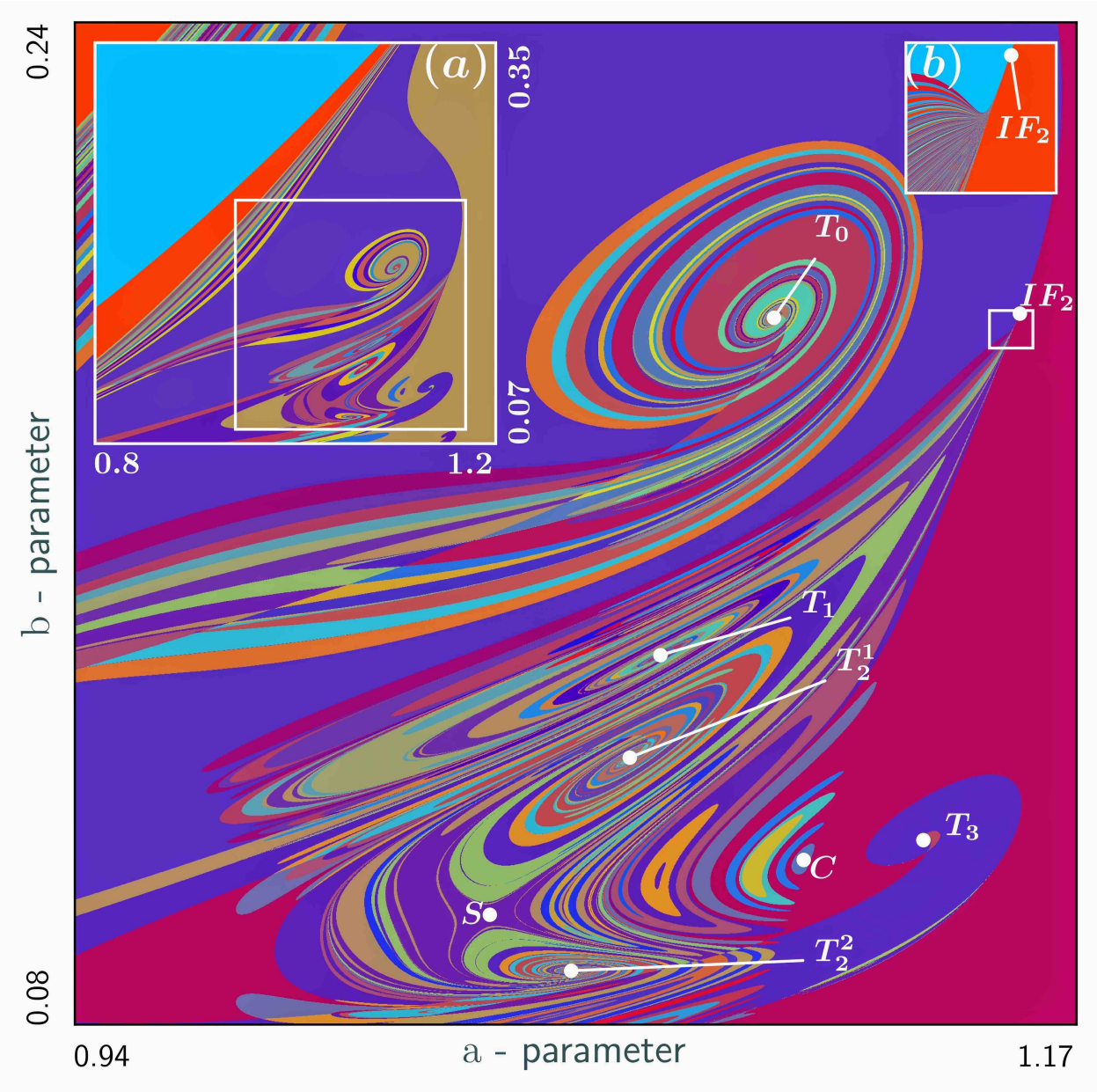


**Figure (5.4)** (color online) [2–9]-length sweep discloses organization of homo/heteroclinic bifurcations originating from cod-2 inclination-flip $IF_2$ and multiple T-points: primary $T_0$ coded as $\{1\bar{0}\}$, secondary $T_1$ as $\{10\bar{1}\}$, and a pair $T_2^1 - T_2^2$ with code $\{11\bar{0}\}$ separated by a saddle ($S$) in the $(a, b)$-parameter plane; here $\sigma = 10$. Inset (a) shows a larger $(a, b)$-sweep of [1–7]-length; (b) [16–23]-long sweep depicts dense loci of homoclinic bifurcation curves originating from $IF_2$.

able tools for 3D rendering. The open source software developed is available at `https://bitbucket.org/pusuluri_krishna/deterministicchaosprospector/`.

### 5.3.1 Transient dynamics

The sweep of [5–12]-length in Fig. 5.2 is superimposed with the curves, obtained by parametric continuation, corresponding to pitch-fork ($PF$), Andronov-Hopf ($AH_0$ and $AH_{1,2}$ for $O$ and $C^{\pm}$) and the primary homoclinic ($H_0$) bifurcations all originating from the codimension-2 Bogdanov-Takens point ($BT$) [238]. Fig. 5.1f shows how the primary homoclinic loop transmutes into a double loop along the curve $H_0$. The sweep reveals the way the inclination-flip $IF_1$ and $IF_2$ points give rise to jets of homoclinic bifurcation curves spiraling to various self-similar cod-2 Bykov terminal T-points, including $T_0$ and $T_1$, that correspond to heteroclinic connections linking the saddle $O$ with saddle-foci $C^+$, $C^-$ and generating periodic sequences $\{1\bar{0}\}$, $\{10\bar{1}\}$ (Fig. 5.1e), resp.

Figure 5.3a shows that with longer sequences we can obtain more detailed sweeps disclosing multiple T-points of smaller scales near the saddle point, $S$, that are not seen in Fig. 5.1. These spiral structures around T-points (identical to $T_2^1$ and $T_2^2$ in Fig. 5.4) morph into closed loops (like those shown in Fig. 5.3c) after collapsing into the saddle as $\sigma$-parameter is varied Figures 5.3b,d present the sweep of [100–123]-length, i.e., after skipping the first 100 transient symbols. Here regions with solid colors of constant $P(23)$-values represent the stability windows corresponding to simple (periodic) Morse-Smale dynamics, whereas multi-colored noisy regions refer to structurally unstable chaotic dynamics, as described later.

The ($a$, $b$)-sweep of [2-9]-length in Fig. 5.4 demonstrates the intrinsic re-arrangement of the bifurcation constituents of complexity for a different cut at $\sigma = 10$. Here, the secondary inclination-flip point, ($IF_2$), gives rise to loci of outgoing homoclinic curves that are re-directed by a saddle point ($S$), and spiral onto multiple T-points. The heteroclinic connections at the T-points, $T_0$-$T_3$, are given by $\{1\bar{0}\}$, $\{10\bar{1}\}$, $\{11\bar{0}\}$, and $\{\bar{1}\}$, respectively. The T-points $T_2^1$ and $T_2^2$, separated by the saddle $S$, correspond to the same heteroclinic connection $\{11\bar{0}\}$. Note that here the primary homoclinic curve spirals onto the primary T-point $T_0$. The T-point $T_3$ belongs to the stability window dominated by the symmetric

figure-8 periodic orbit (Fig. 5.1d) in the long run. The semi-annular structures around $C$ are, in fact, the remnants of the spirals around $T_3$, where the other halves of the spirals are disintegrated by the stable periodic orbit existing near $T_3$. With small $\sigma$-variations, $T_3$ crosses over the stability boundary near $C$, so that both ends of the semi-annular structures merge to complete spirals around $T_3$. Meanwhile, T-points $T_2^1$ and $T_2^2$ merge with the saddle $S$ to transform into concentric cycles.

### 5.3.2 Long-term system behavior

While a detailed sweep for short-term transient dynamics lets us reveal the underlying homoclinic bifurcations, longer sweeps omitting initial transients are designed to localize stability windows corresponding to regular dynamics and regions of chaotic dynamics in the parameter space. We implemented two algorithms into our computational DCP toolkit to classify such regions depending on whether the corresponding binary sequences of solutions are periodic or not for the given parameter values. The first algorithm based on Eq. (2) includes periodicity correction (PC) to identify periodic structure within a binary sequence and to normalize it to its smallest valued circular permutation. For example, the symmetric figure-8 periodic orbit in Fig. 5.1d is coded with $\{\overline{01}\}$) not with $\{\overline{10}\}$. The second algorithm utilizes the Lempel-Ziv-76 (LZ) compression [236], to determine the normalized complexity (the number of words in vocabulary per sequence length) of the binary sequence. The LZ compression algorithm scans a sequence from left to right and adds a new word to the vocabulary every time a previously unencountered substring is detected. Since all circular permutations of a periodic orbit have the same complexity, with this approach we can also detect stability windows amidst structurally unstable chaotic regions. This approach requiring only one solution per parameter set complements more expensive computational approaches based on the evaluations of the largest or several Lyapunov exponents.

Figure 5.5 represents the bi-parametric [1000-1999]-long sweeps to identify regions of simple and complex dynamics in model; here insets a/c and b/d represent the PC- and

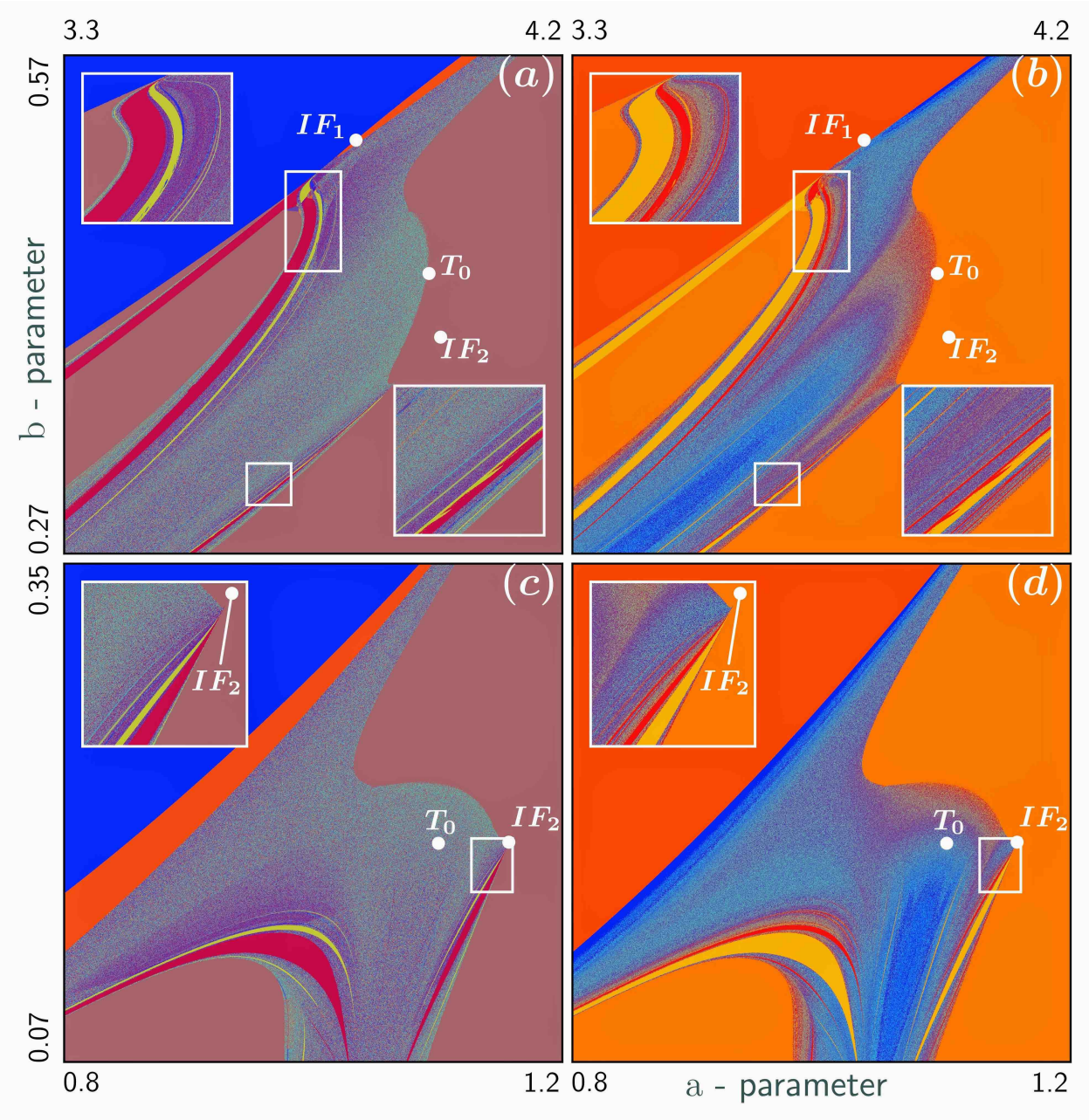


**Figure (5.5)** (color online) Long [1000–1999]-length sweeps to detect a multiplicity of stability windows (solid colors; dark red due to stable PO $\{\overline{0011}\}$) in Fig. 5.1d) within noisy/multi-color regions of chaos adjacent to $IF_1$ and $IF_2$ points in the $(a, b)$-parameter plane using PC algorithm in (a) and (c), and LZ-complexity in (b) and (d). Sweeps at $\sigma = 1.5$ (a,b) and $\sigma = 10$ (c,d) to compare with Fig. 5.2 and 5.4.

LZ-algorithm based sweeps, respectively. Regions of solid monotone colors correspond to the stability windows with stable equilibrium states and periodic orbits, while multi-

colored noisy regions indicate that the dynamics are structurally unstable and chaotic. The sweeps in Figs. 5a-b (at $\sigma = 1.5$) are superimposed with the primary and secondary inclination-flip points, $IF_1$ and $IF_2$, along with the primary T-point $T_0$ located next to the boundary between the regions of chaotic and stable periodic dynamics. They reveal multiple stability windows adjacent to $IF_1$ and $IF_2$ (magnified insets), including the wide one (in dark red) corresponding to a stable periodic orbit $\{\overline{0011}\}$ (shown in Fig. 5.1d). This approach can clearly identify distinct periodic orbits and their stability windows mapped by different colors. Note that same stability windows (indicated with same colors) emerge near both $IF_1$ and $IF_2$ in the reversed order. The sweeps in Figs. 5.5c-d (at $\sigma = 10$) depict the primary T-point $T_0$ located inside the region of chaotic dynamics, and the stability windows accumulating to $IF_2$. We note that the PC-algorithm lets one detect and identify a variety of stable periodic orbits efficiently even with short symbolic sequences (see Figs. 5.5b,d) compared to quite long sequences required by the LZ-algorithm that suits better for the detection of chaotic regions. To harness the best of both worlds, we can combine both PC and LZ, by first running the symbolic sequences through PC to detect the existence of, and to normalize, periodic orbits. The normalized sequences are then used to compute the power series sum $P$ and colored with the colormap as previously described. We then run aperiodic sequences through LZ to detect their complexity. We color the LZ-complexity values in shades of gray, with darker gray representing greater complexity. Together, this results in long term bi-parametric sweeps such as Figs. 5.6b.

## 5.4 Special organizing structures in parameter space

In this last section, we present a brief discussion of complex organizing structures in the parameter space, including inclination flip points, Bykov T-points, parametric saddles and isolas (isolated closed curves). Such structures have been theoretically described previously [240–243]. To our knowledge, this is the first detailed three dimensional computational reconstruction of such bifurcation surfaces in parameter space, made possible by the fast parallel computation of trajectories on GPUs.

### 5.4.1 Inclination flips and Bykov “terminal” T-points

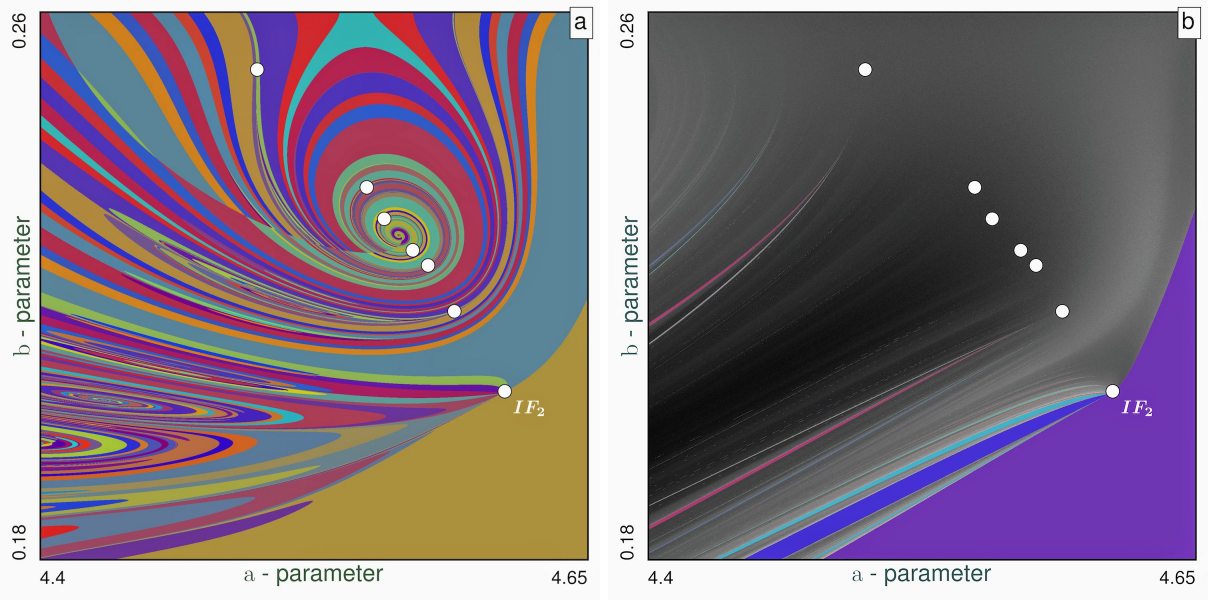


**Figure (5.6)** Short-term and long-term sweeps to disclose the multiplicity of basic inclination-flip bifurcation points (white dots) at $\sigma = 1.2$. **(a)** $\{k_i\}_{i=2}^{9}$ sweep illustrates a locus of homoclinic curves converging towards the primary and secondary T-points to the inclination-flip points $IF_2$ **(b)** Long $\{k_i\}_{i=1000}^{1999}$ DCP-based sweep reveals a variety of large and narrow stability windows, also known as the *Shilnikov flames*, originating below subsequent inclination flip points located on the boundary (not shown here) separating the region of the Lorenz attractor (above it) from that of quasi-attractors coexisting with stable periodic orbits.

A typical signature for Lorenz-like systems is the complex universal and self-similar characteristic spirals in the parameter plane, organized around a central point called a Bykov terminal point (T-point) as seen in Figs. 5.2,5.4. Each characteristic spiral around a T-point in the parameter plane corresponds to a homoclinic loop of the saddle $O$ in the phase space, such that with each turn of the spiral approaching the T-point, the outgoing separatrix of saddle makes increasing number of loops around a saddle-focus $C^{\pm}$, before finally forming a closed heteroclinic connection between the saddle and the saddle focus at the T-point. Fig. 5.1e shows a one-way heteroclinic connection (red) between the saddle and the saddle focus for parameter values near the T-point $T_1$ in Fig. 5.2b, with $(a, b) \sim (3.68179, 0.3517)$. Here, the unstable separatrix $\Gamma_1$ (red) of the saddle $O$ makes

one loop around $C^+$, followed by another loop around $C^-$, then merges with the incoming separatrix of $C^+$, thus effectively making infinite loops around $C^+$ before emerging out. The symmetric heteroclinic connection along $\Gamma_2$ from $O$ to $C^-$, is shown in blue.

Near a T-point, there exist countably many secondary T-points with increasing complexity of heteroclinic connections in the phase space and with similar bifurcation structures as the central T-point in the parameter plane, although on a smaller scale (see Figs. 5.2b, 5.6). Multiple inclination flip (IF) homoclinic bifurcations of the saddle occurring along the characteristic spirals of the T-points (detected with MatCont and shown as white dots in Fig. 5.6) give rise to saddle-node and period-doubling bifurcations of periodic orbits [70, 240]. Fine organization of the structure of the chaotic regions and stability windows near the T-point and surrounding IF points is revealed in greater detail in 5.6b. In addition, the unfolding of a T-point also includes other curves corresponding to the homoclinic connections of the saddle-focus satisfying the Shilnikov condition [77, 244, 245] that give rise to a denumerable set of saddle periodic orbits nearby [78], as well as those corresponding to heteroclinic connections between both saddle-foci [71, 246, 247].

We depict the parametric sweeps at $\sigma = 1.2$, which nicely summarize the behavior of the inclination flips and secondary T-points for short term (Fig. 5.6a, $\{k_i\}_{i=2}^{9}$) and long term dynamics (Fig. 5.6b, $\{k_i\}_{i=1000}^{1999}$ with DCP). Several inclination flips (white dots) close to the primary T-point $T_0$ are clearly seen as the congregation centers of homoclinic curves leading up to secondary T-points vis-à-vis transient dynamics, while those same inclination flip points also give rise to stability windows in the long term, amidst regions of structurally unstable and chaotic dynamics.

### 5.4.2 Parametric saddles for homoclinic curve branching

In this section, we describe a saddle in the parameter space that causes branch switching between homoclinic bifurcation curves. Between $\sigma = 1.5$ and $\sigma = 2.0$, the primary homoclinic bifurcation curve shifts from a complete loop to a spiral organization around the primary T-point $T_0$. This implies the existence of a saddle in between the

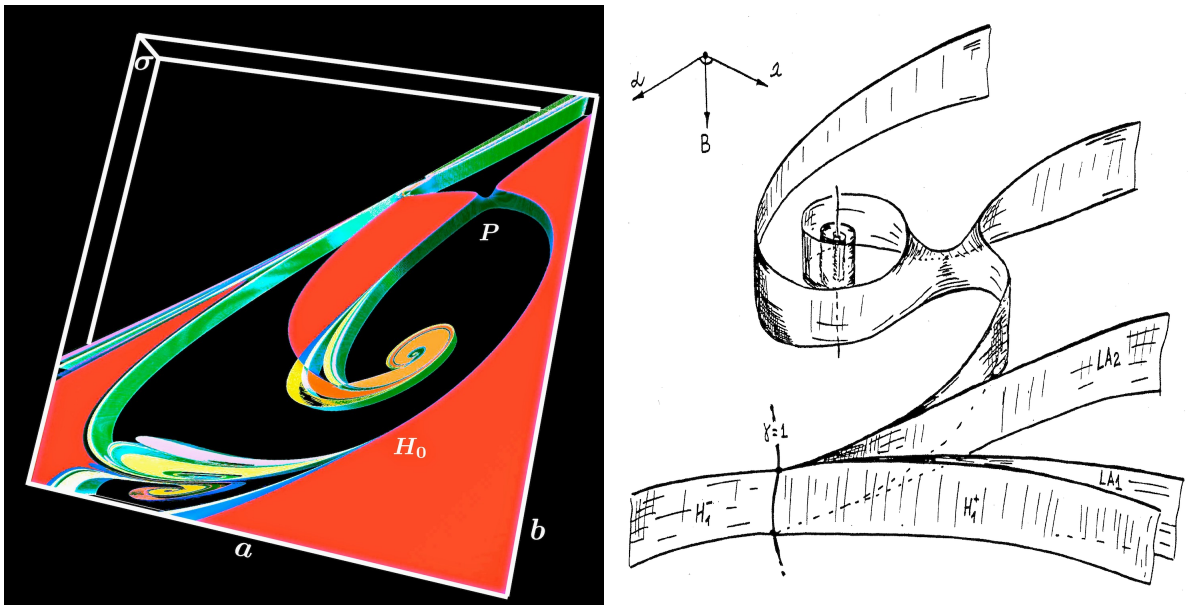


**Figure (5.7)** Bifurcation diagram in $(a, b, \sigma)$-parameter space showing the transformation of the primary homoclinic bifurcation curve $H_0$, when it starts to spiral towards the primary T-point $T_0$ instead of making a full loop (see Fig. 5.2). This 3D reconstruction (with $\sigma$ on the vertical axes) is made of 100 sweeps with $\{k_i\}_{i=0}^{7}$ in the range $1.7418$ (top)$\leq \sigma \leq 1.7439$ (bottom). The $P$-point marks the location of the branching saddle near $\sigma \approx 1.7428$. (right) Sketch of a bifurcation surface featuring a saddle causing the homoclinic bifurcation branching in the 3D parameter space of the Shimizu-Morioka system (courtesy A.L. Shilnikov et. al., 1993 [7])

two $\sigma$ values that branches the primary homoclinic bifurcation curve $H_0$. Fig. 5.7(left) shows a detailed 3D $(a, b, \sigma)$ bifurcation diagram close to this saddle. It is constructed using 100 bi-parametric sweeps in the $(a, b)$-plane with $1.7418$ (top surface) $\leq \sigma \leq 1.7439$ (bottom surface), using $\{k_i\}_{i=0}^{7}$ and 3D volume is rendered with Drishti software [239]. This branching of $H_0$ occurs at $\sigma \approx 1.7428$ and is marked by $P$. Detailed zooms close to $P$, shown in Fig. 5.8, further unravel this 3D organization of the homoclinic bifurcation surface at the homoclinic branching saddle $P$. A similar 3D bifurcation surface with a saddle in the Shimizu-Morioka system is presented in [7] and shown in Fig. 5.7(right).

### 5.4.3 Parametric saddles bridging T-points

We now focus on another kind of saddle ubiquitous to parametric sweeps, serving as a bridge between two identical T-points, marked $S$ in Figs.5.2,5.3,5.4. The interesting

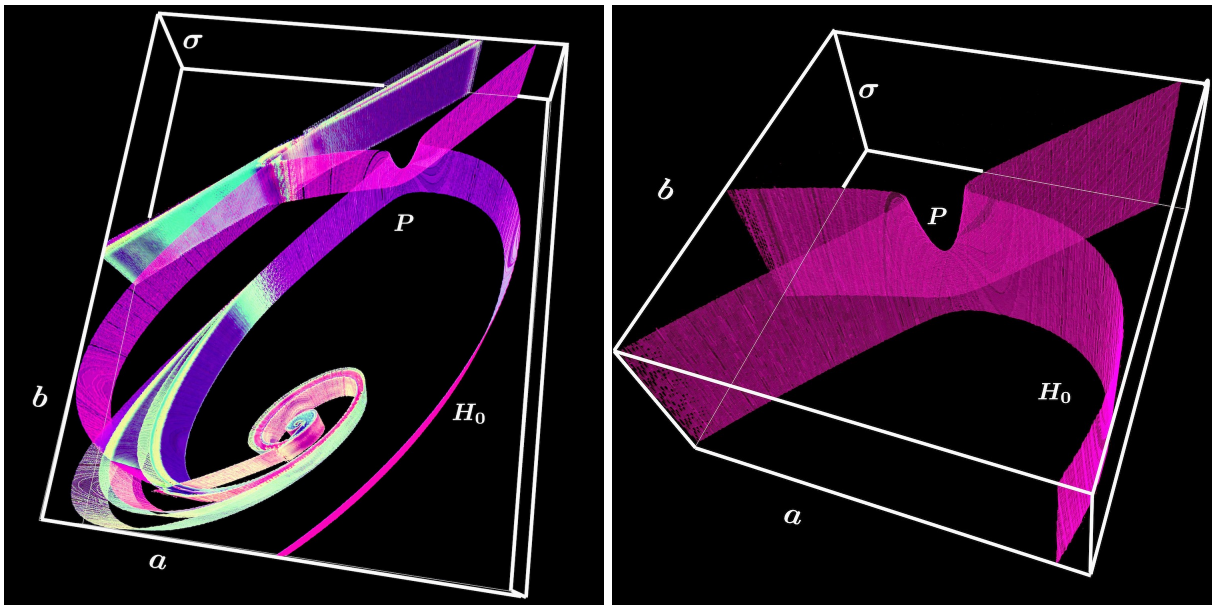


**Figure (5.8)** Magnifications of the saddle $P$ in Fig. 5.7 to better reveal the organization of the homoclinic bifurcation surface $H_0$ and how it branches to originate from 1D $IF_1$-curve and scroll onto the primary $T$-line in the $(a, b, \sigma)$-parameter space.

feature of such a saddle is that the T-point spirals above and below have identical construction and the same heteroclinic connections, as described previously in Fig. 5.4 for $\sigma = 10$, with $T_2^1$ above and $T_2^2$ below $S$. In order to see how such T-points on either side of a saddle are related to each other, we run multiple sweeps with closely varying $\sigma$ values and observe the structural changes in the spiral organization. Fig. 5.9 shows such chaotic mixing close to the saddle $S$ as $\sigma$ values are varied from **(a)** $\sigma = 1.372$, **(b)** $\sigma = 1.352$, **(c)** $\sigma = 1.288$, and through **(d)** $\sigma = 1.264$. As $\sigma$ changes, the T-points above and below the saddle appear to be merging together, as depicted in the transitions: Fig. 5.9a→b and Fig. 5.9c→d.

The 3D scrolling structure of the bifurcation surface around the hyperbolic saddle $S$ for $1.344 \leq \sigma \leq 1.374985$ constructed using 2000 bi-parametric sweeps using $\{k_i\}_{i=4}^{11}$ and rendered with open-source scientific visualization software *Drishti* is shown in Fig. 5.10. Fig. 5.10a,b,c reveal with gradually increasing depth, the continuous structural connections between the T-points on either side of this bridging saddle $S$. As we move along the T-point curve by varying $\sigma$, the curve undergoes a change in orientation and re-enters the

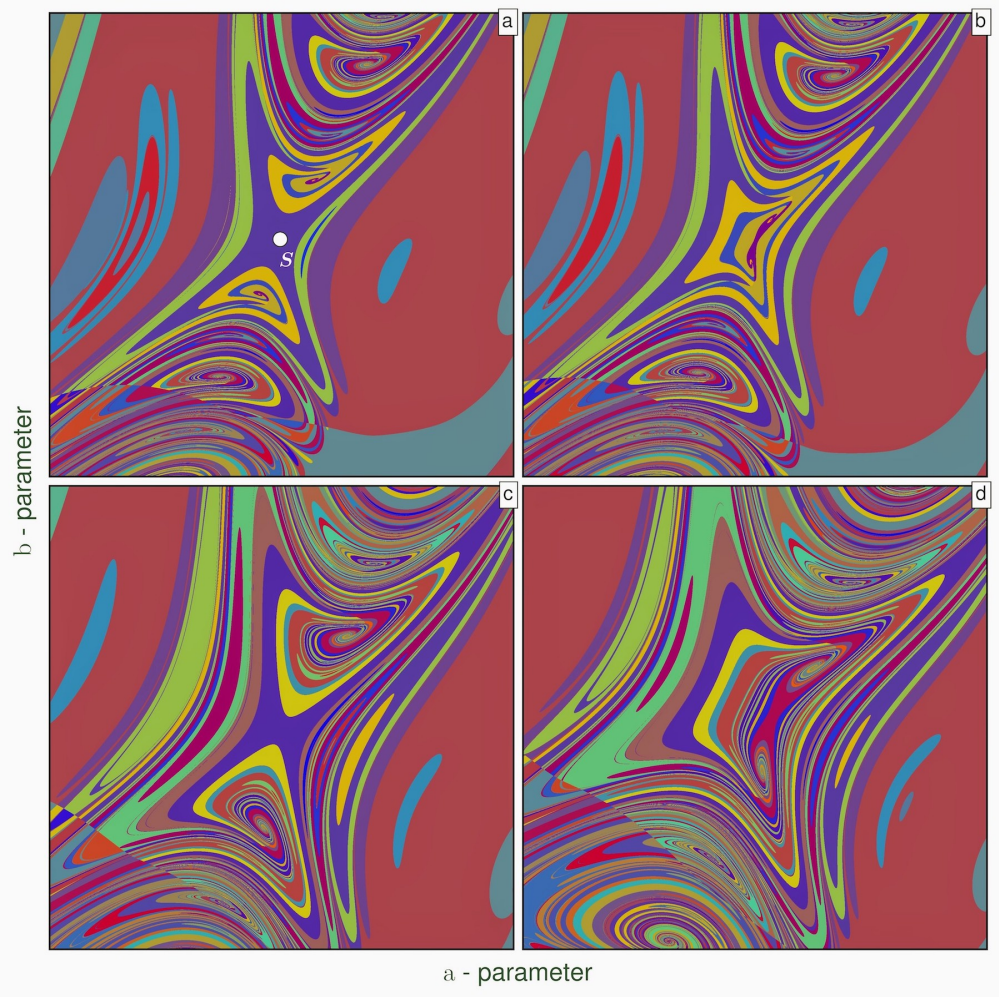


**Figure (5.9)** Chaotic mixing near the bridging saddle $S$ (white dot in panel (a)) (see Fig. 5.2) is revealed using four $\{k_i\}_{i=4}^{11}$-sweeps for varying $\sigma$ values: **(a)** $\sigma = 1.372$, **(b)** $\sigma = 1.352$, **(c)** $\sigma = 1.288$ and **(d)** $\sigma = 1.264$. As $\sigma$ is changed, the symmetric T-points (with an identical binary coding) above and below the saddle merge together, giving rise to annular isolas. Compare with Fig. 5.10 and watch the supplementary movie in the Appendix.

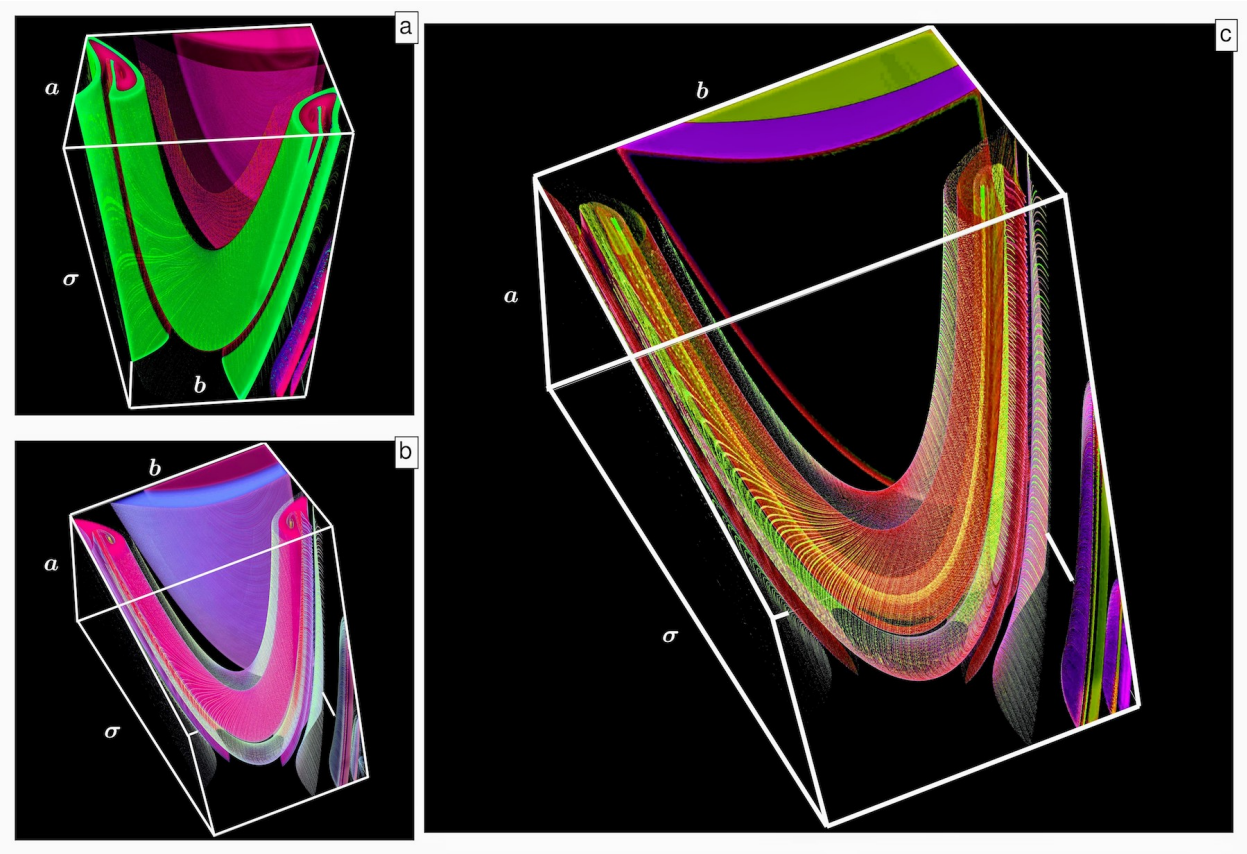


**Figure (5.10)** 3D bifurcation structure near the bridging saddle $S$ (see 2D bifurcation diagrams in Figs. 5.2 and 5.9) in the $(a, b, \sigma)$-parameter space is rendered using 2000 $\{k_i\}_{i=4}^{11}$-sweeps (each of 2000x2000-resolution) in the $\sigma$-range: $1.344 \leq \sigma \leq 1.374985$. It reveals the connectivity between two identical T-points on either side of the saddle, with a gradually increasing depth, as a bending T-curve with the saddle $S$ in the middle. Depending on how these structures are sliced, they will look like spirals or concentric circles/isolas in the corresponding 2D parametric sweeps shown above and below.

bifurcation planes of previous T-points, giving birth to the saddles in between them. Note that each sweep has 2000x2000 resolution. All 2000 such produced slices imply a total computation of $2000^3 = 8 \times 10^9$ trajectories. Despite being computationally heavy, this was achieved in just about 8 hours on a single Nvidia Tesla-K40 GPU.

### 5.4.4 Annular isolas from a bridging saddle

As seen in Fig. 5.9, as the T-points on either side of a bridging saddle merge together with varying $\sigma$, it results in the formation of isolas of homoclinic bifurcation curves

resembling concentric annular structures. This is due to the fact that the T-point curve changes its orientation with respect to the bifurcation planes and the T-point becomes non-transverse to this plane, which was described as a codimension-two-plus-one event [241, 242]. Such isolas are also seen in Figs.5.2,5.3,5.4. As we slice several $(a, b)$ bi-parametric sweeps in Fig. 5.10 for changing $\sigma$-values, moving from the top towards the bottom surface, the T-points appear to be merging as they become non-transverse to the bifurcation plane and we can only observe isolas made of homoclinic bifurcation curves. See [183] for a detailed description of semi-annular isolas arising from the ghost of a T-point ($T_3$) as seen near the point $C$ in Fig.5.4, where the other halves of the spirals are disintegrated by the stable periodic orbit.

## 5.5 Summary

In this chapter, we presented a novel framing combining applied dynamical systems, GPU-based parallel computation, and 2D/3D parameter space visualization to extend the theory of non-local homoclinic bifurcations of lower codimensions. With this approach we can explore and determine the universal rules of complex dynamics in diverse systems. We could identify regions of simple and chaotic dynamics in the parameter space of a classic nonlinear laser model with a Lorenz-like attractor, as well as disclose the key underlying bifurcation structures, including Bykov T-point spirals and inclination flips. We performed detailed computational reconstruction and visualization of the 3D embedding of bifurcation surfaces, parametric saddles and isolas. This methodology and understanding can further advance the studies of cross-disciplinary nonlinear phenomena across biological, medical, and engineering systems [89].

### Supplementary Material

Parameters of the model are set as follows:

Fig. 5.1: (a) trajectory $\{1\}$ ($a = 3.827$, $b = 0.51903$); trajectory $\{11...\}$ ($a = 3.827$, $b = 0.54$); trajectory $\{10...\}$ ($a = 3.827$, $b = 0.50$); background ($a = 3.765$, $b = .4$); (b)

trajectory $\{10100101...\}$ ($a = 3.765$, $b = .44$); (c) trajectory $\{10100110...\}$ ($a = 3.765$, $b = .47$); (d) periodic orbit $\{\overline{01}\}$ ($a = 4.2$, $b = 0.583$); periodic orbit $\{\overline{0011}\}$ ($a = 3.37326$, $b = 0.313333$); (e) $T_1$ ($a = 3.68199$, $b = .35171$); (f) chaotic background of one-sided loops ($a = 3.72$, $b = 0.48954338$);

Fig. 5.2: $T_0$ ($a = 3.95902$, $b = 0.438616$); $S$ ($a = 3.37386$, $b = 0.269558$); $BT$ ($a = 4.56255$, $b = 0.637487$); $P_1$ ($a = 4.124910$, $b = 0.595354$); $IF_1$ ($a = 3.827$, $b = 0.51903$); $P_2$ ($a = 3.546020$, $b = 0.353647$); $IF_2$ ($a = 3.98$, $b = .40037$); $P_3$ ($a = 4.125120$, $b = 0.479283$); $P_4$ ($a = 4.241910$, $b = 0.598092$);

Fig. 5.3: $S$ ($a = 3.37386$, $b = 0.269558$);

Fig. 5.4: $IF_2$ ($a = 1.157$, $b = 0.1935$); $T_0$ ($a = 1.10054$, $b = 0.192854$); $T_1$ ($a = 1.07446$, $b = .138992$); $T_2^1$ ($a = 1.06744$, $b = .122637$); $T_2^2$ ($a = 1.05398$, $b = .0885933$); $T_3$ ($a = 1.13485$, $b = .109461$); $C$ ($a = 1.10738$, $b = .106295$); $T_1$ ($a = 1.03528$, $b = .0975449$);

Fig. 5.10: Bottom surface $a \in (3.68, 3.86)$, $b \in (0.23, 0.255)$; Top surface; $a \in (3.57, 3.86)$, $b \in (0.235, 0.27)$; $1.344$(bottom surface) $\leq \sigma \leq 1.374985$(top surface)

# CHAPTER 6

# CONCLUSIONS

This project is truly cross-disciplinary, requiring the formulation, development and integration of theories, models and tools spanning across several research scopes including *(a)* central pattern generators and coupled oscillators; *b)* dynamical systems analysis, homoclinic chaos, and mathematical modeling; *(c)* high-performance GPU computing, visualization, and unsupervised machine learning. Although the particular emphasis of this project is in understanding network phenomena in Neuroscience, we also demonstrate the applications of these tools to study nonlinear phenomena occurring in diverse disciplines. This will help to bridge some of the gap in communication and enable multidisciplinary cooperation between researchers in Neuroscience and other non-linear science communities.

## Multistability analysis

This project extends our knowledge of the principles guiding multi-stable rhythmic behaviors in complex neural network topologies from their basic constituent motifs and allows us to predict the changes in patterns of activity and multistability, based on changes in the network configurations and external inputs. It also helps us to understand the plausible biophysical mechanisms that control and modulate rhythmic activity. We showed how network topologies and synaptic changes can alter the rhythmic behavior of the network and promote or suppress multistability. This can generate verifiable hypotheses for neurophysiological experiments and manipulations of real animal CPGs with dynamic clamp technique [199]. We identified network topologies that produce robust monostable rhythms and are resilient to external perturbations. This can also help non-biological systems from engineering, economics, and environmental studies, where loss of resilience

is a challenge to predict and can cause catastrophic effects. Future studies can be expanded to the complete dynamical analysis of detailed and realistic animal CPG models. Such understanding is essential to study motor control, dynamic memory, information processing, and decision making in animals and humans [200]. It also has implications for gaining insights into complex neurological phenomena in higher animals along with neurological disorders related to CPG arrhythmia, and the development of mechanisms to treat such disorders. Before such techniques can be applied to humans, we need to achieve a comprehensive understanding of the working of these modular networks in lower animals and through computational models. An important aspect of this analytical technique is that it is valid across a wide range of oscillatory networks without dependence on the underlying mathematical equations and hence is applicable to a variety of rhythmic neuronal and non-neuronal activities beyond motor control. This can further be expanded to the study of real world neural networks composed of large populations of neurons. While this project deals with networks of neurons, the methodology might also be applied to study networks of brain regions that synergistically excite or inhibit each other and produce rhythmic patterns of firing. Hence the modeling approaches could enhance whole brain computational modeling research that models the structural and functional connectivity across several parcellations of the human brain to study various cognitive processes during resting state, task conditions, or under pathological disorders [201, 202].

**Symbolic dynamics**

The symbolic methods developed will expedite examinations of dynamics of simple and biologically plausible models of individual neurons, as well as emergent network behaviors and the sweeps of their parameter spaces. For Lorenz like systems with homoclinic chaos, these tools will help identify the essential organizing structures of complexity such as the various homoclinic, heteroclinic connections and characteristic spirals of Bykov terminal points, in addition to detecting regions of simple, stable dynamics or those with structurally unstable, chaotic dynamics in the parameter space. Such complex

behaviors can also occur in neural and other biological systems at transitions between oscillatory activity types. The symbolic toolkit can thus offset and complement other computational tools such as spike counting, Lyapunov exponents and parameter continuation to study a broad spectrum of complex dynamical phenomena and will help determine the origin and universal rules of complex dynamics. Such symbolic approaches in conjunction with the previously described multistability analysis can lead to improved insights for data analysis of event related brain potentials, functional neuroimaging and cognition [248–256].

**Computational advances**

Computationally expensive simulations are sped up by making use of parallel computing and GPU based technologies such as CUDA, OpenAcc, OpenMP, and OpenMPI [3–5, 47, 48]. This allows the reconstruction of highly detailed biparametric sweeps and bifurcation diagrams in just a few seconds, as well as enable highly detailed three dimensional sweeps. Multistability analysis of larger networks using Poincare return maps is automated using unsupervised machine learning [40–46]. The insights in CPG multistability gained from this research will help in the design and development of more efficient robot locomotion [203–214]. The computational tools developed in the project will benefit a wide audience of interdisciplinary researchers for studies of a variety of diverse nonlinear applications. The tools developed are open source and freely available online at the following repositories, including some that are simple and readily accessible for classroom teaching: *a)* `https://bitbucket.org/pusuluri_krishna/deterministicchaosprospector/`

*b)* `https://github.com/jusjusjus/Motiftoolbox`

*c)* `https://bitbucket.org/pusuluri_krishna/cpg_multistability/`

# REFERENCES

[1] O. Sporns and R. Kötter, “Motifs in brain networks,” *PLoS biology*, vol. 2, no. 11, p. e369, 2004.

[2] A. Sakurai and P. S. Katz, “Artificial synaptic rewiring demonstrates that distinct neural circuit configurations underlie homologous behaviors,” *Current Biology*, vol. 27, no. 12, pp. 1721–1734, 2017.

[3] K. Pusuluri, A. Pikovsky, and A. Shilnikov, “Unraveling the chaos-land and its organization in the rabinovich system,” in *Advances in Dynamics, Patterns, Cognition*. Springer, 2017, pp. 41–60.

[4] K. Pusuluri and A. Shilnikov, “Homoclinic chaos and its organization in a nonlinear optics model,” *Phys. Rev. E*, vol. 98, p. 040202, Oct 2018. [Online]. Available: https://link.aps.org/doi/10.1103/PhysRevE.98.040202

[5] ——, “Symbolic representation of neuronal dynamics,” in *Advances on Nonlinear Dynamics of Electronic Systems*. World Scientific, 2019, pp. 97–102. [Online]. Available: https://www.worldscientific.com/doi/abs/10.1142/9789811201523_0018

[6] A. Shilnikov and G. Cymbalyuk, “Homoclinic saddle-node orbit bifurcations en a route between tonic spiking and bursting in neuron models, invited paper,” *Regular & Chaotic Dynamics*, vol. 9, pp. 281–297, 2004.

[7] A. Shilnikov, “On bifurcations of the Lorenz attractor in the Shimizu-Morioka model,” *Physica D*, vol. 62(1-4), pp. 338–346, 1993.

[8] E. Bullmore and O. Sporns, “Complex brain networks: graph theoretical analysis of structural and functional systems,” *Nature Reviews Neuroscience*, vol. 10, no. 3, p. 186, 2009.

[9] F. Azam, “Biologically inspired modular neural networks,” Ph.D. dissertation, Virginia Tech, 2000.

[10] D. Meunier, R. Lambiotte, and E. T. Bullmore, “Modular and hierarchically modular organization of brain networks,” *Frontiers in neuroscience*, vol. 4, p. 200, 2010.

[11] J. P. Miller and A. I. Selverston, “Neural mechanisms for the production of the lobster pyloric motor pattern,” in *Model neural networks and behavior*. Springer, 1985, pp. 37–48.

[12] T. Bal, F. Nagy, and M. Moulins, “The pyloric central pattern generator in crustacea: a set of conditional neuronal oscillators,” *Journal of Comparative Physiology A*, vol. 163, no. 6, pp. 715–727, 1988.

[13] E. Marder and R. L. Calabrese, “Principles of rhythmic motor pattern generation,” *Physiological reviews*, vol. 76, no. 3, pp. 687–717, 1996.

[14] W. B. Kristan Jr, R. L. Calabrese, and W. O. Friesen, “Neuronal control of leech behavior,” *Progress in neurobiology*, vol. 76, no. 5, pp. 279–327, 2005.

[15] R. J. Calin-Jageman, M. J. Tunstall, B. D. Mensh, P. S. Katz, and W. N. Frost, “Parameter space analysis suggests multi-site plasticity contributes to motor pattern initiation in tritonia,” *Journal of Neurophysiology*, vol. 98, no. 4, pp. 2382–2398, 2007.

[16] W. E. Sherwood, R. Harris-Warrick, and J. Guckenheimer, “Synaptic patterning of left-right alternation in a computational model of the rodent hindlimb central pattern generator,” *Journal of computational neuroscience*, vol. 30, no. 2, pp. 323–360, 2011.

[17] J. M. Newcomb, A. Sakurai, J. L. Lillvis, C. A. Gunaratne, and P. S. Katz, “Homology and homoplasy of swimming behaviors and neural circuits in the nudipleura

(mollusca, gastropoda, opisthobranchia)," *Proceedings of the National Academy of Sciences*, vol. 109, no. Supplement 1, pp. 10 669–10 676, 2012.

[18] R. Milo, S. Shen-Orr, S. Itzkovitz, N. Kashtan, D. Chklovskii, and U. Alon, "Network motifs: simple building blocks of complex networks," *Science*, vol. 298, no. 5594, pp. 824–827, 2002.

[19] M. I. Rabinovich, P. Varona, A. I. Selverston, and H. D. Abarbanel, "Dynamical principles in neuroscience," *Reviews of modern physics*, vol. 78, no. 4, p. 1213, 2006.

[20] A. Bulloch and N. Syed, "Reconstruction of neuronal networks in culture," *Trends in Neurosciences*, vol. 15, no. 11, pp. 422–427, 1992.

[21] E. Marder, "Invertebrate neurobiology: Polymorphic neural networks," *Current Biology*, vol. 4, no. 8, pp. 752–754, 1994.

[22] W. N. Frost and P. S. Katz, "Single neuron control over a complex motor program," *Proceedings of the National Academy of Sciences*, vol. 93, no. 1, pp. 422–426, 1996.

[23] P. S. Katz, "Evolution of central pattern generators and rhythmic behaviours," *Philosophical Transactions of the Royal Society B*, vol. 371, no. 1685, pp. 20 150 057–20 150 057, 2016.

[24] J. Wojcik, J. Schwabedal, R. Clewley, and A. L. Shilnikov, "Key bifurcations of bursting polyrhythms in 3-cell central pattern generators," *PloS one*, vol. 9, no. 4, p. e92918, 2014.

[25] D. Alacam and A. Shilnikov, "Making a swim central pattern generator out of latent parabolic bursters," *International Journal of Bifurcation and Chaos*, vol. 25, no. 07, p. 1540003, 2015.

[26] J. Wojcik, R. Clewley, and A. Shilnikov, “Order parameter for bursting polyrhythms in multifunctional central pattern generators,” *Physical Review E*, vol. 83, no. 5, p. 056209, 2011.

[27] T. G. Brown, “The intrinsic factors in the act of progression in the mammal,” *Proc. R. Soc. Lond. B*, vol. 84, no. 572, pp. 308–319, 1911.

[28] S. Jalil, D. Allen, J. Youker, and A. Shilnikov, “Toward robust phase-locking in melibe swim central pattern generator models,” *Chaos: An Interdisciplinary Journal of Nonlinear Science*, vol. 23, no. 4, p. 046105, 2013.

[29] A. Sakurai and P. Katz, “Distinct neural circuit architectures produce analogous rhythmic behaviors in related species,” in *Soc. Neurosci. Abstr*, vol. 37, no. 04, 2011.

[30] A. Sakurai, J. M. Newcomb, J. L. Lillvis, and P. S. Katz, “Different roles for homologous interneurons in species exhibiting similar rhythmic behaviors,” *Current Biology*, vol. 21, no. 12, pp. 1036–1043, 2011.

[31] A. Sakurai, C. A. Gunaratne, and P. S. Katz, “Two interconnected kernels of reciprocally inhibitory interneurons underlie alternating left-right swim motor pattern generation in the mollusk melibe leonina,” *Journal of neurophysiology*, vol. 112, no. 6, pp. 1317–1328, 2014.

[32] P. S. Katz, “Comparison of extrinsic and intrinsic neuromodulation in two central pattern generator circuits in invertebrates,” *Experimental Physiology*, vol. 83, no. 3, pp. 281–292, 1998.

[33] N. Kopell and B. Ermentrout, “Chemical and electrical synapses perform complementary roles in the synchronization of interneuronal networks,” *Proceedings of the National Academy of Sciences*, vol. 101, no. 43, pp. 15 482–15 487, 2004.

[34] K. Matsuoka, “Mechanisms of frequency and pattern control in the neural rhythm generators,” *Biological cybernetics*, vol. 56, no. 5-6, pp. 345–353, 1987.

[35] N. Kopell, “Toward a theory of modelling generators,” *Neural control of rhythmic movements in vertebrates*, 1988.

[36] C. Canavier, D. Baxter, J. Clark, and J. Byrne, “Multiple modes of activity in a model neuron suggest a novel mechanism for the effects of neuromodulators,” *Journal of neurophysiology*, vol. 72, no. 2, pp. 872–882, 1994.

[37] F. Skinner, N. Kopell, and E. Marder, “Mechanisms for oscillation and frequency control in networks of mutually inhibitory relaxation oscillators,” *J. Comput. Neurosci*, vol. 1, pp. 69–87, 1994.

[38] R. Dror, C. C. Canavier, R. J. Butera, J. W. Clark, and J. H. Byrne, “A mathematical criterion based on phase response curves for stability in a ring of coupled oscillators,” *Biological cybernetics*, vol. 80, no. 1, pp. 11–23, 1999.

[39] A. A. Prinz, C. P. Billimoria, and E. Marder, “Alternative to hand-tuning conductance-based models: construction and analysis of databases of model neurons,” *Journal of neurophysiology*, vol. 90, no. 6, pp. 3998–4015, 2003.

[40] D. S. Wilks, “Cluster analysis,” in *International geophysics*. Elsevier, 2011, vol. 100, pp. 603–616.

[41] A. K. Jain, M. N. Murty, and P. J. Flynn, “Data clustering: a review,” *ACM computing surveys (CSUR)*, vol. 31, no. 3, pp. 264–323, 1999.

[42] M. Längkvist, L. Karlsson, and A. Loutfi, “A review of unsupervised feature learning and deep learning for time-series modeling,” *Pattern Recognition Letters*, vol. 42, pp. 11–24, 2014.

[43] F. Pedregosa, G. Varoquaux, A. Gramfort, V. Michel, B. Thirion, O. Grisel, M. Blondel, P. Prettenhofer, R. Weiss, V. Dubourg *et al.*, “Scikit-learn: Machine learning

in python," *Journal of machine learning research*, vol. 12, no. Oct, pp. 2825–2830, 2011.

[44] F. Murtagh, "A survey of recent advances in hierarchical clustering algorithms," *The Computer Journal*, vol. 26, no. 4, pp. 354–359, 1983.

[45] R. Gentleman and V. Carey, "Unsupervised machine learning," in *Bioconductor Case Studies*. Springer, 2008, pp. 137–157.

[46] S. C. Johnson, "Hierarchical clustering schemes," *Psychometrika*, vol. 32, no. 3, pp. 241–254, 1967.

[47] W. Wang, L. Xu, J. Cavazos, H. H. Huang, and M. Kay, "Fast acceleration of 2d wave propagation simulations using modern computational accelerators," *PloS one*, vol. 9, no. 1, p. e86484, 2014.

[48] E. Yavuz, J. Turner, and T. Nowotny, "Genn: a code generation framework for accelerated brain simulations," *Scientific reports*, vol. 6, p. 18854, 2016.

[49] A. Shilnikov, "Complete dynamical analysis of a neuron model," *Nonlinear Dynamics*, vol. 68, no. 3, pp. 305–328, 2012.

[50] H. Ju, A. Neiman, and A. Shilnikov, "Bottom-up approach to torus bifurcation in neuron models," *arXiv preprint arXiv:1805.11719*, 2018.

[51] R. Barrio, M. Angeles Martínez, S. Serrano, and A. Shilnikov, "Macro-and micro-chaotic structures in the hindmarsh-rose model of bursting neurons," *Chaos: An Interdisciplinary Journal of Nonlinear Science*, vol. 24, no. 2, p. 023128, 2014.

[52] R. Barrio and A. Shilnikov, "Parameter-sweeping techniques for temporal dynamics of neuronal systems: case study of hindmarsh-rose model," *The Journal of Mathematical Neuroscience*, vol. 1, no. 1, p. 6, 2011.

[53] A. B. Neiman, K. Dierkes, B. Lindner, L. Han, and A. L. Shilnikov, “Spontaneous voltage oscillations and response dynamics of a hodgkin-huxley type model of sensory hair cells,” *The Journal of Mathematical Neuroscience*, vol. 1, no. 1, p. 11, 2011.

[54] P. Channell, I. Fuwape, A. B. Neiman, and A. L. Shilnikov, “Variability of bursting patterns in a neuron model in the presence of noise,” *Journal of computational neuroscience*, vol. 27, no. 3, p. 527, 2009.

[55] J.-W. Shuai and D. M. Durand, “Phase synchronization in two coupled chaotic neurons,” *Physics Letters A*, vol. 264, no. 4, pp. 289–297, 1999.

[56] M. F. Simoni and S. P. DeWeerth, “Two-dimensional variation of bursting properties in a silicon-neuron half-center oscillator,” *IEEE Transactions on Neural Systems and Rehabilitation Engineering*, vol. 14, no. 3, pp. 281–289, 2006.

[57] G. J. Gutierrez, T. O’Leary, and E. Marder, “Multiple mechanisms switch an electrically coupled, synaptically inhibited neuron between competing rhythmic oscillators,” *Neuron*, vol. 77, no. 5, pp. 845–858, 2013.

[58] A. A. Prinz, D. Bucher, and E. Marder, “Similar network activity from disparate circuit parameters,” *Nature neuroscience*, vol. 7, no. 12, pp. 1345–1352, 2004.

[59] P. Friedrich, M. Vella, A. I. Gulyás, T. F. Freund, and S. Káli, “A flexible, interactive software tool for fitting the parameters of neuronal models,” *Frontiers in neuroinformatics*, vol. 8, p. 63, 2014.

[60] J. E. Rubin and D. Terman, “Explicit maps to predict activation order in multiphase rhythms of a coupled cell network,” *The Journal of Mathematical Neuroscience*, vol. 2, no. 1, p. 4, 2012.

[61] W. B. Kristan, “Neuronal decision-making circuits,” *Current Biology*, vol. 18, no. 19, pp. R928–R932, 2008.

[62] K. L. Briggman and W. Kristan Jr, “Multifunctional pattern-generating circuits,” *Annu. Rev. Neurosci.*, vol. 31, pp. 271–294, 2008.

[63] J. Collens, “Rhythmogenesis and bifurcation analysis of 3-node neural network kernels,” 2017.

[64] T. Xing, “Computational study in chaotic dynamical systems and mechanisms for pattern generation in three-cell networks,” 2015.

[65] D. Alacam, “Modeling rhythm generation in swim central pattern generator of melibe leonina,” 2017.

[66] A. Shilnikov, R. Gordon, and I. Belykh, “Polyrhythmic synchronization in bursting networking motifs,” *Chaos: An Interdisciplinary Journal of Nonlinear Science*, vol. 18, no. 3, p. 037120, 2008.

[67] R. L. Calabrese, B. J. Norris, A. Wenning, and T. M. Wright, “Coping with variability in small neuronal networks,” 2011.

[68] J. T. Schwabedal, D. E. Knapper, and A. L. Shilnikov, “Qualitative and quantitative stability analysis of penta-rhythmic circuits,” *Nonlinearity*, vol. 29, no. 12, p. 3647, 2016.

[69] V. S. Afraimovich, V. V. Bykov, and L. P. Shilnikov, “The origin and structure of the Lorenz attractor,” *Sov. Phys. Dokl.*, vol. 22, pp. 253–255, 1977.

[70] L. P. Shilnikov, A. L. Shilnikov, D. Turaev, and L. O. Chua, *Methods of Qualitative Theory in Nonlinear Dynamics*. Singapore: World Sci. Publ., 1998, 2001, vol. 1-2.

[71] V. V. Bykov, “On the structure of bifurcations sets of synamical systems that are systems with a separatrix contour containing saddle-focus,” *Methods of Qualitative Theory of Differential Equations, Gorky University (in Russian).*, pp. 44–72, 1980.

[72] V. S. Afraimovich, S. V. Gonchenko, L. M. Lerman, A. L. Shilnikov, and D. V. Turaev, "Regular and chaotic dynamics," *Scientific heritage of L.P. Shilnikov. Part 1*, vol. 4, no. 19, pp. 435–462, 2014.

[73] D. Aubin and A. Dahan Dalmedico, "Writing the history of dynamical systems and chaos: longue durée and revolution, disciplines and cultures," *Historia Math.*, vol. 29, no. 3, pp. 273–339, 2002.

[74] L. A. Belyakov, "Bifurcations of systems with a homoclinic curve of the saddle-focus with a zero saddle value," *Mat. Zametki*, vol. 36, no. 5, pp. 681–689, 798, 1984.

[75] J. Guckenheimer and R. F. Williams, "Structural stability of Lorenz attractors," *Inst. Hautes Études Sci. Publ. Math.*, vol. 50, no. 50, pp. 59–72, 1979.

[76] A. Shilnikov, "Bifurcation and chaos in the Morioka-Shimizu system," *Selecta Math. Soviet.*, vol. 10(2), pp. 105–117, 1991.

[77] L. P. Shilnikov, "A case of the existence of a denumerable set of periodic motions," *Dokl. Akad. Nauk SSSR*, vol. 160, pp. 558–561, 1965.

[78] L. Shilnikov, "The existence of a denumerable set of periodic motions in four-dimensional space in an extended neighborhood of a saddle-focus." *Soviet Math. Dokl.*, vol. 8(1), pp. 54–58, 1967.

[79] A. Shilnikov, "Complete dynamical analysis of an interneuron model," *J. Nonlinear Dynamics*, vol. 68, no. 3, pp. 305–328, 2012.

[80] S. Gonchenko, I. Ovsyannikov, C. Simo, and D. Turaev, "Three-dimensional Hénon-like maps and wild Lorenz-like attractors," *Inter. J. Bif. Chaos*, vol. 15(11), pp. 3493–3508, 2005.

[81] V. V. Bykov, "Bifurcations leading to chaos in Chua's circuit," *Inter. J. Bif. Chaos*, vol. 8, pp. 685–699, 1998.

[82] V. S. Afraimovich and L. P. Shilnikov, “Strange attractors and quasiattractors,” in *Nonlinear dynamics and turbulence*, ser. Interaction Mech. Math. Ser. Boston, MA: Pitman, 1983, pp. 1–34.

[83] L. P. Shilnikov, A. L. Shilnikov, D. V. Turaev, and L. O. Chua, *Methods of Qualitative Theory in Nonlinear Dynamics. Part I*. Singapore: World Scientific, 1998.

[84] A. J. Homburg and B. Sandstede, “Homoclinic and heteroclinic bifurcations in vector fields,” in *Handbook of Dynamical Systems*, H. W. Broer, B. Hasselblatt, and F. Takens, Eds. Elsevier Science, 2010, vol. 3, ch. 8, pp. 379–524.

[85] R. Barrio, A. Shilnikov, and L. Shilnikov, “Kneadings, symbolic dynamics and painting Lorenz chaos,” *Int. J. Bifurcation & Chaos*, vol. 22, no. 04, p. 1230016, 2012.

[86] T. Xing, R. Barrio, and A. Shilnikov, “Symbolic quest into homoclinic chaos,” *Int. J. Bifurcation & Chaos*, vol. 24, no. 8, p. 1440004, 2014.

[87] J. V. Moloney, J. S. Uppal, and R. G. Harrison, “Origin of chaotic relaxation oscillations in an optically pumped molecular laser,” *PRL*, vol. 59, no. 25, p. 2868, 1987.

[88] W. Forysiak, J. V. Moloney, and R. G. Harrison, “Bifurcations of an optically pumped three-level laser model,” *Physica D*, vol. 53, no. 1, pp. 162 – 186, 1991.

[89] K. Pusuluri, H. Ju, and A. Shilnikov, *Chaotic Dynamics in Neural Systems*. Berlin, Heidelberg: Springer Berlin Heidelberg, 2020, pp. 1–13. [Online]. Available: https://doi.org/10.1007/978-3-642-27737-5_738-1

[90] G. S. Cymbalyuk, Q. Gaudry, M. A. Masino, and R. L. Calabrese, “Bursting in leech heart interneurons: cell-autonomous and network-based mechanisms,” *Journal of Neuroscience*, vol. 22, no. 24, pp. 10 580–10 592, 2002.

[91] R. Bertram, “A computational study of the effects of serotonin on a molluscan burster neuron,” *Biological Cybernetics*, vol. 69, no. 3, pp. 257–267, 1993.

[92] C. Canavier, D. Baxter, J. Clark, and J. Byrne, "Nonlinear dynamics in a model neuron provide a novel mechanism for transient synaptic inputs to produce long-term alterations of postsynaptic activity," *Journal of neurophysiology*, vol. 69, no. 6, pp. 2252–2257, 1993.

[93] R. J. Butera Jr, "Multirhythmic bursting," *Chaos: An Interdisciplinary Journal of Nonlinear Science*, vol. 8, no. 1, pp. 274–284, 1998.

[94] F. Fröhlich and M. Bazhenov, "Coexistence of tonic firing and bursting in cortical neurons," *Physical Review E*, vol. 74, no. 3, p. 031922, 2006.

[95] J. Hounsgaard and O. Kiehn, "Serotonin-induced bistability of turtle motoneurones caused by a nifedipine-sensitive calcium plateau potential." *The Journal of physiology*, vol. 414, no. 1, pp. 265–282, 1989.

[96] H. Lechner, D. Baxter, J. Clark, and J. Byrne, "Bistability and its regulation by serotonin in the endogenously bursting neuron r15 in aplysia," *Journal of neurophysiology*, vol. 75, no. 2, pp. 957–962, 1996.

[97] G. G. Turrigiano, E. Marder, and L. Abbott, "Cellular short-term memory from a slow potassium conductance," *Journal of neurophysiology*, vol. 75, no. 2, pp. 963–966, 1996.

[98] M. I. Rabinovich, P. Varona, A. I. Selverston, and H. D. Abarbanel, "Dynamical principles in neuroscience," *Reviews of modern physics*, vol. 78, no. 4, p. 1213, 2006.

[99] S. Rinaldi and S. Muratori, "Slow-fast limit cycles in predator-prey models," *Ecological Modelling*, vol. 61, no. 3-4, pp. 287–308, 1992.

[100] D. J. DeShazer, J. García-Ojalvo, and R. Roy, "Bursting dynamics of a fiber laser with an injected signal," *Physical Review E*, vol. 67, no. 3, p. 036602, 2003.

[101] E. Shochat and V. Rom-Kedar, “Novel strategies for granulocyte colony-stimulating factor treatment of severe prolonged neutropenia suggested by mathematical modeling,” *Clinical Cancer Research*, vol. 14, no. 20, pp. 6354–6363, 2008.

[102] M. Steriade, E. G. Jones, and R. R. Llinás, *Thalamic oscillations and signaling.* John Wiley & Sons, 1990.

[103] K. L. Briggman and W. Kristan Jr, “Multifunctional pattern-generating circuits,” *Annu. Rev. Neurosci.*, vol. 31, pp. 271–294, 2008.

[104] N. Kopell, “Toward a theory of modelling generators,” *Neural control of rhythmic movements in vertebrates*, 1988.

[105] E. Marder and R. L. Calabrese, “Principles of rhythmic motor pattern generation,” *Physiological reviews*, vol. 76, no. 3, pp. 687–717, 1996.

[106] P. S. Katz, “Tritonia swim network,” *Scholarpedia*, vol. 4, no. 5, p. 3638, 2009.

[107] A. Shilnikov, R. Gordon, and I. Belykh, “Polyrhythmic synchronization in bursting networking motifs,” *Chaos: An Interdisciplinary Journal of Nonlinear Science*, vol. 18, no. 3, p. 037120, 2008.

[108] W. B. Kristan Jr, R. L. Calabrese, and W. O. Friesen, “Neuronal control of leech behavior,” *Progress in neurobiology*, vol. 76, no. 5, pp. 279–327, 2005.

[109] W. B. Kristan and P. Katz, “Form and function in systems neuroscience,” *Current biology*, vol. 16, no. 19, pp. R828–R831, 2006.

[110] W. B. Kristan Jr, R. L. Calabrese, and W. O. Friesen, “Neuronal control of leech behavior,” *Progress in neurobiology*, vol. 76, no. 5, pp. 279–327, 2005.

[111] K. L. Briggman and W. B. Kristan, “Imaging dedicated and multifunctional neural circuits generating distinct behaviors,” *Journal of Neuroscience*, vol. 26, no. 42, pp. 10 925–10 933, 2006.

[112] D. Alaçam and A. L. Shilnikov, “Making a swim central pattern generator out of latent parabolic bursters,” *J. Bifurcations and Chaos*, vol. 25, no. 7, p. 1540003, 2015.

[113] M. Steriade, D. A. McCormick, and T. J. Sejnowski, “Thalamocortical oscillations in the sleeping and aroused brain,” *Science*, vol. 262, no. 5134, pp. 679–685, 1993.

[114] J. E. Rubin and D. Terman, “High frequency stimulation of the subthalamic nucleus eliminates pathological thalamic rhythmicity in a computational model,” *Journal of computational neuroscience*, vol. 16, no. 3, pp. 211–235, 2004.

[115] M. Bazhenov, I. Timofeev, M. Steriade, and T. Sejnowski, “Spiking-bursting activity in the thalamic reticular nucleus initiates sequences of spindle oscillations in thalamic networks,” *Journal of neurophysiology*, vol. 84, no. 2, pp. 1076–1087, 2000.

[116] I. Timofeev, M. Bazhenov, T. Sejnowski, and M. Steriade, “Cortical hyperpolarization-activated depolarizing current takes part in the generation of focal paroxysmal activities,” *Proceedings of the National Academy of Sciences*, vol. 99, no. 14, pp. 9533–9537, 2002.

[117] J. Guckenheimer, “Towards a global theory of singularly perturbed dynamical systems,” in *Nonlinear Dynamical Systems and Chaos*. Springer, 1996, pp. 213–225.

[118] V. Belykh, I. Belykh, M. Colding-Jørgensen, and E. Mosekilde, “Homoclinic bifurcations leading to the emergence of bursting oscillations in cell models,” *The european physical journal E*, vol. 3, no. 3, pp. 205–219, 2000.

[119] B. Doiron, C. Laing, A. Longtin, and L. Maler, “Ghostbursting: a novel neuronal burst mechanism,” *Journal of computational neuroscience*, vol. 12, no. 1, pp. 5–25, 2002.

[120] C. R. Laing, B. Doiron, A. Longtin, L. Noonan, R. W. Turner, and L. Maler, “Type i burst excitability,” *Journal of computational neuroscience*, vol. 14, no. 3, pp. 329–342, 2003.

[121] P. F. Rowat and R. C. Elson, “State-dependent effects of na channel noise on neuronal burst generation,” *Journal of Computational Neuroscience*, vol. 16, no. 2, pp. 87–112, 2004.

[122] A. Shilnikov and G. Cymbalyuk, “Transition between tonic spiking and bursting in a neuron model via the blue-sky catastrophe,” *Physical review letters*, vol. 94, no. 4, p. 048101, 2005.

[123] A. Shilnikov, R. L. Calabrese, and G. Cymbalyuk, “Mechanism of bistability: tonic spiking and bursting in a neuron model,” *Physical Review E*, vol. 71, no. 5, p. 056214, 2005.

[124] G. Cymbalyuk and A. Shilnikov, “Coexistence of tonic spiking oscillations in a leech neuron model,” *Journal of computational neuroscience*, vol. 18, no. 3, pp. 255–263, 2005.

[125] P. Channell, G. Cymbalyuk, and A. Shilnikov, “Origin of bursting through homoclinic spike adding in a neuron model,” *Physical Review Letters*, vol. 98, no. 13, p. 134101, 2007.

[126] A. Shilnikov and M. Kolomiets, “Methods of the qualitative theory for the hindmarsh–rose model: A case study–a tutorial,” *International Journal of Bifurcation and chaos*, vol. 18, no. 08, pp. 2141–2168, 2008.

[127] M. A. Kramer, R. D. Traub, and N. J. Kopell, “New dynamics in cerebellar purkinje cells: torus canards,” *Physical review letters*, vol. 101, no. 6, p. 068103, 2008.

[128] A. L. Shilnikov, L. P. Shilnikov, and D. V. Turaev, “Blue-sky catastrophe in singularly perturbed systems,” *Moscow Mathematical Journal*, vol. 5, no. 1, pp. 269–282, 2005.

[129] L. P. Shilnikov, A. L. Shilnikov, and D. V. Turaev, “Showcase of blue sky catastro-

phes," *International Journal of Bifurcation and Chaos*, vol. 24, no. 08, p. 1440003, 2014.

[130] L. P. Shil'nikov, *Methods of qualitative theory in nonlinear dynamics*. World Scientific, 2001, vol. 5.

[131] A. L. Shilnikov and N. F. Rulkov, "Origin of chaos in a two-dimensional map modeling spiking-bursting neural activity," *International Journal of Bifurcation and Chaos*, vol. 13, no. 11, pp. 3325–3340, 2003.

[132] ——, "Subthreshold oscillations in a map-based neuron model," *Physics Letters A*, vol. 328, no. 2-3, pp. 177–184, 2004.

[133] T. R. Chay, "Chaos in a three-variable model of an excitable cell," *Physica D: Nonlinear Phenomena*, vol. 16, no. 2, pp. 233–242, 1985.

[134] G. S. Medvedev, "Reduction of a model of an excitable cell to a one-dimensional map," *Physica D: Nonlinear Phenomena*, vol. 202, no. 1-2, pp. 37–59, 2005.

[135] R. E. Griffiths and M. Pernarowski, "Return map characterizations for a model of bursting with two slow variables," *SIAM Journal on Applied Mathematics*, vol. 66, no. 6, pp. 1917–1948, 2006.

[136] A. L. Hodgkin and A. F. Huxley, "A quantitative description of membrane current and its application to conduction and excitation in nerve," *The Journal of physiology*, vol. 117, no. 4, pp. 500–544, 1952.

[137] P. Channell Jr, G. Cymbalyuk, and A. Shilnikov, "Applications of the poincare mapping technique to analysis of neuronal dynamics," *Neurocomputing*, vol. 70, no. 10-12, pp. 2107–2111, 2007.

[138] J. Rinzel and G. B. Ermentrout, "Analysis of neural excitability and oscillations," *Methods in neuronal modeling*, vol. 2, pp. 251–292, 1998.

[139] B. Ermentrout, “Type i membranes, phase resetting curves, and synchrony,” *Neural computation*, vol. 8, no. 5, pp. 979–1001, 1996.

[140] J. Wojcik and A. Shilnikov, “Voltage interval mappings for activity transitions in neuron models for elliptic bursters,” *Physica D: Nonlinear Phenomena*, vol. 240, no. 14-15, pp. 1164–1180, 2011.

[141] X.-J. Wang and J. Rinzel, “Oscillatory and bursting properties of neurons,” in *The handbook of brain theory and neural networks*. MIT Press, 1998, pp. 686–691.

[142] J. Rinzel, “Bursting oscillations in an excitable membrane model,” in *Ordinary and partial differential equations*. Springer, 1985, pp. 304–316.

[143] R. Bertram, M. J. Butte, T. Kiemel, and A. Sherman, “Topological and phenomenological classification of bursting oscillations,” *Bulletin of mathematical biology*, vol. 57, no. 3, pp. 413–439, 1995.

[144] E. M. Izhikevich, “Neural excitability, spiking and bursting,” *International journal of bifurcation and chaos*, vol. 10, no. 06, pp. 1171–1266, 2000.

[145] ——, *Dynamical systems in neuroscience*. MIT press, 2007.

[146] A. Tikhonov, “On the dependence of the solutions of differential equations on a small parameter,” *Matematicheskii sbornik*, vol. 64, no. 2, pp. 193–204, 1948.

[147] L. S. Pontryagin and L. Rodygin, “Periodic solution of a system of ordinary differential equations with a small parameter in the terms containing derivatives,” in *Doklady Akademii Nauk*, vol. 132, no. 3. Russian Academy of Sciences, 1960, pp. 537–540.

[148] N. Fenichel, “Geometric singular perturbation theory for ordinary differential equations,” *Journal of differential equations*, vol. 31, no. 1, pp. 53–98, 1979.

[149] E. Mischenko and N. K. Rozov, “Differential equations with small parameters and relaxation oscillations, plenum press new york and london (1980). 14 e. nelson,

internal set theory: a new approach to nonstandard analysis, bull. amer. math. soc., 83 (6)(1977) 1165-1198. 15] van der pol, relaxation oscillations, philos. mag. 2 7 (1926) 978 992."

[150] A. Androvov, A. Vitt, and S. Khaikin, "Theory of oscillations," 1966.

[151] E. Mishchenko, *Asymptotic methods in singularly perturbed systems*.

[152] C. Jones and N. Kopell, "Tracking invariant manifolds with differential forms in singularly perturbed systems," *Journal of Differential Equations*, vol. 108, no. 1, pp. 64–88, 1994.

[153] V. Arnol'd, V. Afrajmovich, Y. S. Il'yashenko, and L. Shil'nikov, "Bifurcation theory and catastrophe theory," *Encyclopaedia of Mathematical Sciences (Dynamical systems V)*, vol. 5, 1994.

[154] D. Terman, "The transition from bursting to continuous spiking in excitable membrane models," *Journal of Nonlinear Science*, vol. 2, no. 2, pp. 135–182, 1992.

[155] A. V. Holden and Y.-S. Fan, "From simple to simple bursting oscillatory behaviour via chaos in the rose-hindmarsh model for neuronal activity," *Chaos, Solitons & Fractals*, vol. 2, no. 3, pp. 221–236, 1992.

[156] X.-J. Wang, "Genesis of bursting oscillations in the hindmarsh-rose model and homoclinicity to a chaotic saddle," *Physica D: Nonlinear Phenomena*, vol. 62, no. 1-4, pp. 263–274, 1993.

[157] U. Feudel, A. Neiman, X. Pei, W. Wojtenek, H. Braun, M. Huber, and F. Moss, "Homoclinic bifurcation in a hodgkin–huxley model of thermally sensitive neurons," *Chaos: An Interdisciplinary Journal of Nonlinear Science*, vol. 10, no. 1, pp. 231–239, 2000.

[158] B. Deng and G. Hines, "Food chain chaos due to shilnikov's orbit," *Chaos: An Interdisciplinary Journal of Nonlinear Science*, vol. 12, no. 3, pp. 533–538, 2002.

[159] R. C. Elson, R. Huerta, H. D. Abarbanel, M. I. Rabinovich, and A. I. Selverston, "Dynamic control of irregular bursting in an identified neuron of an oscillatory circuit," *Journal of Neurophysiology*, vol. 82, no. 1, pp. 115–122, 1999.

[160] R. Barrio, M. Angeles Martínez, S. Serrano, and A. Shilnikov, "Macro-and micro-chaotic structures in the hindmarsh-rose model of bursting neurons," *Chaos: An Interdisciplinary Journal of Nonlinear Science*, vol. 24, no. 2, p. 023128, 2014.

[161] B. Deng, "Glucose-induced period-doubling cascade in the electrical activity of pancreatic $\beta$-cells," *Journal of mathematical biology*, vol. 38, no. 1, pp. 21–78, 1999.

[162] A. Hutt *et al.*, "Sequences by metastable attractors: interweaving dynamical systems and experimental data," *Frontiers in Applied Mathematics and Statistics*, vol. 3, p. 11, 2017.

[163] P. beim Graben, K. K. Sellers, F. Fröhlich, and A. Hutt, "Optimal estimation of recurrence structures from time series," *EPL (Europhysics Letters)*, vol. 114, no. 3, p. 38003, 2016.

[164] P. B. Graben and A. Hutt, "Detecting metastable states of dynamical systems by recurrence-based symbolic dynamics," 2013.

[165] P. beim Graben and A. Hutt, "Detecting event-related recurrences by symbolic analysis: applications to human language processing," *Philosophical Transactions of the Royal Society A: Mathematical, Physical and Engineering Sciences*, vol. 373, no. 2034, p. 20140089, 2015.

[166] C. Mira, *Chaotic dynamics: from the one-dimensional endomorphism to the two-dimensional diffeomorphism*. World Scientific, 1987.

[167] C. Mira and A. Shilnikov, "Slow–fast dynamics generated by noninvertible plane maps," *International Journal of Bifurcation and Chaos*, vol. 15, no. 11, pp. 3509–3534, 2005.

[168] R. L. Devaney, “A first course in chaotic dynamical systems addison wesley publishing company,” 1992.

[169] A. Sharkovsky, S. Kolyada, A. Sivak, and V. Fedorenko, *Dynamics of one-dimensional maps*. Springer Science & Business Media, 2013, vol. 407.

[170] J. Best, A. Borisyuk, J. Rubin, D. Terman, and M. Wechselberger, “The dynamic range of bursting in a model respiratory pacemaker network,” *SIAM Journal on Applied Dynamical Systems*, vol. 4, no. 4, pp. 1107–1139, 2005.

[171] L. P. Shilnikov, A. L. Shilnikov, and D. V. Turaev, “Showcase of blue sky catastrophes,” *International Journal of Bifurcation and Chaos*, vol. 24, no. 08, p. 1440003, 2014.

[172] L. Shil’nikov and D. Turaev, “Simple bifurcations leading to hyperbolic attractors,” *Computers & Mathematics with Applications*, vol. 34, no. 2-4, pp. 173–193, 1997.

[173] L. P. Shilnikov and D. V. Turaev, “A new simple bifurcation of a periodic orbit of blue sky catastrophe type,” *Translations of the American Mathematical Society-Series 2*, vol. 200, pp. 165–188, 2000.

[174] N. Gavrilov and A. Shilnikov, “Example of a blue sky catastrophe,” *Translations of the American Mathematical Society-Series 2*, vol. 200, pp. 99–106, 2000.

[175] R. H. Abraham, “Chaostrophes, intermittency, and noise,” *Chaos, fractals, and dynamics*, pp. 3–22, 1985.

[176] V. I. Luk’yanov and L. P. Shilnikov, “On some bifurcations of dynamical systems with homoclinic structures,” in *Doklady Akademii Nauk*, vol. 243, no. 1. Russian Academy of Sciences, 1978, pp. 26–29.

[177] N. Gavrilov and L. Šil’nikov, “On three-dimensional dynamical systems close to systems with a structurally unstable homoclinic curve. i,” *Mathematics of the USSR-Sbornik*, vol. 17, no. 4, p. 467, 1972.

[178] A. A. Prinz, “Rhythmic pattern generation in invertebrates,” in *The Oxford Handbook of Invertebrate Neurobiology*. Oxford University Press, 2019, p. 391.

[179] A. Sakurai and P. S. Katz, “The central pattern generator underlying swimming in dendronotus iris: a simple half-center network oscillator with a twist,” *Journal of neurophysiology*, vol. 116, no. 4, pp. 1728–1742, 2016.

[180] P. S. Katz and A. Sakurai, “Neural control of swimming in nudipleura mollusks,” in *The Oxford Handbook of Invertebrate Neurobiology*, 2017.

[181] K. Pusuluri, S. Basodi, and A. Shilnikov, “Computational exposition of multistable rhythms in 4-cell neural circuits,” *Communications in Nonlinear Science and Numerical Simulation*, vol. 83, p. 105139, 2020.

[182] J. Collens, K. Pusiluri, A. Kelly, D. Knapper, T. Xing, S. Basodi, D. Alacam, and A. Shilnikov, “Dynamics and bifurcations in multistable 3-cell neural networks,” *Chaos: An Interdisciplinary Journal of Nonlinear Science*, 2020, submitted.

[183] K. Pusuluri, H. Meijer, and A. Shilnikov, “Homoclinic puzzles and chaos in a nonlinear laser model,” *Communications in Nonlinear Science and Numerical Simulation*, 2020, submitted.

[184] T. Xing, J. Wojcik, M. A. Zaks, and A. Shilnikov, “Fractal parameter space of lorenz-like attractors: a hierarchical approach,” in *Chaos, Information Processing And Paradoxical Games: The Legacy Of John S Nicolis*. World Scientific, 2015, pp. 87–104.

[185] T. Xing, R. Barrio, and A. Shilnikov, “Symbolic quest into homoclinic chaos,” *International Journal of Bifurcation and Chaos*, vol. 24, no. 08, p. 1440004, 2014.

[186] R. Barrio, F. Blesa, S. Serrano, T. Xing, and A. Shilnikov, “Homoclinic spirals: Theory and numerics,” in *Progress and Challenges in Dynamical Systems*. Springer, 2013, pp. 53–64.

[187] R. Barrio, A. Shilnikov, and L. Shilnikov, “Kneadings, symbolic dynamics and painting lorenz chaos,” *International Journal of Bifurcation and Chaos*, vol. 22, no. 04, p. 1230016, 2012.

[188] R. J. Butera Jr, “Multirhythmic bursting,” *Chaos: An Interdisciplinary Journal of Nonlinear Science*, vol. 8, no. 1, pp. 274–284, 1998.

[189] R. Perlman, C. Kaufman, and M. Speciner, *Network security: private communication in a public world*. Pearson Education India, 2016.

[190] A. Lempel and J. Ziv, “On the complexity of finite sequences,” *IEEE Transactions on information theory*, vol. 22, no. 1, pp. 75–81, 1976.

[191] K. Pusuluri, S. Basodi, and A. Shilnikov, “Computational exposition of multistable rhythms in 4-cell neural circuits,” *Communications in Nonlinear Science and Numerical Simulation*, vol. 83, p. 105139, 2020.

[192] J. Rubin and D. Terman, “Geometric analysis of population rhythms in synaptically coupled neuronal networks,” *Neural computation*, vol. 12, no. 3, pp. 597–645, 2000.

[193] F. Skinner, L. Zhang, J. P. Velazquez, and P. Carlen, “Bursting in inhibitory interneuronal networks: a role for gap-junctional coupling,” *Journal of neurophysiology*, vol. 81, no. 3, pp. 1274–1283, 1999.

[194] C. Van Vreeswijk, L. Abbott, and G. B. Ermentrout, “When inhibition not excitation synchronizes neural firing,” *Journal of computational neuroscience*, vol. 1, no. 4, pp. 313–321, 1994.

[195] S. Jalil, I. Belykh, and A. Shilnikov, “Fast reciprocal inhibition can synchronize bursting neurons,” *Physical Review E*, vol. 81, no. 4, p. 045201, 2010.

[196] ——, “Spikes matter in phase-locking of inhibitory bursting networks,” *Phys Rev E*, vol. 85, p. 36214, 2012.

[197] N. W. Schultheiss, A. A. Prinz, and R. J. Butera, *Phase response curves in neuroscience: theory, experiment, and analysis*. Springer Science & Business Media, 2011.

[198] I. Belykh, E. de Lange, and M. Hasler, "Synchronization of bursting neurons: What matters in the network topology," *Physical review letters*, vol. 94, no. 18, p. 188101, 2005.

[199] I. Kemenes, V. Marra, M. Crossley, D. Samu, K. Staras, G. Kemenes, and T. Nowotny, "Dynamic clamp with stdpc software," *Nature protocols*, vol. 6, no. 3, p. 405, 2011.

[200] T. Kee, P. Sanda, N. Gupta, M. Stopfer, and M. Bazhenov, "Feed-forward versus feedback inhibition in a basic olfactory circuit," *PLoS computational biology*, vol. 11, no. 10, p. e1004531, 2015.

[201] G. Deco, G. Tononi, M. Boly, and M. L. Kringelbach, "Rethinking segregation and integration: contributions of whole-brain modelling," *Nature Reviews Neuroscience*, vol. 16, no. 7, p. 430, 2015.

[202] V. K. Jirsa, W. C. Stacey, P. P. Quilichini, A. I. Ivanov, and C. Bernard, "On the nature of seizure dynamics," *Brain*, vol. 137, no. 8, pp. 2210–2230, 2014.

[203] G. Ren, W. Chen, S. Dasgupta, C. Kolodziejski, F. Wörgötter, and P. Manoonpong, "Multiple chaotic central pattern generators with learning for legged locomotion and malfunction compensation," *Information Sciences*, vol. 294, pp. 666–682, 2015.

[204] P. Kaluza and T. Cioacă, "Phase oscillator neural network as artificial central pattern generator for robots," *Neurocomputing*, vol. 97, pp. 115–124, 2012.

[205] A. J. Ijspeert, "Central pattern generators for locomotion control in animals and robots: a review," *Neural networks*, vol. 21, no. 4, pp. 642–653, 2008.

[206] J. H. Barron-Zambrano and C. Torres-Huitzil, “Cpg implementations for robot locomotion: Analysis and design,” in *Robotic Systems-Applications, Control and Programming*. InTech, 2012.

[207] T. Mori, Y. Nakamura, M.-A. Sato, and S. Ishii, “Reinforcement learning for cpg-driven biped robot,” in *AAAI*, vol. 4, 2004, pp. 623–630.

[208] A. Nogaret, E. L. O’callaghan, R. M. Lataro, H. C. Salgado, C. D. Meliza, E. Duncan, H. D. Abarbanel, and J. F. Paton, “Silicon central pattern generators for cardiac diseases,” *The Journal of physiology*, vol. 593, no. 4, pp. 763–774, 2015.

[209] P. Eckert, A. Spröwitz, H. Witte, and A. J. Ijspeert, “Comparing the effect of different spine and leg designs for a small bounding quadruped robot,” in *Robotics and Automation (ICRA), 2015 IEEE International Conference on*. IEEE, 2015, pp. 3128–3133.

[210] A. T. Sprowitz, A. Tuleu, A. J. Ijspeert *et al.*, “Kinematic primitives for walking and trotting gaits of a quadruped robot with compliant legs,” *Frontiers in computational neuroscience*, vol. 8, p. 27, 2014.

[211] L. Righetti and A. J. Ijspeert, “Pattern generators with sensory feedback for the control of quadruped locomotion,” in *Robotics and Automation, 2008. ICRA 2008. IEEE International Conference on*. IEEE, 2008, pp. 819–824.

[212] A. J. Ijspeert, A. Crespi, D. Ryczko, and J.-M. Cabelguen, “From swimming to walking with a salamander robot driven by a spinal cord model,” *science*, vol. 315, no. 5817, pp. 1416–1420, 2007.

[213] A. J. Ijspeert, “Biorobotics: Using robots to emulate and investigate agile locomotion,” *science*, vol. 346, no. 6206, pp. 196–203, 2014.

[214] N. S. Szczecinski, A. E. Brown, J. A. Bender, R. D. Quinn, and R. E. Ritzmann, “A neuromechanical simulation of insect walking and transition to turning of the

cockroach blaberus discoidalis," *Biological cybernetics*, vol. 108, no. 1, pp. 1–21, 2014.

[215] F. Dyson, *Imagined Worlds*. Harvard Univ. Press, 1998.

[216] H. Haken, "Analogy between higher instabilities in fluids and lasers," *Physics Letters A*, vol. 53, no. 1, pp. 77–78, 1975.

[217] ——, *Laser Light Dynamics*. North-Holland, Amsterdam, 1985.

[218] C. Weiss and H. King, "Oscillation period doubling chaos in a laser," *Optics Communications*, vol. 44, no. 1, pp. 59–61, 1982.

[219] C. Weiss, W. Klische, P. Ering, and M. Cooper, "Instabilities and chaos of a single mode nh3 ring laser," *Optics communications*, vol. 52, no. 6, pp. 405–408, 1985.

[220] C. Weiss and J. Brock, "Evidence for lorenz-type chaos in a laser," *PRL*, vol. 57, no. 22, p. 2804, 1986.

[221] L. M. Pecora and T. L. Carroll, "Synchronization in chaotic systems," *PRL*, vol. 64, no. 8, p. 821, 1990.

[222] Y. Liu, N. Kikuchi, and J. Ohtsubo, "Controlling dynamical behavior of a semiconductor laser with external optical feedback," *Phys. Review E*, vol. 51, no. 4, p. R2697, 1995.

[223] G. D. Vanwiggeren and R. Roy, "Communication with chaotic lasers," *Science*, vol. 279, no. 5354, pp. 1198–1200, 1998.

[224] A. Argyris, M. Hamacher, K. Chlouverakis, A. Bogris, and D. Syvridis, "Photonic integrated device for chaos applications in communications," *PRL*, vol. 100, no. 19, p. 194101, 2008.

[225] J. Ohtsubo, *Semiconductor lasers: stability, instability and chaos*. Springer, 2012, vol. 111.

[226] M. Naruse, S.-J. Kim, M. Aono, H. Hori, and M. Ohtsu, “Chaos and random-number generation based on nanoscale optical energy transfer,” in *European Quantum Electronics Conference*. Optical Society of America, 2015, p. EG_P_15.

[227] J. Moloney, J. Uppal, and R. Harrison, “Origin of chaotic relaxation oscillations in an optically pumped molecular laser,” *PRL*, vol. 59, no. 25, p. 2868, 1987.

[228] W. Forysiak, J. Moloney, and R. Harrison, “Bifurcations of an optically pumped three-level laser model,” *Physica D*, vol. 53, no. 1, pp. 162–186, 1991.

[229] R. Barrio, A. Shilnikov, and L. Shilnikov, “Kneadings, symbolic dynamics and painting lorenz chaos,” *Int. J. Bifurcation & Chaos*, vol. 22, no. 04, p. 1230016, 2012.

[230] T. Xing, J. Wojcik, R. Barrio, and A. Shilnikov, “Symbolic toolkit for chaos explorations,” in *Int. Conf. Theory and Application in Nonlinear Dynamics (ICAND 2012)*. Springer, 2014, pp. 129–140.

[231] T. Xing, R. Barrio, and A. Shilnikov, “Symbolic quest into homoclinic chaos,” *Int. J. Bifurcation & Chaos*, vol. 24, no. 08, p. 1440004, 2014.

[232] T. Xing, J. Wojcik, M. Zaks, and A. L. Shilnikov, “Fractal parameter space of lorenz-like attractors: A hierarchical approach,” in *Chaos, Information Processing and Paradoxical Games: The legacy of J.S. Nicolis*, G. Nicolis and V. Basios, Eds. Singapore: World Sci. Publ., 2015.

[233] K. Pusuluri, A. Pikovsky, and A. Shilnikov, “Unraveling the chaos-land and its organization in the rabinovich system,” in *Advances in Dynamics, Patterns, Cognition*. Springer, 2017, pp. 41–60.

[234] J. A. Gallas, “The structure of infinite periodic and chaotic hub cascades in phase diagrams of simple autonomous flows,” *Int. J. Bifurcation & Chaos*, vol. 20, no. 02, pp. 197–211, 2010.

[235] R. Barrio, F. Blesa, S. Serrano, and A. Shilnikov, "Global organization of spiral structures in biparameter space of dissipative systems with shilnikov saddle-foci," *Phys. Review E*, vol. 84, no. 3, p. 035201, 2011.

[236] A. Lempel and J. Ziv, "On the complexity of finite sequences," *IEEE Trans. Information Theory*, vol. 22, no. 1, pp. 75–81, 1976.

[237] V. S. Afraimovich, V. Bykov, and L. P. Shilnikov, "On the origin and structure of the lorenz attractor," in *Akademiia Nauk SSSR Doklady*, vol. 234, 1977, pp. 336–339.

[238] L. Shilnikov, A. Shilnikov, D. Turaev, and L. Chua, *Methods of Qualitative Theory in Nonlinear Dynamics*. Singapore: World Sci. Publ., 1998, 2001, vol. 1-2.

[239] A. Limaye, "Drishti: a volume exploration and presentation tool," in *Developments in X-Ray Tomography Viii*, ser. SPIE Proceedings, S. Stock, Ed., vol. 8506. International Society for Optics and Photonics, 2012, p. 85060X.

[240] A. L. Shil'nikov, L. P. Shil'nikov, and D. V. Turaev, "Normal forms and Lorenz attractors," *Int. J. Bifurcation & Chaos*, vol. 3, pp. 1123–1123, 1993.

[241] S. Wieczorek and B. Krauskopf, "Bifurcations of $n$-homoclinic orbits in optically injected lasers," *Nonlinearity*, vol. 18, no. 3, pp. 1095–1120, 2005.

[242] A. Algaba, F. Fernández-Sánchez, M. Merino, and A. Rodríguez-Luis, "Structure of saddle-node and cusp bifurcations of periodic orbits near a non-transversal T-point," *Nonlinear Dynamics*, vol. 63, no. 3, pp. 455–476, 2011.

[243] ——, "Analysis of the T-point-Hopf bifurcation in the Lorenz system," *Communications in Nonlinear Science and Numerical Simulation*, vol. 22, no. 1-3, pp. 676–691, 2015.

[244] L. P. Shilnikov, "A contribution to the problem of the structure of an extended neighborhood of a rough equilibrium state of saddle-focus type," *Math. USSR-Sb*, vol. 10, no. 1, pp. 91–102, 1970.

[245] L. P. Shilnikov and A. Shilnikov, “Shilnikov bifurcation,” *Scholarpedia*, vol. 2, no. 8, p. 1891, 2007, revision #153014.

[246] V. Bykov, “The bifurcations of separatrix contours and chaos,” *Physica D*, vol. 62, no. 1–4, pp. 290–299, 1993.

[247] P. Glendinning and C. Sparrow, “T-points: A codimension two heteroclinic bifurcation,” *Journal of Statistical Physics*, vol. 43, no. 3, pp. 479–488, 1986.

[248] P. beim Graben, S. Gerth, and S. Vasishth, “Towards dynamical system models of language-related brain potentials,” *Cognitive neurodynamics*, vol. 2, no. 3, pp. 229–255, 2008.

[249] J. E. Lewis and L. Glass, “Nonlinear dynamics and symbolic dynamics of neural networks,” *Neural Computation*, vol. 4, no. 5, pp. 621–642, 1992.

[250] P. beim Graben, J. D. Saddy, M. Schlesewsky, and J. Kurths, “Symbolic dynamics of event-related brain potentials,” *Physical Review E*, vol. 62, no. 4, p. 5518, 2000.

[251] R. Dale and M. J. Spivey, “From apples and oranges to symbolic dynamics: a framework for conciliating notions of cognitive representation,” *Journal of Experimental & Theoretical Artificial Intelligence*, vol. 17, no. 4, pp. 317–342, 2005.

[252] K. Dobosz and W. Duch, “Understanding neurodynamical systems via fuzzy symbolic dynamics,” *Neural Networks*, vol. 23, no. 4, pp. 487–496, 2010.

[253] S. I. Dimitriadis, “Complexity of brain activity and connectivity in functional neuroimaging,” *Journal of neuroscience research*, vol. 96, no. 11, pp. 1741–1757, 2018.

[254] P. Bonzon, “Towards neuro-inspired symbolic models of cognition: linking neural dynamics to behaviors through asynchronous communications,” *Cognitive neurodynamics*, vol. 11, no. 4, pp. 327–353, 2017.

[255] P. beim Graben and A. Hutt, “Detecting event-related recurrences by symbolic analysis: applications to human language processing,” *Phil. Trans. R. Soc. A*, vol. 373, no. 2034, p. 20140089, 2015.

[256] P. Cariani, “Symbols and dynamics in the brain,” *Biosystems*, vol. 60, no. 1-3, pp. 59–83, 2001.